UNIVERSITY OF OKLAHOMA

GRADUATE COLLEGE

Modeling and Evaluation of Protonic Ceramic Fuel Cells for Flare Mitigation

A THESIS

SUBMITTED TO THE GRADUATE FACULTY

in partial fulfilment of the requirements for the

Degree of

MASTER OF SCIENCE

By

JADEN NORMAN

Norman, Oklahoma

2024

Modeling and Evaluation of Protonic Ceramic Fuel Cells for Flare Mitigation

A THESIS APPROVED FOR THE

SCHOOL OF AEROSPACE AND MECHANICAL ENGINEERING

BY THE COMMITTEE CONSISTING OF:

Dr. Pejman Kazempoor, Chair

Dr. Hanping Ding

Dr. Hamidreza Shabgard

ACKNOWLEDGEMENTS

There is no question in my mind that this work would not have been possible on my own. I have been incredibly fortunate to have a wonderful support system throughout my academic career of family, friends, and excellent professors. First, I would like to give my sincere thanks to my advisor, Dr Pejman Kazempoor for his consistent guidance, encouragement, and support in both my classes and research under his tutelage. My initial interest in doing research for him came purely because of the friendly conversations we'd had during advising sessions as an undergraduate student. His friendly demeanor and vast knowledge were great boons to me when I was stuck on various aspects of developing the model throughout my final semester. I also want to thank the other members of my thesis committee, Dr Hanping Ding, and Dr Hamidreza Shabgard, for their patience and support.

I would also like to extend my gratitude to all my friends and colleagues at the University of Oklahoma. Particularly, I would like to thank Dr Abu Yousuf for his friendship, faith, and invaluable help in the many drafts and weeks of research that have gone into this work. He has always opened the door to me and has served as a great mentor during my graduate experience. I would also like to thank Chris Fisher and Hugh Nelson, who worked with me as I learned more about fuel cells and spent many hours with me in classes and research environments. I would also like to thank Ryan Young, for his constant friendship and support throughout all my time at the University of Oklahoma. He has always been able to find a way to lift spirits during the stressful stretches of exams and deadlines.

Most importantly, I would like to thank my wonderful family, and especially my loving wife, who has had great patience during the long nights and weeks of research. Without her love, understanding, and encouragement, all this work would not have been possible. I am also grateful to my parents, for preparing me for a successful college career and their unwavering love and support.

Table of Contents

LIST OF TABLES

LIST OF FIGURES

Abbreviations

Term	Name	Units (if applicable)
Acronyms		
Bcf/d	Billion Cubic Feet per Day	
BTX	Benzene, Toluene, Xylene	
CDC	Center for Disease Control and Prevention	
CTE	Coefficient of Thermal Expansion	
EES	Engineering Equation Solver	
FBR	Fixed Bed Reactor	
FDT	Fuel Delivery Tube	
GHG	Greenhouse Gas	
MDA	Methane Dehydroaromatization	
PEN	Positive, Electrolyte, Negatrode	
PCEC	Protonic Ceramic Electrolysis Cells	
PCER	Protonic Ceramic Electrochemical Reactor	
PCFC	Protonic Ceramic Fuel Cells	
SOFC	Solid Oxide Fuel Cell	
Equations		
A	Area	m^2
c_p	Heat capacity	$J \cdot K^{-1}$
D	Diffusion coefficient	$cm^2 \cdot s^{-1}$
d_h	hydraulic diameter	m^2
ΔG	Gibbs free energy	J
Δh	Specific enthalpy	$J \cdot mol^{-1}$
Δz	Length of discretized unit cell	m
ϵ	Emissivity of solid material	-
F	Faraday's constant	$C \cdot mol^{-1}$
h	Coefficient of convective heat transfer	$W \cdot m^{-2} \cdot K^{-1}$
h_{sidech}	Height of either the fuel or air-side channel	m
i_{cell}	Current running through the cell	A
j_{cell}	Current density	$A \cdot m^{-2}$
k	Thermal conductivity of solid	$W \cdot m^{-1} \cdot K^{-1}$
L	Length of the cell	m
λ	Thermal Conductivity of fluid	$W \cdot m^{-1} \cdot K^{-1}$
M	Molar mass	$g \cdot mol^{-1}$
μ	Viscosity	$Pa \cdot s$
N	Number of moles	mol
Nu	Nusselt Number	-
P	Pressure, or partial pressure with subscript	bar

P_m	Perimeter	m
Pr	Prandtl number	-
R	Gas constant	$J \cdot K^{-1}$
R_{ohm}	Resistance	Ω
r_i	Radius of layer i	m
r_j	reaction rate of reaction j	$mol \cdot K^{-1}$
Re	Reynold's number	-
ρ	Density	$kg \cdot m^{-3}$
σ	Stefan Boltzmann constant	$W \cdot m^{-2} \cdot K^{-4}$
T	Temperature	$°K$
τ	Thickness of anode or cathode layer	m
$\vec{V}$	Velocity	$m \cdot s^{-1}$
V	Voltage	V
Subscripts		
A	Air	
Act	Activation Overpotential	
An	Anode	
Airch	Air channel	
BT	Benzene to Toluene	
Ca	Cathode	
Conc	Concentration Overpotential	
EB	Ethylene to Benzene	
F	Reacting fuel	
FDT	Fuel Delivery Tube	
Fuelch	Fuel channel	
IC	Interconnect	
ICA	Interconnect. air side	
ICF	Interconnect, fuel side	
ME	Methane to Ethylene	
Ohm	Ohmic Overpotential	
ORR	Oxidation Reduction Reaction	
PEN	Positrode, Electrolyte, Negatrode	
PF	Pre-fuel	
PO	Partial Oxidation of Methane	
SR	Steam Reforming	
WGS	Water Gas Shift	

Abstract

Protonic Ceramic Fuel Cells (PCFCs) are an emerging mid-temperature fuel cell technology that specializes in electrochemically converting chemical energy into electrical energy. These PCFCs have been suggested as a future technology for flare mitigation through the cogeneration of power and useful chemicals. PCFCs are here proposed to accomplish this purpose by utilizing the wasted methane and C_2 components at these flaring sites to produce electricity, hydrogen, and aromatics. In this study, a numerical methane-fed protonic ceramic fuel cell model is developed utilizing recent advancements in PCFC fabrication, innovation, and experimentation. The model used a tubular PCFC geometry and implements mass and energy balances, as well as electrochemical, and kinetic equations solved using Engineering Equation Solver (EES) to predict the viability of the PCFC system. The system exhibits a very small power density on the order of ~0.01 W/cm^2, which is much lower than other fuel cells due to the chosen catalyst prioritizing the slower kinetics of methane dehydroaromatization. However, the results also indicate that the production of value-added aromatics allow the system to potentially be very economically friendly if the manufacturing costs can be brought down to 65% of their current costs. The realistic PCFC model is also compared and measured against competing technologies and is found to be competitive with current power production practices. The results of this study highlight the potential of PCFC technology to transform wasted energy into economic and environmental gains, offering a significant step forward in hydrogen-based sustainable energy practices.

Chapter 1: Introduction

1.1 Current Situation with Emissions

Climate change is becoming an apparent problem as the world continues to increase greenhouse gas (GHG) emissions. The exponential increase in GHG emissions in the world are directly responsible for global warming, increasing the average surface air temperature by about 1°C since 1900 [1]. The vast majority of that increase has occurred since 1990 and can be directly correlated with the expanded use of fossil fuels [1]. The release of GHG can continue to adversely affect global warming for over 100 years after its release; so, as the need for energy continues to grow across the globe, a need for cleaner energy production methods is necessary to mitigate the detrimental effects of GHG emissions.

In 2021, the U.S. was the second-highest emitting country, accounting for more than 10.85% of the world's total production-based greenhouse gas emissions [2]. Of this total, methane emissions are responsible for about 17% of the country's GHG emissions' anticipated warming effect over the next 100 years[3]. While CO_2 is the most common and longest lasting GHG, methane has a much shorter average post-release lifetime of only around 12 years [4]. However, in this short 12 year span, methane has a much larger overall warming effect than CO_2, despite the longer lifetime of CO_2 [4]. Therefore, reducing methane

emissions could provide a much more immediate impact on global warming due to its short lifetime.

In the U.S., the energy sector is responsible for 40% of the total methane emissions, with two of the leading causes being flaring and venting of natural gas. Flaring is the process of igniting natural gas so that it combusts into CO_2 and byproducts, whereas venting directly releases it into the atmosphere. Overall, the U.S. flares about 1.3% of the total natural gas it collects from deposits, and while this number sounds insignificant, it equates to nearly 1.5 billion cubic feet per day (Bcf/d) [5]. These processes are sometimes necessary in oil and gas production for safety reasons, but it is more common to see flaring and venting occur simply due to the price of processing outweighing the final product. This is an unfortunate occurrence that largely plagues oil and gas wellheads in remote locations, not connected to pipeline infrastructure. The added cost of processing the natural gas for transportation (often entailing a sweetening process and cooling to cryo-liquid temperatures) makes natural gas uneconomical for many remote oil and gas producers. This is most pronounced in the U.S. in North Dakota and Texas, two of the largest producing fossil fuels fuel states. Infrastructure capacity constraints account for 84 percent of flaring that occurs in North Dakota and 64 percent in Texas [6]. The impact of the infrastructure limitations' in just these two states on flaring is shown in Figure 1.1.

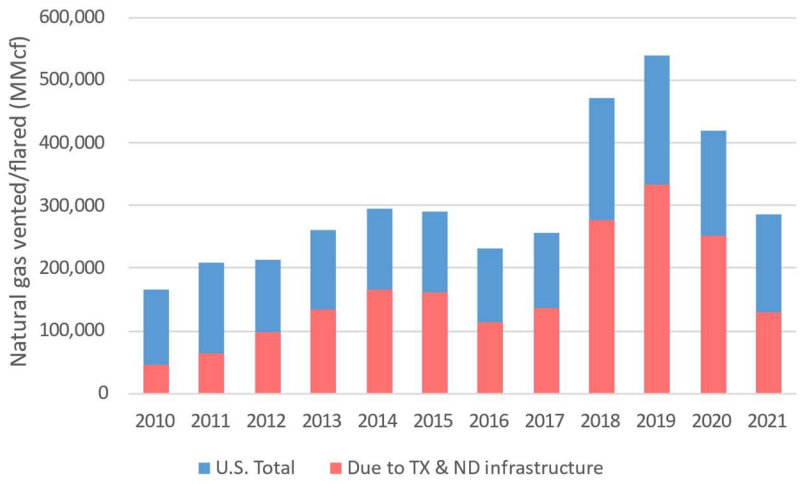

Figure 1.1: Current U.S. Flaring and Venting Rates gathered from U.S. Energy Information Administration [7]. Note: this data is gathered from the federally reported flaring and venting. Some states do not collect or report this data.

Figure 1.1 shows that the remote locations' limited access to pipeline infrastructure in Texas and North Dakota make up a huge portion of the total flaring in the country. It is also worth noting that the substantial decrease in flaring in 2020 and 2021 can be partially attributed to the COVID-19 pandemic that resulted in the price of oil barrels reaching less than $0 [8]. Regardless, 70% of natural gas sent to flares are sent to flares that run on a near-constant basis [9], and these remote locations make up a significant portion of that number.

1.2 Role of Electrochemical Cells

In light of the issues discussed above, many investors and government programs are looking into developing technologies that can mitigate flaring in all scenarios [10]. One such promising technology is protonic ceramic fuel cells (PCFC). Fuel cells are designed to harness chemical energy and directly transform it into electrical energy. Fuel cells have been earmarked as having incredible potential in the energy sector since this process is not limited by the Carnot cycle like other energy systems.

Fuel cells are particularly desirable because they can store and create clean, green energy, so long as the materials provided are also collected through renewable methods. They have become more and more viable especially due to the drastic improvements made since 2005 [11]. Despite improvements, fuel and electrolysis cells are not currently used in the natural gas market, but they have the potential to make a remarkable difference in a variety of areas, especially relating to chemical production and power plants due to their ability to run on methane and natural gas [12], [13].

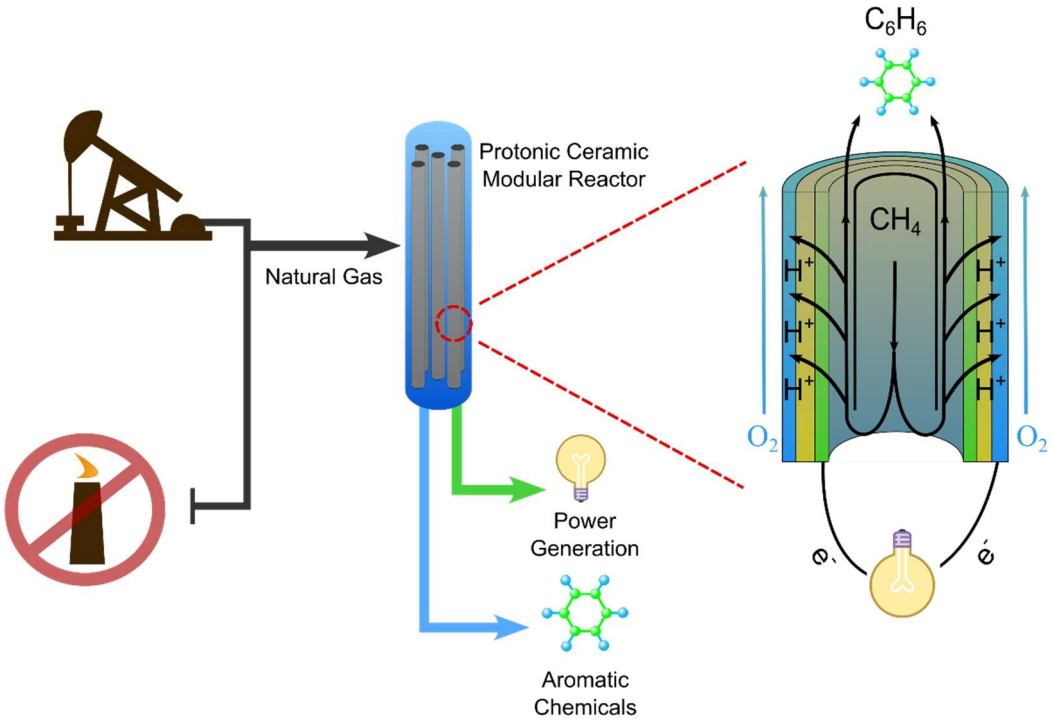

Figure 1.2: Implementation of PCER for flaring mitigation

Figure 1.2 above shows one such potential application wherein a protonic ceramic electrochemical cell reactor (PCER) is theorized to be particularly useful as a natural gas reactor the cogenerates power and aromatic chemicals from natural gas. This theory was originally published by Liu et al but is yet to be theoretically or practically confirmed [13]. If

such reactors could be placed in the natural gas process just prior to the flare, there could be great environmental improvements and a drastic increase in the overall output and utility of the natural gas, especially as PCFCs continue to improve[11].

The idea of utilizing methane in fuel cells for the cogeneration of power and value-added chemicals has been a topic of several studies [14], [15], [16], but it is far more common for studies to focus on either power *or* chemical production. A common practice, which is utilized throughout this work, is for these processes to be distinguished by referring to the system as a PCFC when the intention is power production and a protonic ceramic electrochemical (or electrolysis) cell (PCEC) for chemical production. For example, Hong, et al. published a PCFC study in 2023 boasting an incredible methane conversion rate of up to >85% at 700 °C from a methane and carbon dioxide mixture to produce syngas [17]. However, his study does not discuss power generation results from the cell, so this would designate it as a PCEC system for the purpose of discussions in this work. To consider the idea of cogeneration, PCFC and PCEC studies are considered together under the umbrella of PCERs throughout this work.

1.3 Project Description

1.3.1 Rationale

In light of the possibility suggested by Figure 1.2, the aim of this work is to ascertain the theoretical and economic viability of implementing a protonic ceramic modular reactor to cogenerate power and aromatics to utilize currently stranded/flared natural gas. PCERs optimized for the cogeneration of power and aromatic chemicals from methane/natural gas

are yet to be assembled. As such, there is no specific experimental data from which to build a theoretical model to estimate the benefits of such a device. Therefore, this work utilizes the knowledge of existing PCFCs and aromatic chemical production catalysts to estimate optimal parameters and capabilities of the system. The goal for the optimized model is to achieve the following outcomes [18]:

1. Achieves >30% natural gas conversion
2. Achieves an aromatics yield of >50%
3. Overall >90% reduction in CO2 emissions

1.3.2 Project Objectives

- Develop a model for the PCER theorized by the DOE goals
- Optimize input parameters for the PCER system
- Identify realistic power and chemical outputs from such a system
- Perform a rough economic analysis to establish minimum performance capabilities

1.4 Thesis Structure

The thesis is organized into 6 chapters. The subsequent chapters and sections are outlined as follows:

Chapter 2 discusses the technological background necessary for this project. This is done by first discussing the operation of fuel cells and how they fit into a power system in section 2.1. This is followed by a large discussion on the methane dehydroaromatization (MDA) reaction in section 2.2, since understanding the reaction is critical in effectively

modeling the PCER's capabilities. Finally, these discussions are merged to introduce the suggested MDA reaction mechanism in the PCER in section 2.3.

Chapter 3 details the model formulation and the exact constants used for the reaction and electrochemical cell sub-models. Appropriate justification is provided as to why some methods and approaches are chosen over others.

Chapter 4 highlights the results from the PCER model. This is done by first validating the model in section 4.1, and then identifying important parametric relationships and guidelines for the PCER operation in subsequent sections.

Chapter 5 includes an economic discussion and considers the results from chapter 4 to determine whether the suggested PCER system is economically viable. An Aspen-HYSYS model is used to reliably estimate the cost and returns of the PCFC system.

Chapter 6 provides a summary of conclusions and recommendations for further research efforts.

Chapter 2: Technological Background

2.1 Fuel Cells

2.1.1 Fuel Cell Concepts

While there are many types of fuel cells, PCFCs represent one of the most promising avenues of energy storage systems for future industrial applications. One of the biggest draws to PCFCs over other fuel cell types like solid oxide fuel cells (SOFC) is due to their ability to operate effectively in intermediate temperature ranges of $\sim 400 - 750$ °C [19], whereas SOFCs require temperatures of 600-1000 °C.

The setup and process within a PCFC is relatively straightforward. Fuel cells can operate as a galvanic reactor consisting of an anode and cathode, usually separated by a conductive electrolyte. This stack of three mediums is often referred to in literature as the positrode, electrolyte, negatrode (PEN) assembly. In a PCFC, hydrogen-rich fuel is supplied to the anode, which is ionized and passed through a proton-conducting electrolyte to react with oxygen that is supplied on the cathode side to output water. As the hydrogen is dissociated into protons, the emitted electrons are passed through a circuit, generating power as shown in Figure 2.3.

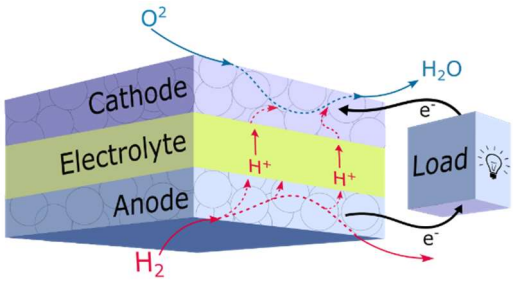

Figure 2.3: Standard hydrogen-fed PCFC mechanism

The cell reactions can be represented as follows:

$$H_2 \rightarrow 2H^+ + 2e^- \text{ anode reaction} \quad (2.1)$$

$$0.5O_2 + 2H^+ + 2e^- \rightarrow H_2O \text{ cathode reaction} \quad (2.2)$$

Equations 2.1 and 2.2 combine to create the water formation reaction. This reaction is very exothermic and can help reach and/or maintain the high operating temperatures in the cell.

2.1.2 Fuel Flexibility

PCFCs always achieve their highest efficiencies when hydrogen is the fuel, but hydrogen is a very expensive feedstock and is one of the biggest challenges in justifying industrial application. Alternatively, PCFCs have proven capable of running on natural gas, methane, ethanol, propane, butane, ammonia and other hydrogen-rich hydrocarbons [12]. This is possible due to the high temperature of the cell, which helps to provide the activation energy needed for the decomposition of hydrocarbons into carbon and hydrogen. For methane and natural gas, which is the focus of this study, the power output of the cell has shown a drop to roughly 60% of its hydrogen-fed counterpart [12].

2.1.3 Challenges and developments in PCFCs

There are a variety of challenges faced by PCFCs. Some notable challenges include, but are not limited to the following points:

- Stability and resistance to coking [13]
- Applying economic and effective seals across the channels and materials during manufacturing [20]
- Mismatches in coefficients of thermal expansion (CTE) resulting in high internal stress [19]

The lower temperature of PCFCs can help alleviate some of the coking and internal stress, but these issues require advancements in the materials science of the catalyst, electrolytes and electrodes to truly be mitigated. Issues with seals are much more significant in planar cells than they are in tubular configurations.

Many incredible advancements have been made with regard to improving the materials used in the PEN assembly. Some studies focus on manufacturing [21], while others focus on catalyst development, such as designing for improved selectivity of products [22]. Kasyanova et al. wrote a remarkable review discussing the advancements of recent PCFC studies [19]. Some of their referenced studies, along with other works directly applicable to this study are shown below in Table 1.1:

Table 1.1: Notable recent works in PCFC experimental studies

Electrolyte (E) and Cathode (C) Compositions	Power Density	Features	Year	Ref
E: $BaCe_{0.55}Zr_{0.3}Y_{0.15}O_{3-\delta}$ (< 5 μm) C: $Ba_{0.5}BaCe_{0.55}Zr_{0.3}Y_{0.15}O_{3-\delta}Sr_{0.5}Co_{0.8}Fe_{0.2}O_{3-\delta}$	500 °C: 535 mW/cm^2 600 °C: 1302 mW/cm^2	High performance, low stability/durability in a 5x5 cm^2 working area	2018	[23]
E: $BaCe_{0.7}Zr_{0.1}Y_{0.2}O_{3-\delta}$ (10 μm) C: $La_{0.5}Sr_{0.5}Fe_{0.9}Mo_{0.1}O_{3-\delta}$	650 °C: 851 mW/cm^2 700 °C: 1174 mW/cm^2	Modification of $La_{0.5}Sr_{0.5}FeO_{3-\delta}$ with molybdenum	2021	[24]

E: $BaCe_{0.7}Zr_{0.1}Y_{0.1}Yb_{0.1}O_{3-\delta}$ (25 um) C: $Ba(Co_{0.4}Fe_{0.4}Zr_{0.1}Y_{0.1})_{0.95}Ni_{0.05}O_{3-\delta}$	500 °C: 270 mW/cm^2 550 °C: 450 mW/cm^2 600 °C: 660 mW/cm^2	Triple-conducting electrode with improved electrochemical activity and reduced CTE	2021	[25]
E: $BaCe_{0.7}Zr_{0.1}Y_{0.1}Yb_{0.1}O_{3-\delta}$ (14 um) C: $La_{0.6}Sr_{0.4}Co_{0.2}Fe_{0.8}O_{3-\delta} - BaCe_{0.7}Zr_{0.1}Y_{0.1}Yb_{0.1}O_{3-\delta}$	500 °C: 240 mW/cm^2 550 °C: 380 mW/cm^2 600 °C: 570 mw/cm^2	Introduction of porous interlayer between E and C	2021	[26]
E: $BaCe_{0.7}Zr_{0.1}Y_{0.1}Yb_{0.1}O_{3-\delta}$ (25um) C: $La_{0.6}Sr_{0.4}Co_{0.2}Fe_{0.8}O_{3-\delta} - BaCe_{0.7}Zr_{0.1}Y_{0.1}Yb_{0.1}O_{3-\delta}$	500 °C: 188 mW/cm^2 550 °C: 294 mW/cm^2 600 °C: 465 mW/cm^2	Tubular PCFC with working area of 2.3 cm^2	2021	[27]
E: $BaZr_{0.1}Ce_{0.7}Y_{0.1}Yb_{0.1}$ (7 um) C: $PrBa_{0.5}Sr_{0.5}Co_{1.5}Fe_{0.5}O_{5+\delta}$	NH_3: 700 °C: 1060 mW/cm^2 H_2: 700 °C: 1330 mW/cm^2	Tubular PCFC, fueled by NH_3 and H_2, prepared by phase inversion	2022	[28]
E: $BaCe_{0.7}Zr_{0.1}Y_{0.2}O_{3-\delta}$ C: $LaNi_{0.6}Fe_{0.4}O_{3-\delta} - Sm_{0.5}Sr_{0.5}CoO_{3-\delta}$	600 °C: 425 mW/cm^2 650 °C: 728 mW/cm^2 700 °C: 1427 mW/cm^2	New combination of perovskite and materials for cathode	2022	[29]
E: $BaSn_{0.16}Zr_{0.24}Ce_{0.35}Y_{0.1}Yb_{0.1}Dy_{0.05}O_{3-\delta}$	600 °C: 318 mW/cm^2	Promising new proton conductor	2022	[30]
E: $BaCe_{0.7}Zr_{0.1}Y_{0.1}Yb_{0.1}O_{3-\delta}$ (BCZYYb) C: $Ba_{0.95}La_{0.05}Fe_{0.8}Zn_{0.2}O_{3-\delta} - BCZYYb$	550 °C: 174 mW/cm^2 600 °C: 342 mW/cm^2 650 °C: 601 mW/cm^2 700 °C: 847 mW/cm^2	Introduction of a nano-structured active layer to expand triple phase boundary	2023	[31]
E: $BaZr_{0.2}Ce_{0.7}Y_{0.1}O_{3-\delta}$ C: $Sr_4Fe_4Co_2O_{13+\delta} + BaZr_{0.2}Ce_{0.7}Y_{0.1}O_{3-\delta}$	550 °C: 550 mW/cm^2	Excellent triple-conducting cathode material SFC+BCZY	2023	[32]
E: BaCe0.2Zr0.7Y0.1O3−δ(BCZY27) (12um) C: BaCo0.4Fe0.4Zr0.1Y0.1O3−δ (11um)	650 °C: 196 mW/cm^2	Introduces new 3D printing method for mass-producible tubular PCFCs	2023	[21]
E: $BaCe_{0.4}Zr_{0.4}Y_{0.1}Yb_{0.1}O_{3-\delta}$ C: $BSC + PBSCF$	H_2: 600 °C: 1640 mW/cm^2 H_2: 450 °C: 770 mW/cm^2 CH_4: 500 °C: 550 mw/cm^2	Incredible peak power densities at lower operating temperatures	2023	[33]

2.2 Methane Dehydroaromatization

2.2.1 Benzene Production Pathways

Benzene plays an important role in the global economy as it is one of the foundational components of many commonly used industrial products like plastics, synthetic fibers, resins and nylon. In addition, benzene plays a role in the production of many lubricants, detergents, drugs, dyes, rubbers, and pesticides [34]. With a strong worldwide need for benzene, it has become one of the top 20 chemicals for production volume in the world [34], [35].

Currently, around 70% of the world's benzene production comes from naphtha via catalytic reforming and steam cracking [36]. These are multi-step processes that require a

variety of intermediates and output a mixture of components that include aromatics like benzene, as well as alkanes, cycloalkanes, hydrogen, and light gases [37]. This leads to a relatively complex separation process to isolate these different chemicals.

MDA offers a high upside alternative to these expensive processes. The MDA process is a direct conversion from methane to benzene, aromatics, and hydrogen. This process is a more direct route, with fewer intermediates and overall has a much less complex process than the more mature naphtha reforming [38]. Therefore, it has the potential to reduce costs and increase profitability for chemical manufacturers of benzene.

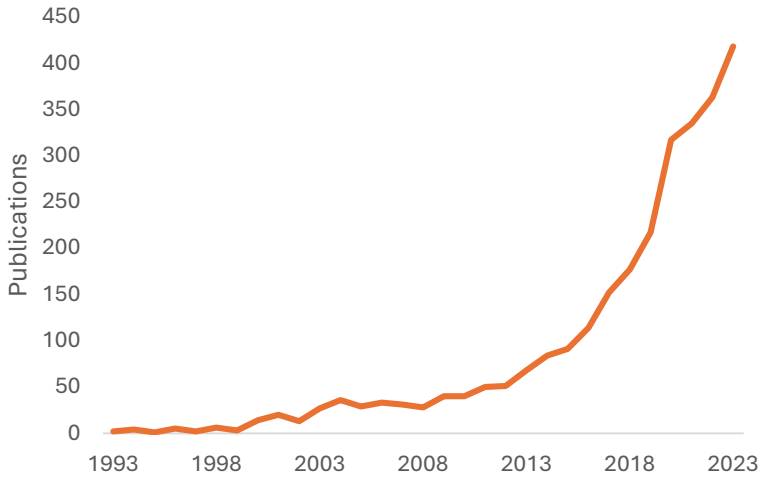

Figure 2.4: Published research articles related to MDA.

The potential of MDA is reflected in the research studies around it. Figure 2.4 shows the rapidly growing interest in MDA research from the scientific community. The growing interest is proof of the potential economic and societal impact of the process in a variety of affected industries. This section covers the following objectives: I) establish a global need for benzene; II) discuss the theoretical reaction mechanisms for MDA; III) Analyze the

existing popular means of MDA (fixed and fluidized bed reactors); IV) determine the potential for using electrochemical means (PCFC) of achieving MDA.

2.2.2 Essentiality of Benzene Production

Benzene, toluene, and xylene (BTX) are often referred to as “value added chemicals” due to their usefulness as feedstocks for other products [39]. The namesake “value added” is especially true in comparison to methane, since benzene is far easier to transport and also functions as a fundamental building block in the chemical industry.

The global market size of benzene is expected to grow by about 4.6% annually through at least 2028 due to its prominent role in several massive industries [40]. For example, the materials derived from benzene play crucial roles in automotive fabrication and batteries for the growing electric vehicle market. In addition, many insulation materials and adhesives require benzene, making it required for the construction industry. Lastly, benzene’s unique properties are also helpful for making many kinds of pharmaceutical compounds and medicines, establishing it as a building block of the pharmaceutical industry [40].

The economic impact of MDA would benefit all these global industries, but arguably the most important benefit could lie in the fact that MDA can be a reliable consumer of methane. As crude oil continues to be depleted as well as increase in cost, there is a growing need to open a new source for benzene without oil/naphtha as the raw material [41]. Methane fits this need very well. In addition, methane can be produced through biological processes using renewable sources such as biomass or organic waste in a process called biomethanation or anaerobic digestion. In this case, methane is considered renewable

because the feedstock (biomass or organic waste) can be continuously replenished through natural processes such as plant growth or waste generation.

However, even with the potential benefits, benzene and aromatic production come with a few notable societal drawbacks. For example, where once benzene was used as an important additive in gasoline production due to its high octane number, this practice has since become much more moderated due to its carcinogenic nature. Benzene is potentially harmful enough that the Center for Disease Control and Prevention (CDC) goes as far as recommending that people should not live near gasoline fueling stations and not even let their children play around them [35]. In light of this drawback, it is important that great care is taken to mitigate direct human exposure to benzene.

The MDA process is not yet widely practiced in industrial settings due to its immaturity compared to existing benzene production methods. In other words, there are certain aspects of the process that must be improved before the full potential of MDA can be implemented and realized. To do that, a thorough understanding of the chemistry and thermodynamics of the reaction is required.

2.2.3 Chemistry of MDA

MDA is defined by the transformation of methane into benzene and hydrogen as shown below:

$$CH_4 \rightarrow C_6H_6 + 9H_2 \qquad \text{(Non-oxidative)} \qquad (2.3)$$

$$6CH_4 + 4.5O_2 \rightarrow C_6H_6 + 9H_2O \qquad \text{(Oxidative)} \qquad (2.4)$$

This is a strongly endothermic reaction and therefore typically requires high temperatures to see significant results. It is generally accepted that MDA occurs under two different conditions: oxidative and non-oxidative. While still endothermic, MDA is more thermodynamically favorable in oxidative conditions. Although, Han et al. discovered in 1992 that the benzene selectivity over zeolite catalysts was only ~3% in oxidative conditions due to an overabundance of CO and CO_2, which tracks with the oxidative production of syngas [42]. In 1993, Wang et al. experimented with non-oxidative MDA and reported that while it still may not be very thermodynamically favorable (meaning low conversion rates), there are very low levels of byproducts [43]. This was the beginning of a great spark of research looking to improve non-oxidative MDA.

Over the last 30 years, the most commonly practiced reaction conditions include a temperature generally around 700 °C (973°K) and a pressure of 1 bar [38], [43], [44]. While 1 bar has been the most studied condition, it is worth noting that even at the early stages of MDA research, it was identified that an increased overall and partial pressure of methane correlated with an increased yield of benzene over otherwise identical reaction conditions [43], [45]. The maximum conversion and selectivity of benzene and aromatics has improved with catalyst development, with the current conversion rates around 12-18% and selectivity reaching up to 90% in fixed and fluid bed reactors [41], [44], [46], [47], [48].

2.2.4 Reaction Mechanisms

Various researchers have had differing opinions on the exact reaction steps, mechanisms and kinetics of MDA, but there have been several consistent findings

throughout the available data. A few of these can be consolidated into the following points [38], [41], [42], [43], [44], [46], [47], [48], [49], [50]:

1) Mo/ZSM-5 (or Mo/HZSM5) works as a bi-functional catalyst, i.e. there are two active reaction sites.
2) At the beginning of the reaction, there is an induction period wherein MoO_x species are reduced to Mo_2C or MoO_xC_y by methane.
3) Coke formation occurs quickly on the catalyst leading to catalyst deactivation, especially at higher temperatures.

Attempts to define a reaction rate and kinetics for MDA are merely theoretical up to this point, with various researchers coming to differing conclusions. This is primarily because the identity, standard Gibbs energy, and surface coverages of the intermediate species are not able to be determined experimentally since the reaction steps are not distinguishable in steady state [51]. Instead, pulsed reaction techniques are combined with quasi-in-situ spectroscopic characterization to definitively outline 3 primary reaction stages [52], [53], [54].

i) Activation: This stage involves the autocatalytic reduction of Mo(VI) with carbon monoxide (CO) as the primary carbon-containing product.
ii) Induction: This stage is characterized by the formation of surface carbon species.
iii) Autocatalytic Formation of Benzene: This final stage is where the formation of benzene occurs.

Once again, the details of how these various stages happen are still unconfirmed, with varying theories being applied and models attempted. However, all the significant theories involve some mixture or isolation of acetylene, ethane, and ethylene as

intermediates in the reaction. These theories can be divided into two primary categories as shown in Figure 2.5 below [44].

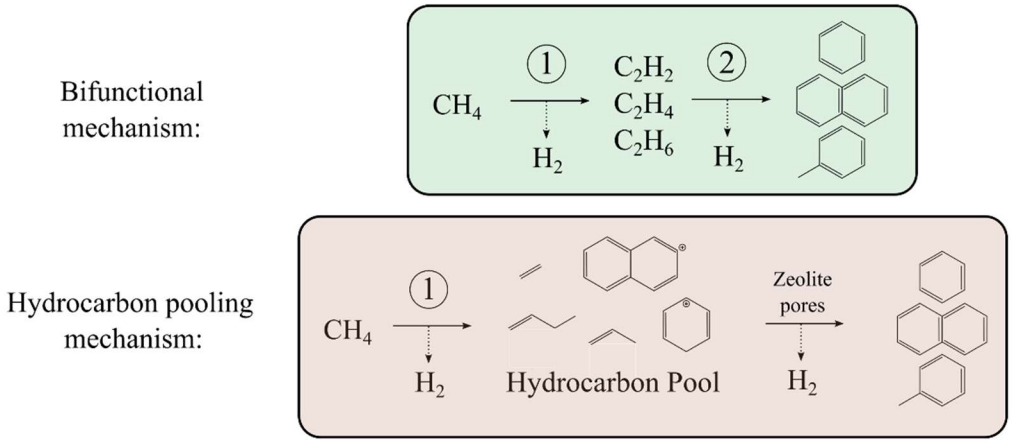

Figure 2.5: Proposed MDA reaction pathways

The Bifunctional mechanism is the most thoroughly covered topic and represents the leading theories for MDA reaction mechanisms. The hydrocarbon pool mechanism has been proposed only recently and the intermediates are largely unknown [44], [52]. Kosinov et al. states that both these fundamental mechanisms could potentially even be co-existing in the MDA reaction [55]. While neither theory can be wholly ruled out, an overwhelming amount of literature agrees that there is likely to be some form of C_2 molecules as intermediates as shown in the bi-functional mechanism [38], [41], [42], [44], [45], [47], [49], [50], [51], [52], [53], [56], [57], [58], [59], [60], [61], [62]. Since the majority of the research, available data and theoretical models to date discuss and utilize the bifunctional mechanism, that is the mechanism used for this study.

2.2.5 Bifunctional Mechanism

For the bifunctional mechanism, Razdan et al. [51] suggested the following scheme since he hypothesized that, of the C_2 intermediates, acetylene is easily the most readily aromatized into benzene.

$$6CH_4 \xrightarrow[+3H_2]{} 3C_2H_6 \xrightarrow[+3H_2]{} 3C_2H_4 \xrightarrow[+3H_2]{} 3C_2H_2 \rightarrow C_6H_6$$

In Razdan's scheme, ethylene dehydrogenation to acetylene is proposed to take place at Mo sites, while acetylene aromatization may be catalyzed by either Mo or Bronsted acid sites [51]. This somewhat all-inclusive setup is relatively complex compared to other successful models. For example, Fila et al. performed their work in 2015 under the assumption that ethylene is the only primary intermediate since it can be a byproduct of the reaction [45]. This assumption that ethylene is the primary (or only) intermediate is the most common practice seen over the last 30 years, but recent studies and models have combated this idea. In 2020, Razdan et al. performed a kinetic study and arrived at the conclusion that ethane is the initial product of C-C coupling, while acetylene is the aromatizing intermediate [51]. Likewise, in 2019, Vollmer et al. performed another study that showed very different reactivities of ethylene and methane over Mo-ZSM-5 and arrived at the conclusion that "ethylene might not be the actual intermediate" [44], [60]. The combination of Razdan's and Vollmer's studies indicate the wide variety of opinions and discussion on the reaction mechanism. Despite this variety, it is important to note that most of the literature supports the idea of ethylene as an intermediate, and this idea is commonly represented in modeling efforts. Only more recent studies indicate that ethylene is likely joined by several other intermediates [51], [60].

It is also interesting to note the effect of various additives on the reaction. For example, Skutil et al. found that adding small amounts of CO and CO_2 to the methane resulted in enhanced catalyst stability and promoted benzene production [54]. However, large amounts of carbon oxides would completely suppress the catalyst activity very quickly. Similarly, adding large amounts of water (9.5%) had the same effect of complete catalyst deactivation. Additionally, aiding the case for C_2's as intermediates, adding minor amounts of ethylene and ethane to the inlet methane stream significantly increased benzene yield [54].

2.2.6 Modeling the MDA Reaction

Many attempts have been made to simulate the MDA process in an effort to envision it in an industrial setting. One of the earliest attempts was made in 2001 when Lin Li et al. generated a model with CHEMKIN using a detailed reaction-transport model with a plug flow tubular reactor [59]. This model was successful at 950 °K and a CH_4 partial pressure of 0.5 bar, utilizing ethylene as the only intermediate. The model also assumed production of both benzene and naphthalene. In 2018, Zhu et al. also suggested a model with the same products and ethylene as the intermediate. Zhu et al.'s model made use of a Langmuir-Hinshelwood model governed by 3 global reactions: methane to ethylene, ethylene to benzene, and benzene to naphthalene [61].

Zhu et al.'s model successfully simulated existing data from an isothermal packed bed reactor and is one of the most conclusive and definitive modeling attempts to date. The findings from this model have important implications for both research and industrial application. For research and development purposes, this model insinuates that the MDA

reaction can be accurately modeled to predict aromatic yield with ethylene as the intermediate, regardless of whether other intermediates or hydrocarbon pooling take place. The model also confirms the fact that methane recycling is required in commercial scale up for MDA. This is due to the methane conversion rate being equilibrium-limited to only 12% in the model. As a result of this limitation, a variety of researchers have suggested the implementation of extracting the hydrogen through a membranous wall or through pressure swing adsorption to increase the methane conversion [57], [58], [61]. While this strategy undoubtedly increases methane conversion, it has also shown the potential to shift some of the benzene selectivity to other aromatic products [61].

In another attempt to simplify the kinetic model, Zuoan Li et al. proposed a Langmuir-Hinshelwood model in 2012 that ignored intermediates altogether as seen below [63].

$$r = \frac{k_1 f_{CH_4}^6 \left(1 - \frac{f_{C_6H_6} f_{h_2}^9}{K_R f_{CH_4}^6}\right)}{\left(1 + K_{CH_4} f_{CH_4} + K_{H_2} f_{H_2} + K_{C_6H_6} f_{C_6H_6}\right)^6}$$

While ignoring intermediates is ineffective for chemical reaction analysis, the goal for this model was merely to establish effective fluid dynamics parameters for the reaction and reactor. It was determined that methane conversion rates could be increased by decreasing pressure and space velocity and increasing temperature [63], although it has also been experimentally proven that increasing the temperature too much can also drive up coke formation and even deplete aromatic selectivity [50]. However, it is also worth noting that while Li's report agrees with previous work [38] in stating that decreasing pressure also increases methane conversion percentage per pass, other studies have clearly shown that increased pressure yields an increase in total aromatic production and methane conversion

[44], [52], [53]. Therefore, a balance can be found in conversion rate and selectivity through pressure and temperature.

The last important MDA modeling effort considered here comes from the work of Jeong et al. [64]. Jeong's work is chosen as the foundational kinetic model for this study due to the efforts taken to establish detailed kinetic parameters for the MDA reaction over Mo/HZSM-5 catalyst. This task was completed using a six step reaction mechanism that included methane, ethylene as the intermediate, and benzene, naphthalene, toluene, and ethane as products shown in Figure 2.6 below [64]:

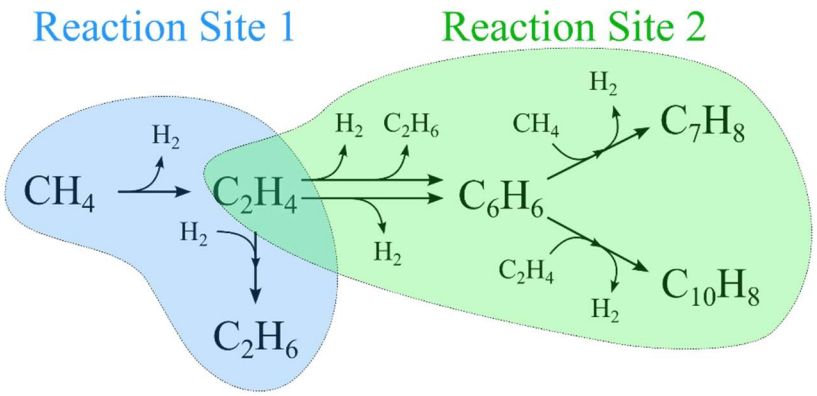

Figure 2.6: Kinetic model setup from Jeong et al. [64]

Utilizing Langmuir-Hinshelwood expressions, Jeong et al. was successfully able to mimic the results of a fixed-bed quartz reactor at atmospheric pressure and 700 °C. This particular experimental setup is very close to what was used by Zhu et al. [65], whose work is used for the validation of the model in Chapter 3. The results from the studies indicate that the ideal temperature for MDA is approximately 700 °C, as benzene yield and methane conversion both dropped at more elevated temperatures (750+°C) due to coking [64]. Additionally, toluene and ethylene represented a very small amount of the total product

(<0.1% yield) after 2 hours on the catalyst. Naphthalene was a little more prominent but benzene was the clear primary product from the MDA reaction [64].

2.2.7 Catalyst Breakdown

Mo/ZSM-5 has been a focal point of study in the MDA reaction for decades, known for achieving benzene yields close to thermodynamic limits (5-15% at 600-800 °C) with a high benzene selectivity (70-90%) across various space velocities and methane partial pressures [44]. The bifunctional nature of the catalyst functions such that Mo and Brønsted acid sites can alternate to complete the reaction process. As such, the degree of Mo-loading strongly influences the catalyst activity, with too much and too little Mo-loading having adverse effects on MDA. The majority of modern studies have estimated the ideal loading at somewhere between 4.5%-6% Mo wt% without catalyst promoters [44], [50], [54], [66], [67], [68]. However, this loading percentage can change when other metals or promoters are implemented with Mo [65]

One of the most important aspects of catalyst preparation for MDA is the mitigation of coke formation. After a thorough analysis, Zhang et al. conclude that there are three types of inhibiting coke formation throughout the Mo/ZSM-5 catalyst [66], [69]:

1) Coke formation on Mo sites inside the zeolite channels, deactivating CH_4 activation
2) Coke formation on Brønsted acid sites inside channels, narrowing the cross section and inhibiting the aromatics from diffusing
3) External coke formation at the channel mouth blocking reactants from entering and products from leaving

Understanding these three types of coke formation leads to improved coke management such as regeneration, coke burn off, or other strategies. Optimizing reaction parameters, recycling, and regeneration are common ways to mitigate these formations, but these are limited in how much they can economically benefit the process without further developments in the catalyst effectiveness for MDA.

2.2.8 Industrial Challenges

For industrial MDA application, there are three significant challenges to overcome due to the nature of MDA being an equilibrium-limited, endothermic reaction as discussed above. These issues are first, effectively supplying the sufficient heat of reaction; second, achieving an effectively high methane conversion and benzene selectivity such that the system can be competitive with existing benzene and aromatic production technologies; and third, reducing regeneration time required due to coke formation.

2.3 Electro-catalysts for MDA

Industrial methane reforming and processing usually takes place in large reactors for processes like steam reforming, water gas shift reactions, and other processes. Packed and fluidized beds are often used to produce and isolate certain products like ethylene and syngas [13], [70], [71]. A promising alternative for methane reforming yet to be industrialized is the use of electrochemical cells. Specifically, PCERs have great potential to be both more economically and more environmentally friendly than current industrial practices.

2.3.1 Electrocatalyst Reaction Mechanism

PCEC systems are designed to conduct ions like protons (and sometimes O^{2-}) and should not necessarily play a role in the MDA reaction mechanism itself. The advantage instead lies with a hybrid process that continually removes hydrogen that helps alleviate the equilibrium limitation faced by standard fixed and fluidized-bed reactors. Hydrogen removal, or conduction in PCECs, can greatly increase aromatic selectivity as discussed earlier [57], [58], [61], [66].

Additionally, the electrolyte membrane in PCECs exhibit minor oxygen-ion conductivity since PCEC electrolytes are not truly pure hydrogen conductors [72]. Liu et al. and Morejudo et al. both note that this attribute enables the concurrent limited-injection of oxygen to the methane aromatization electrode, which helps burn off coke by selectively reacting with hydrogen and hydrocarbons to produce water and carbon dioxide, which mitigates deactivation due to coking, as shown in Figure 2.7 [13], [73].

Studies and tests to this point for MDA application in PCECs have generally required a standard MDA catalyst like Mo/ZSM-5 to be partially coated or otherwise integrated into the methane-fuel side of the PEN assembly. In this way, the methane can undergo the catalyst-enhanced dehydroaromatization, and then the resulting hydrogen is conducted away by the electrochemical process. This combination also helps the thermodynamics of MDA since the hydrogen must dissociate prior to conducting across the electrolyte, which is an exothermic process that helps provide heat for the endothermic MDA.

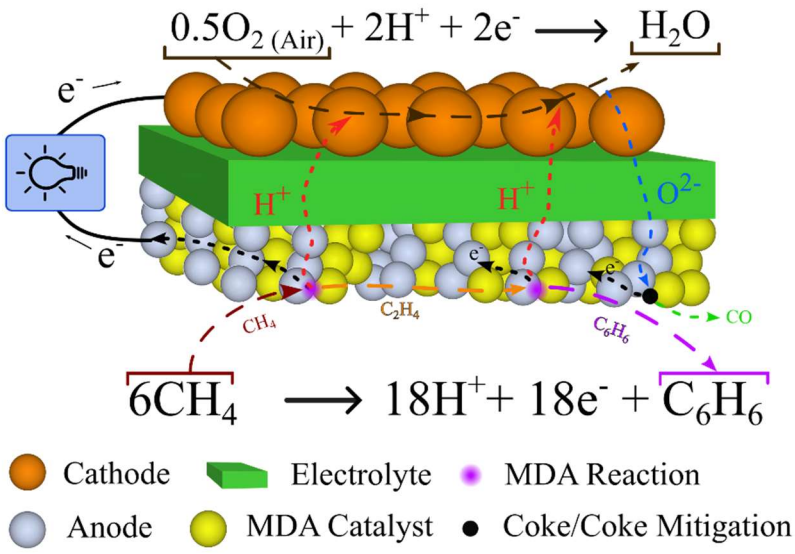

Figure 2.7: MDA reaction mechanism in a protonic ceramic electrochemical cell, using a co-ionic membrane.

2.3.2 PCERs with MDA

Not many experiments have been performed yet to fully understand how much benefit there is to be gained from utilizing PCEC for MDA. However, Morejudo et al. performed one of the first trial studies, implementing MDA catalysts such as Mo/ZSM-5 and Mo/MCM-22 into a cell membrane reactor that acts just like a PCEC [73].

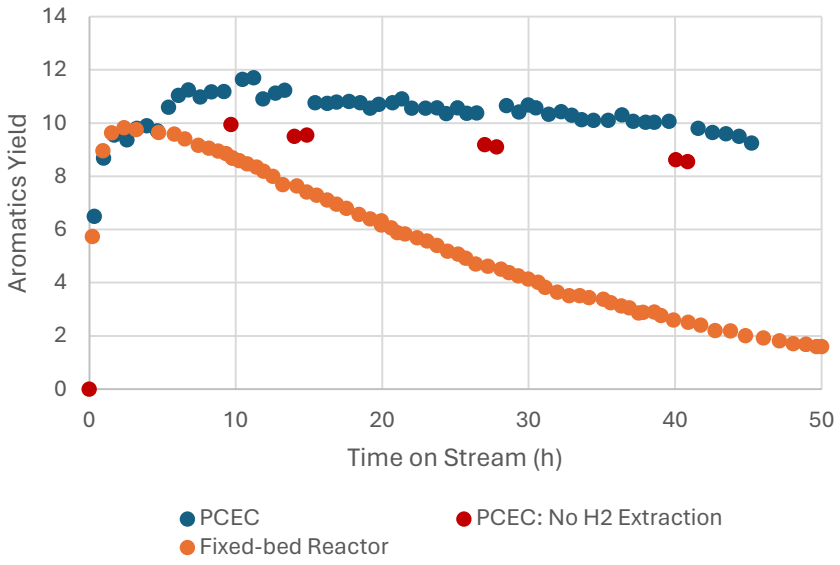

Figure 2.8: Comparing a protonic cell membrane reactor (PCEC) with the standard practice of a fixed bed reactor (FBR) for aromatics yield and catalyst durability [73]

The results in Figure 2.8 show exactly what has been theorized about the possibilities of hydrogen removal and oxygen injection: increased aromatics yield and greatly enhanced catalyst stability. However, this particular study was performed at 700+ °C, therefore the temperature reduction improvement was not realized at this 2016 study. Great PCEC catalyst improvements have occurred since then to lower the operating temperature [33], but these are yet to be tested with MDA applications.

MDA is a developing process that continues to improve with further enhancements to the catalyst. As the process continues to be optimized and catalysts developed, there is great potential for industrial application in the future. Zhang et al. even proposed that it could play an integral role in future sustainable carbon circulation systems. [66] More still needs to be learned about the MDA reaction to truly optimize the catalyst, especially regarding confirming intermediates and further studies into the hydrocarbon pooling mechanism [44], [50], [52], [53], [66]. As these studies take place, it is reasonable to assume that further

application avenues could be considered, and small-scale industrial applications will begin to take place. Additionally, there is great potential of MDA implementation with PCERs as the advancements in both categories allow for a synergistic effect resulting in an enhanced conversion rate and selectivity for MDA and increasingly lucrative byproducts from the PCER system.

Chapter 3: Modelling the Tubular PCFC

3.1 Modelling Overview

This chapter provides a detailed walkthrough of the model formulation. To model the PCFC, Engineering Equation Solver (EES) is used. EES is an iterative simultaneous solver that requires effective initial guesses and boundary conditions for all variables in order to converge a proper solution.

The modeling of PCFC systems is still a rapidly growing field of study [74]. Unfortunately, there are relatively few references of studies performed for modeled tubular PCFC systems. Experimentally, planar button cells are typically preferred due to their simpler manufacturing process and easier measurement requirements, which is also reflected in modeling studies. Nevertheless, there are numerous successful examples of SOFC models, despite their functional similarity, these models may exhibit significantly different values for various components and reactions. Of these, the works done by Stiller [75] and Xi [76] on SOFC modeling are used as the primary examples from which the foundational principles of the model used in this study are derived. Xi's work provided an exemplary discussion on the energy balance mechanics of fuel cells, while Stiller's work is one of the most detailed tubular fuel cell models available at the time of this writing.

The model formulation can be effectively broken into four important functions: reaction mechanisms, mass balance, electrochemical setup, and energy balance. The reaction mechanism setup is arguably the most critical aspect of the model and is responsible for realistically predicting the reaction rates, final selectivity, and also plays a

role in the temperature distribution through the cell. The mass balance takes care of the literal mass flow through the system, and accounts for changes in the product makeup as reactions occur in real time. The electrochemical setup is an integral aspect of both the reaction mechanism and the energy balance and predicts the cell voltage and current. These aspects help predict how much hydrogen is removed from the process stream and generate additional heat inside the cell. Lastly, the energy balance directly predicts the temperature distribution, which relies on the exo and endothermic reactions, and the theoretical maximum power output from the cell. Other modelling studies are also considered a momentum balance which calculates the pressure drop through the cell [77], [78]. In this study, the momentum balance is replaced with an overall pressure drop of 4 millibars.

3.2 Reaction Mechanism

3.2.1 Considered Reactions

As discussed in Chapter 2, the reaction mechanism for the MDA process closely follows the kinetic studies and work of Jeong et al. [64]. However, in a realistic application of natural gas, there are other side reactions occurring alongside the intended MDA reactions. The side reactions considered in this work are the electrochemically driven formation of water on the air side, partial oxidation of methane, steam reforming, and water gas shift reactions on the fuel side as shown in Figure 3.9.

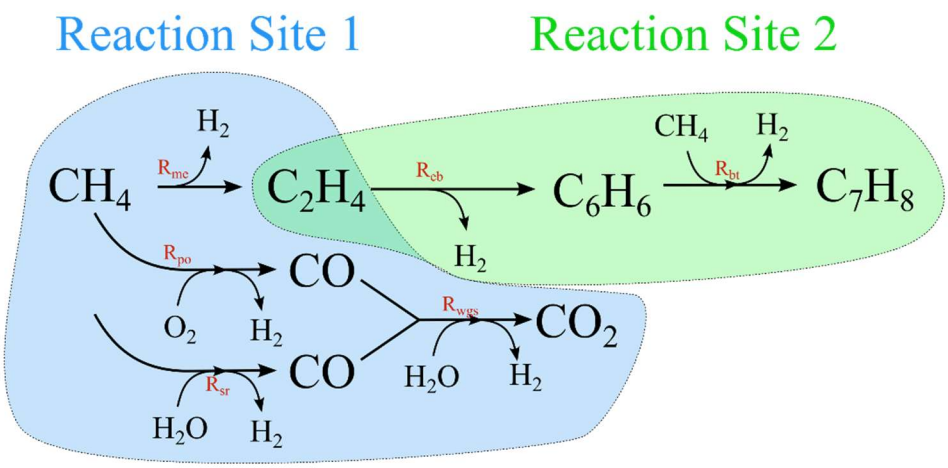

Figure 3.9: Model reaction system

In Jeong's kinetic study, the assumption is that the reactions occur in non-oxidative conditions, which enhances the selectivity of the products [43]. This would normally rule out the partial oxidation reaction since there is no pure oxygen in standard natural gas bulk flows. However, Duan et al. has noted that the electrolyte membranes used in PCFCs are not necessarily pure proton conductors, and have a small ability to conduct oxygen ions as well as protons [11], [12], [72]. Liu et al. has hypothesized that designing a PCFC electrolyte or catalyst with this feature in mind could significantly mitigate coking as the conducted oxygen from the air could react with the coke to create CO [13]. This understanding of the partial oxidation reaction can be characterized by its chemical equation of

$$CH_4 + \frac{1}{2}O_2 \rightarrow CO + 2H_2 \tag{3.1}$$

In most studies where methane is considered as the fuel for a PCFC, water is also mixed in to enhance the results [12]. So, a small amount of water is considered in the inlet stream, which naturally induces the steam reforming and water gas shift reactions,

especially at the higher operating temperatures like 700°C. The steam reforming and water gas shift reactions are given respectively by

$$CH_4 + H_2O \rightarrow CO + 3H_2 \tag{3.2}$$

$$CO + H_2O \rightarrow CO_2 + H_2 \tag{3.3}$$

3.2.2 Reaction Rates

The reaction rates for steam reforming and water gas shift reactions in the presence of a catalyst are well documented. In this study, the work of Timmerman et al. [79] is used to model the steam reforming, while the water gas shift followed the work of Lehnert [80]. These yielded the following formulas for the reaction rate:

$$r_{sr} = k_{sr} * P_{CH_4} P_{H_2O} * \left(1 - \frac{P_{CO} P_{H_2}}{K_{eq,sr} P_{CH_4} P}\right) * A * \alpha_{sr} \tag{3.4}$$

$$r_{wgs} = k_{wgs} P_{CO} P_{H_2O} * A * \alpha_{wgs} \tag{3.5}$$

where r is the reaction rate for the corresponding reaction, k is the rate constant, P_s is the partial pressure of species s, $K_{eq,sr}$ is the equilibrium constant for steam reforming, A is the active area for the reaction, and α is an arbitrary value that compensates for adjustments in the catalyst used between Timmerman and Lehnert's studies and the intended catalyst for this model. The water gas shift reaction stands out from the others considered in the model since the equilibrium constant is not included in the reaction rate. This is due to the extremely fast kinetics of the water gas shift reaction leading to a negligible reverse reaction taking place [77].

The MDA reactions consider the methane conversion to ethylene, ethylene to benzene, and benzene to toluene. While Jeong's work also includes naphthalene formation, this reaction is omitted due to no naphthalene being recorded in the experimental validation data. These MDA reactions, along with the partial oxidation of methane reaction, are modeled with a Langmuir-Hinshelwood expression that simulates the bifunctional nature of the catalyst. The reaction rates are as follows:

$$r_{me} = \frac{k_{me}\left(P_{CH_4}^2 - \frac{P_{C_2H_4}P_{H_2}^2}{K_{eq,me}}\right) * g_{cat}}{1+\left(K_{H_2}^{ad_1}P_{H_2}+K_{CH_4}^{ad_1}P_{CH_4}+K_{C_2H_4}^{ad_1}P_{C_2H_4}+K_{CO}^{ad_1}P_{CO}+K_{CO_2}^{ad_1}P_{CO_2}+K_{H_2O}^{ad_1}P_{H_2O}\right)} \tag{3.6}$$

$$r_{eb} = \frac{k_{eb}\left(P_{C_2H_4}^3 - \frac{P_{C_6H_6}P_{H_2}^3}{K_{eq,eb}}\right) * g_{cat}}{1+\left(K_{H_2}^{ad_2}P_{H_2}+K_{CH_4}^{ad_2}P_{CH_4}+K_{C_2H_4}^{ad_2}P_{C_2H_4}+K_{C_6H_6}^{ad_2}P_{C_6H_6}+K_{C_7H_8}^{ad_2}P_{C_7H_8}\right)} \tag{3.7}$$

$$r_{bt} = \frac{k_{bt}\left(P_{C_6H_6}P_{CH_4} - \frac{P_{C_7H_8}P_{H_2}}{K_{eq,bt}}\right) * g_{cat}}{1+\left(K_{H_2}^{ad_2}P_{H_2}+K_{CH_4}^{ad_2}P_{CH_4}+K_{C_2H_4}^{ad_2}P_{C_2H_4}+K_{C_6H_6}^{ad_2}P_{C_6H_6}+K_{C_7H_8}^{ad_2}P_{C_7H_8}\right)} \tag{3.8}$$

$$r_{po} = \frac{k_{co}\left(P_{CH_4}P_{O_2,air}^{0.5} - \frac{P_{CO}P_{H_2}^2}{K_{eq,co}}\right) * g_{cat}}{1+\left(K_{H_2}^{ad_2}P_{H_2}+K_{CH_4}^{ad_2}P_{CH_4}+K_{C_2H_4}^{ad_2}P_{C_2H_4}+K_{C_6H_6}^{ad_2}P_{C_6H_6}+K_{C_7H_8}^{ad_2}P_{C_7H_8}\right)} \tag{3.9}$$

where the subscripts $me, eb, bt,$ and po represent the methane to ethylene, ethylene to benzene, benzene to toluene, and partial oxidation of methane reactions respectively. The $K_s^{ad_{1/2}}$ term represents the adsorption constant for the species s on reaction sites 1 and 2 in the catalyst, and g_{cat} is the grams of catalyst where the reaction is being considered.

Lastly, the water formation reaction is driven purely by the current through the cell [75], [76]. This is given by the following formula

$$r_{orr} = \frac{i_{cell}}{nF} \tag{3.10}$$

where i_{cell} is the current in A, n is the number of electrons transferred in the reaction, and F is faraday's constant.

3.2.3 Reaction Constants

For the reactions where a rate constant k is necessary, the general form for calculating k is the Arrhenius equation

$$k = k_0 \exp\left(-\frac{E_{act}}{RT_{PEN}}\right) \tag{3.11}$$

where k_0 is the preexponential factor for the specific reaction, E_{act} is the activation energy, R is the universal gas constant, and T_{PEN} is the temperature of the PEN structure where the reaction is taking place. In Jeong's kinetic study, the difference of the inverse of temperature with respect to a reference temperature of 700°C is used instead of the standard T_{PEN} as shown in Table 3.2 below [64]. Jeong's approach is used for the MDA reactions and the partial oxidation reaction, while the standard Arrhenius form is used for the steam reforming reaction. For the water gas shift reaction, a value of $0.0171 \cdot \exp\left(-\frac{103191}{T_{PEN}}\right) \frac{mol}{s*m^3*Pa^2}$ has been used in previous studies and is also applied here [78]. To adjust for the units used by the reaction rate and implementation in the model, this value turns into

$$k_{wgs} = 0.0171 \cdot \exp\left(-\frac{103191}{T_{PEN}}\right) \cdot h_{fuelch} \cdot 10^{10} \tag{3.12}$$

where h_{fuelc} is the height of the fuel channel in meters, k_{wgs} is the rate constant in $\frac{mol}{s*m^2*bar^2}$, and the 10^{10} term is added to adjust the units from Pa to bar.

The adsorption constants generally follow a similar modified-Arrhenius trend, except for CO, CO_2, and H_2O. Since CO_2 and H_2O are not included in Jeong's kinetic study [64], they

are simply given constant values similar to CO. The remaining adsorption constants are calculated based on the work of Jeong's study, and followed Jeong's approach of using the inverse temperature as follows

$$K_s^{ad} = K_0^{ad} \exp\left(\frac{E_{act}}{r}\left(\frac{1}{T_{PEN}} - \frac{1}{T_{ref}}\right)\right) \tag{3.13}$$

Lastly, for the equilibrium constants K_{eq}, the first step is to determine the Gibb's free energy change for each reaction. The EES database is used to calculate the Gibb's free energy of the different reactions such that for each reaction,

$$\Delta G = \Sigma \Delta G_{products}^{\nu_s} - \Sigma \Delta G_{reactants}^{\nu_s} \tag{3.14}$$

where ΔG is the standard Gibb's free energy, and ν_s is the stoichiometric coefficient for each species s in the reactants or products respectively. Then the standard Arrhenius equation is used to calculate the equilibrium constant K_{eq}.

$$K_{eq} = \exp\left(-\frac{\Delta G}{RT_{PEN}}\right) \tag{3.15}$$

The final values used to determine all the above constants is shown in Table 3.2. All the activation energies are determined by Jeong [64] for the MDA reaction and adsorption constants, Timmerman [79] for the steam reforming reaction, and Mallens [81] for the water gas shift reaction. However, many of the preexponential factors are significantly adjusted to align with the catalyst data used for validation.

Table 3.2: Kinetic data used in model

Constant	Units	Value	Reference
k_{me}	$\frac{mol}{g_{cat} * s * bar^2}$	$1.68 * 10^{-3} \exp\left(-\frac{92710}{R}\left(\frac{1}{T_{PEN}} - \frac{1}{T_{ref}}\right)\right)$	This work

k_{eb}	$\frac{mol}{g_{cat} * s * bar^2}$	$1.75 * 10^2 \exp\left(-\frac{31350}{R}\left(\frac{1}{T_{PEN}} - \frac{1}{T_{ref}}\right)\right)$	This work
k_{bt}	$\frac{mol}{g_{cat} * s * bar^2}$	$3.54 * 10^{-3} \exp\left(-\frac{501400}{R}\left(\frac{1}{T_{PEN}} - \frac{1}{T_{ref}}\right)\right)$	This work
k_{po}	$\frac{mol}{g_{cat} * s * bar^2}$	$8.75 * 10^{-4} \exp\left(-\frac{189200}{R}\left(\frac{1}{T_{PEN}} - \frac{1}{T_{ref}}\right)\right)$	This work
k_{sr}	$\frac{mol}{m^2 * s * bar^2}$	$1483 \exp\left(-\frac{61000}{RT_{PEN}}\right)$	[79]
k_{wgs}	$\frac{mol}{m^2 * s * bar^2}$	$0.0171 \cdot \exp\left(-\frac{103191}{T_{PEN}}\right) \cdot h_{fuelch} \cdot 10^{10}$	[78]
α_{sr}	-	0.4	Arbitrary value
α_{wgs}	-	0.3	Arbitrary value
$K_{H_2}^{ad_1}$	bar^{-1}	$7.58 * 10^{-2} \exp\left(\frac{21410}{R}\left(\frac{1}{T_{PEN}} - \frac{1}{T_{ref}}\right)\right)$	[64]
$K_{CH_4}^{ad_1}$	bar^{-1}	$9.66 * 10^{-2} \exp\left(\frac{94610}{R}\left(\frac{1}{T_{PEN}} - \frac{1}{T_{ref}}\right)\right)$	[64]
$K_{C_2H_4}^{ad_1}$	bar^{-1}	$7.94 * 10^{-2} \exp\left(\frac{40020}{R}\left(\frac{1}{T_{PEN}} - \frac{1}{T_{ref}}\right)\right)$	[64]
$K_{H_2}^{ad_2}$	bar^{-1}	$9.40 * 10^{-2} \exp\left(\frac{21080}{R}\left(\frac{1}{T_{PEN}} - \frac{1}{T_{ref}}\right)\right)$	[64]
$K_{CH_4}^{ad_2}$	bar^{-1}	$1.19 * 10^{-1} \exp\left(\frac{44070}{R}\left(\frac{1}{T_{PEN}} - \frac{1}{T_{ref}}\right)\right)$	[64]

$K_{C_2H_4}^{ad_2}$	bar^{-1}	$2.27 * 10^{-1} \exp\left(\frac{128700}{R}\left(\frac{1}{T_{PEN}} - \frac{1}{T_{ref}}\right)\right)$	[64]
$K_{C_6H_6}^{ad_2}$	bar^{-1}	$4.88 * 10^{-2} \exp\left(\frac{174000}{R}\left(\frac{1}{T_{PEN}} - \frac{1}{T_{ref}}\right)\right)$	[64]
$K_{C_7H_8}^{ad_2}$	bar^{-1}	$5.22 * 10^{-2} \exp\left(\frac{34850}{R}\left(\frac{1}{T_{PEN}} - \frac{1}{T_{ref}}\right)\right)$	[64]
$K_{CO}^{ad_1}$	bar^{-1}	$1.575 * 10^{-1}$	This work
$K_{CO_2}^{ad_1}$	bar^{-1}	$1.575 * 10^{-1}$	This work
$K_{H_2O}^{ad_1}$	bar^{-1}	$9 * 10^{-2}$	This work

3.3 Mass Balance

3.3.1 Model Discretization

The first step in the mass balance is understanding the discretization of the system. For a tubular PCFC, it is assumed that all conditions would be radially symmetric, therefore only 2 dimensions of discretization are needed. The assumption of radial symmetry has been proven to have a few drawbacks with regard to overpotential calculations for the electrochemistry [82], but it is still reliable enough to be a standard assumption used in a variety of other tubular fuel cell models [75], [83]. The approach to the discretization in this study is largely taken from Stiller's work, as seen below in Figure 3.10 [75]:

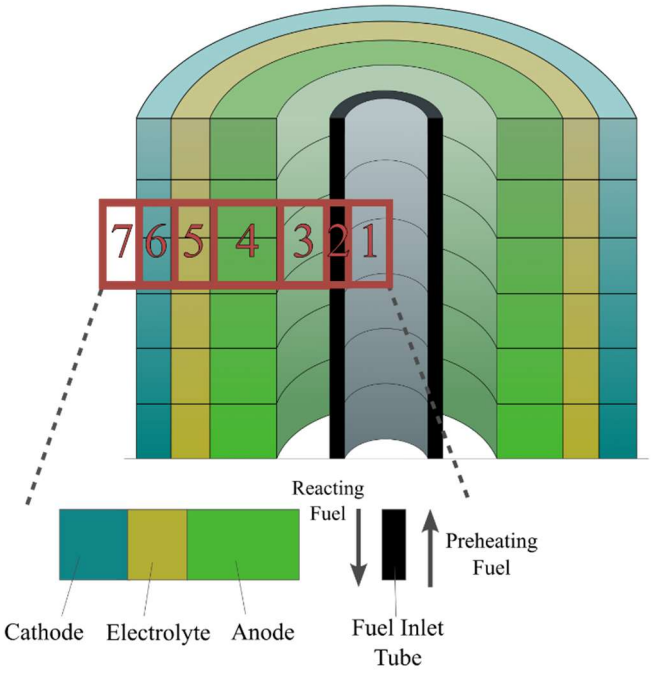

Figure 3.10: Discretization of the tubular PCFC. Seven sections are considered for the radial direction, while the height (Z-axis) is also discretized.

The red box in Figure 3.10 highlights the seven areas of discretization expanding out from the center of the cell. The seven units in numerical order are (1) the preheating fuel, (2) the fuel delivery tube (FDT), (3) reacting fuel, (4) anode, (5) electrolyte, (6) cathode, and (7) the air stream. The radii of these units vary with the thicknesses of the different units and are referred to as r_i where i is the corresponding unit. The Z axis is split into 15 sections where 0 is the inlet, and 15 is the outlet from the cell.

Given the above discretization setup, several important parameters need to be clarified. First, the active area is normally a simple calculation in planar cells. In this tubular case, it is calculated using the average radius between the inner and outer surfaces as follows

$$A = 2 * \pi * \frac{r_6 + r_3}{2} * L_{cell} \tag{3.16}$$

where A is the active area, $r_6$and r_3 are the outer and inner radii respectively, and L_{cell} is the length of the cell.

Another important parameter not depicted in Figure 3.10 is the interconnect. Interconnects in tubular fuel cells are significantly different from planar configurations. Kee et al. has suggested a spiraling wire on both sides of the PEN structure for the interconnect [84]. However, in the discretization setup, this has been simplified such that the contact area between the interconnect and the electrodes is one fourth of the total active area. In other words, the spiraling interconnect occupies a fourth of the available surface area on the anode and cathode. For the total cross-sectional area of the interconnect, which plays a role in overpotential calculations, a rectangle is considered such that

$$A_{IC} = \frac{A}{4} * (r_3 - r_2) \tag{3.17}$$

3.3.2 Discretized Mass Balance

The term “mass balance” may be misleading since the majority of the calculation work actually takes place in mole units rather than mass units. The inlet mass flow rate and molar concentrations of the process flow are considered as input parameters so the number of moles of each component can be calculated by the following formula:

$$N_s = \frac{m_s}{MM_s} \tag{3.18}$$

$$s \in \{CH_4, C_2H_4, C_6H_6, C_7H_8, CO, CO_2, H_2, H_2O, N_2, O_2\}$$

where N is the number of moles, m is the mass, and MM is the molar mass of a particular species s. For calculations where the total number of moles in the stream is required, this is calculated by adding the moles of each species together:

$$N_{bulk} = \Sigma(N_s) \tag{3.19}$$

where N is the number of moles of species s. Since the inlet concentrations are known, and the reactions dictate further changes in concentration through the cell, EES can combine these equations to converge a solution for these variables. The partial pressure for each species i can also be determined as the product of the mole percent and the pressure. The partial pressure is critical to the reaction mechanisms as it determines the equilibrium of the reactions as discussed earlier.

With these terms formulated, the final step in the mass balance is to model the change in concentrations due to the reactions in the air and fuel bulk flow streams. For the fuel side, which does not contain significant amounts of nitrogen or oxygen, the following system of equations is used for each unit of discretization along the Z axis:

$$0 = N_{CH4,i-1} - N_{CH4,i} - 2 * r_{me,i} - r_{bt,i} - r_{po,i} - r_{sr,i} \tag{3.20}$$

$$0 = N_{C2H4,i-1} - N_{C2H4,i} + r_{me,i} - 3 * r_{eb,i}$$

$$0 = N_{C6H6,i-1} - N_{C6H6,i} + r_{eb,i} - r_{bt,i}$$

$$0 = N_{C7H8,i-1} - N_{C7H8,i} + r_{bt,i}$$

$$0 = N_{CO,i-1} - N_{CO,i} + r_{po,i} - r_{wgs,i} + r_{sr,i}$$

$$0 = N_{CO_2,i-1} - N_{CO_2,i} + r_{wgs,i}$$

$$0 = N_{H2O,i-1} - N_{H2O,i} - r_{wgs,i} - r_{sr,i}$$

$$0 = N_{H_2,i-1} - N_{H_2,i} + 2 * r_{me,i} + 3 * r_{eb,i} + r_{bt,i} + 2 * r_{po,i} - r_{orr,i} + r_{wgs,i} + 3 * r_{sr,i}$$

where i is the discretization unit along the Z axis.

This setup accounts only for the reactions considered in this study. If other reactions were to be added in, the general form for the above system of equations could be written as

$$0 = \left(N_{s,i-1} - N_{s,i}\right) + \Sigma\left(\nu_{s,k} r_k\right),\ k \in \{All\ reactions\} \tag{3.21}$$

where s is the component species $(CH_4, H_2, \ldots)$, k is all included reactions, and ν is the stoichiometric coefficient for the corresponding elementary component. Applying this general form to the air side yields the following equations:

$$0 = \mathrm{N}_{\mathrm{O}_2,i-1} - \mathrm{N}_{\mathrm{O}_2,i} - .5 * \mathrm{r}_{\mathrm{orr},i} - .5 * \mathrm{r}_{\mathrm{po},i} \tag{3.22}$$

$$0 = N_{N_2,i-1} - N_{N_2,i}$$

$$0 = N_{H_2O,i-1} - N_{H_2O,i} + r_{orr,i}$$

3.4 Electrochemical Model

3.4.1 Nernst Equation

Electrochemical modelling of fuel cells typically begins setting up the Nernst equation, which represents the theoretical maximum voltage an electrochemical reaction can generate, or the electromotive force. In this study, it is assumed that only the conducted protons contribute to the generated current. Specifically, that means the oxygen ions that are conducted to mitigate coking are ignored, and no other component in the fuel plays a role in the electrochemical process. Therefore, the Nernst equation in this system is represented by

$$E_{nernst} = \left(\frac{-\Delta G_{orr}}{n*F}\right) + \frac{R*T_{PEN}}{n*F}\left(\ln\left(\frac{P_{H_2} P_{O_2}^{.5}}{P_{H_2O}}\right) + \ln\left(\frac{P_{cell}}{P_{ambient}}\right)\right) \tag{3.23}$$

where $\Delta G_{orr}$is the Gibbs free energy change for the water formation reaction, the partial pressures represent the hydrogen on the fuel side, and the oxygen and water on the air side,

and P_{cell} and $P_{ambient}$ represent the cell and ambient pressures, respectively. For the water formation reaction, $n = 2$ since there are 2 protons required for the reaction.

Since E_{nernst} represents the maximum voltage, there are realistic losses that need to be considered. These losses, or overpotentials, typically take three forms: Ohmic, Activation, and Concentration [75], [76], [77], [78], [85]. This makes the true voltage output from the system calculated by:

$$V_{cell} = E_{nernst} - \eta_{Ohm} - \eta_{\mathrm{Act}} - \eta_{Conc} \tag{3.24}$$

To calculate the power density, the average current density through the cell is considered as an input parameter. The model then fluctuates the current through the cell to meet the declared average value according to the demands of the overpotential calculations, which rely heavily on the current.

3.4.2 Ohmic Overpotential

The Ohmic overpotential is the direct result of energy loss due to the conductivity of the materials. Therefore, the calculation of the ohmic overpotential is derived directly from Ohm's law [77]:

$$\eta_{Ohm} = i_{cell} * R_{ohm} \tag{3.25}$$

where R_{ohm} is the total ohmic resistance through the cell and its interconnects, and i_{cell} is the current through the cell. In this model, the approach for calculating the total cell ohmic resistance is taken from the work of Campanari and Iora [86], which assumes that the current flow path is perpendicular to the PEN surface. This allows the two resistances (the PEN and the interconnect) to be considered in series with each other:

$$\eta_{ohm} = R_{ohm,PEN} + R_{ohm,IC} \tag{3.26}$$

where R represents the total resistance in ohms due to the PEN structure and interconnect respectively.

For the PEN, the specific resistivity of PCFC electrodes is analyzed by Liu et al. For simplicity, the anode, electrolyte, and cathode are considered as one whole with respect to the resistance, rather than analyzing the resistance of each of them individually. The results from their study are used to estimate the relationship of the specific resistivity of the whole PEN structure with temperature [33]:

$$sr_{PEN} = 0.00381 \exp\left(\frac{27600}{R * T_{PEN}}\right) \tag{3.27}$$

where sr_{PEN} is the specific resistivity of the PEN structure in Ωcm^2. This then yields a value for total resistance as

$$R_{ohm,PEN} = i_{cell} * \frac{sr_{PEN}}{A} \tag{3.28}$$

For the interconnect, temperature dependent data is difficult to find. Instead, a value of $1.176 * 10^{-4}\ \Omega cm$ based on previous SOFC models [85] is used. The resistance due to the interconnect is then calculated by

$$R_{ohm,IC} = i_{cell} * 1.176 * 10^{-4} * \frac{r_3 - r_2}{\frac{A}{4}} \tag{3.29}$$

where $\frac{A}{4}$ represents the area of the interconnect in cm, and $r_3 - r_2$ is considered as the maximum height of the interconnect.

When the two resistances are added together, the resistance from the PEN structure is 2-3 orders of magnitude larger than the ohmic losses from the interconnect. This is expected as a large portion of the raw material cost of PCFCs is attributed to obtaining interconnect materials designed with especially high conductivities [20].

3.4.3 Activation Overpotential

The activation overpotential comes from the extra potential needed to overcome the activation energy barriers of the electrochemical reaction [76], [77], [87]. In both SOFC and PCFC models, this overpotential has been represented using the Butler-Volmer equation [77], [78], [85], [87], [88]:

$$i_{cell} = i_0 \left[\exp\left(\frac{\alpha_{an} F \eta_{act}}{RT_{PEN}}\right) - \exp\left(-\frac{\alpha_{ca} F \eta_{act}}{RT_{PEN}}\right) \right] \tag{3.30}$$

where α_{an} and α_{ca} are the anodic and cathodic symmetry factors, respectively, and i_0 is the exchange current factor. The symmetry factors must sum to unity, and in SOFC systems these are typically assumed to be 0.5 [87]. However, in PCFC systems, these terms change. Zhu et al. simulated a PCFC using moist H_2 at atmospheric pressure and generated effective values for these and other important electrochemical parameters, which are also used in this study [88].

The Butler-Volmer equation is used on both sides of the PEN structure in Zhu' s model [88], and the same approach is used here. This allows for the unique kinetics of the electrochemical reaction on both electrodes to factor into the overpotential calculation, which provides greater insight into the electrodes' effect on the reaction [88]. The overall activation overpotential is then the sum of the overpotentials at the anode and cathode. The respective overpotentials are calculated using the following:

$$i_{cell} = j_{0_{an}} * \left(\exp\left(\frac{\alpha_{an}^{an} F \eta_{act,an}}{RT_{PEN}}\right) - \exp\left(-\frac{\alpha_{ca}^{an} F \eta_{act,an}}{RT_{PEN}}\right) \right) * A \tag{3.31}$$

$$i_{cell} = j_{0_{ca}} * \left(\exp\left(\frac{\alpha_{an}^{ca} F \eta_{act,ca}}{RT_{PEN}}\right) - \exp\left(-\frac{\alpha_{ca}^{ca} F \eta_{act,ca}}{RT_{PEN}}\right) \right) * A \tag{3.32}$$

where $j_{0_{an}}$ and $j_{0_{ca}}$ are the exchange current densities for the anode and cathode respectively, α_{an}^{an} and α_{ca}^{an} are the anodic and cathodic symmetry factors for the anode, α_{an}^{ca} and α_{ca}^{ca} are the anodic and cathodic symmetry factors for the cathode, and $\eta_{act,an}$ and $\eta_{act,ca}$ are the activation overpotentials for the anode and cathode.

Not all of the parameters used by Zhu et al [88] fit the above model, so the modelling work of Zhang [89], whose parameters are confirmed by Sahli [90], is also used in determining appropriate constants for the activation overpotential calculation. Zhang estimated the relationship between temperature and the exchange current density to take a standard Arrhenius form similar to the rate constants discussed in section 3.2.3 [89]:

$$j_0 = j_0^* * \exp\left(-\frac{E_{an/ca}}{RT_{PEN}}\right) \tag{3.33}$$

where j_0^* represents a pre-exponential factor, and $E_{an/ca}$ is the activation energy for the cathodic or anodic electrochemical reaction.

The final constants and the references from which they are taken are shown in Table 3.3 below:

Table 3.3: Constants used for the calculation of the activation overpotential

Term	Units	Value	Reference
$j_{0_{an}}$	$\frac{A}{m^2}$	$9.577 * 10^8 \exp\left(-\frac{E_{an}}{RT_{PEN}}\right)$	[89], [90]
$j_{0_{ca}}$	$\frac{A}{m^2}$	$8.817 * 10^9 \exp\left(-\frac{E_{an}}{RT_{PEN}}\right)$	[89], [90]
E_{an}	$\frac{J}{mol}$	82600	[88]
E_{ca}	$\frac{J}{mol}$	43300	[88]
α_{an}^{an}	-	.3	[88]
α_{ca}^{an}	-	.7	[88]
α_{an}^{ca}	-	.8	[88]

α_{ca}^{ca}	-	. 2	[88]

3.4.4 Concentration Overpotential

The concentration overpotential is sometimes called the diffusion polarization. This loss occurs due to diffusion resistance in the PEN structure, which causes different concentration levels of reacting species at the reaction site compared to the bulk flow [77], [78]. Unlike the ohmic and activation overpotentials which have clearly defined methods of calculation, the concentration overpotential has been calculated using several different methods. Liu et al. performed a study aiming to mitigate the diffusion losses in PCFCs, particularly at low temperatures [33]. The ceramics used in PCFCs require high temperatures to effectively act as ionic conductors, so the diffusion polarization becomes a greater problem the lower the temperature. The reigning strategy in mitigating this loss is to decrease the thickness of the electrolyte as much as possible while still maintaining effectiveness and full coverage across the active surface [33].

The approach to calculating the concentration overpotential in this study closely resembles the approach taken by Aguiar et al from 2004 [91]. Aguiar's study modelled a SOFC and factored in the losses from both the cathode and the anode in one equation. The approach calls for first estimating the adjusted partial pressure (or concentration) of the electrochemical reacting species at the triple phase boundary reaction site. Adjusting his system to a PCFC model, these concentrations are calculated by:

$$P_{O_2,TPB} = P_{O_2} - \frac{RT_{PEN}\tau_{ca}}{4FD_{ca}} j_{cell} \tag{3.34}$$

$$P_{H_2O,TPB} = P_{H_2O} + \frac{RT_{PEN}\tau_{ca}}{2FD_{ca}} j_{cell} \tag{3.35}$$

$$P_{H_2,TPB} = P - \left(P - P_{H_2}\right) \exp\left(\frac{RT_{PEN}\tau_{an}}{2FD_{an}P} j_{cell}\right) \tag{3.36}$$

where the TPB subscript represents the partial pressure of the corresponding species at the triple phase boundary, P represents the system pressure, τ_{an} and τ_{ca} represent the thicknesses of the anode and cathode, and D_{an} and D_{ca} represent the diffusion coefficient of the cathode and anode materials, and j_{cell} represents the current density in $\frac{A}{m^2}$.

With the TPB partial pressures calculated, the formula for the concentration overpotential can be adjusted to PCFC configuration from Aguiar's work on SOFC models as follows [91]:

$$\eta_{conc} = \frac{RT_{PEN}}{2F} \ln\left(\frac{P_{H_2}}{P_{H_2,TPB}}\right) + \frac{RT_{PEN}}{2F} \ln\left(\frac{P_{H_2O,TPB} P_{O_2}^{0.5}}{P_{H_2O} P_{O_2,TPB}^{0.5}}\right) \tag{3.37}$$

In the concentration formula, the left side of the equation represents the overpotential due to the anode, while the left side of the equation represents overpotential due to the cathode. In the calculation of the concentration overpotential, the diffusion coefficients become extremely important, regardless of the chosen method of calculation [11], [88], [89], [92]. The coefficients represent the ion's ability to be conducted across the electrode/electrolyte. Duan et al. [11] and others have estimated the value of this coefficient in PCFC materials, but the results can vary depending on the method of calculation and the chosen electrode material and manufacturing methods. In Aguiar's approach, the anode has a significantly larger diffusivity coefficient than its cathode counterpart [91], so a similar relationship is assumed here. Combining this relationship with the estimates from Duan et al.'s work, the following arbitrary values are selected for the model:

$$D_{an} = 0.3\frac{cm^2}{s}, \qquad D_{ca} = 0.03\frac{cm^2}{s}$$

3.4.5 Electrochemical Model Setup

The Nernst equation and the overpotentials for the model are calculated at each discretization point along the cell model. This allows the current to fluctuate with the changing cell temperature, the availability of hydrogen, and the demand of the overpotentials. The model also outputs an overarching voltage that stays consistent across the whole cell. So, while E_{nernst} and the overpotentials constantly vary through the cell, the V_{cell} remains a constant variable determined by the model.

The product of the determined voltage and selected input current provides the output power density as follows:

$$Power\ Density = V_{cell} * i_{cell,avg} \tag{3.38}$$

Where $i_{cell,avg}$ represents the average current through the cell. The average current density is one of the most important input parameters, as it directly affects how much hydrogen is removed from the bulk fuel stream. This strongly affects the reaction kinetics and output selectivity for the MDA reactions [64], [73].

3.5 Energy Balance

The purpose of the energy balance is to analyze the energy inputs and outputs for the cell as a whole, as well as the discretized points within it. This also includes determining the temperature distribution through the cell and its layers. As is noted in section 3.3.1, the cell is divided into seven layers. In the energy balance, the PEN structure is considered as one

whole layer, and the interconnects are factored in as an additional "layer". This leaves three solid layers (the PEN, Interconnects and the FDT) and three flowing layers (the pre-fuel, reacting fuel, and the air). Figure 3.11 shows the considered types of heat transfer for the energy balance between the different layers.

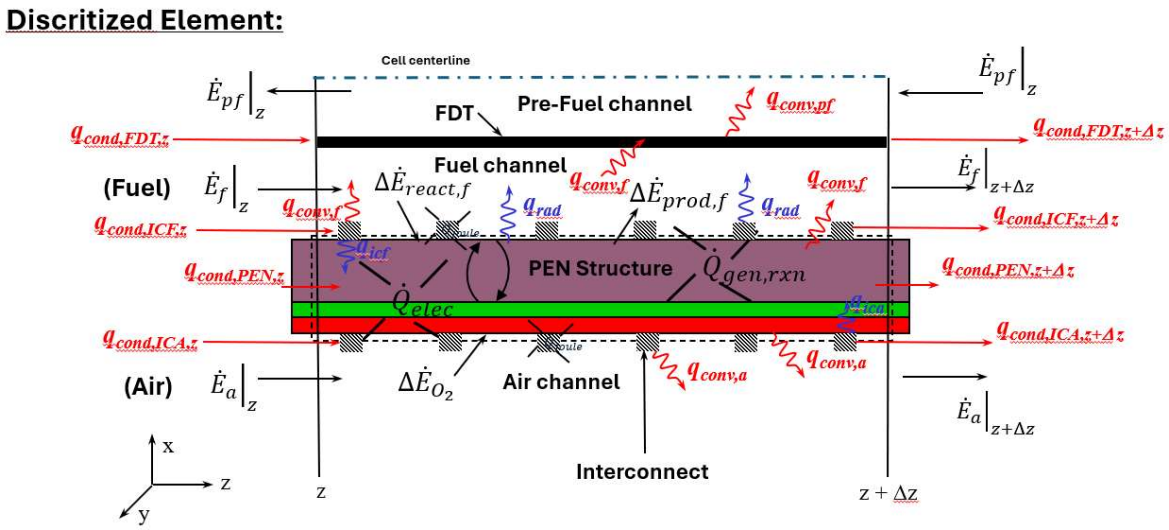

Figure 3.11: Energy balance for a whole discretized unit of the cell

3.5.1 Constants for Flowing Layers

For the flowing layers, a variety of fluid constants are required for the energy analysis. These include the hydraulic diameter (h_d), thermal conductivity (λ), viscosity (μ), convective heat transfer coefficient (h), Nusselt number (Nu), Reynold's number (Re), Prandtl number (Pr), density (ρ), and heat capacity (c_p).

The hydraulic diameter is the most straightforward of these. It is used in equations in place of a standard diameter when the cross-sectional area of the flow is not represented by a circle. The general formula is

$$d_h = \frac{4A}{P_m} \tag{3.39}$$

where A is cross sectional area and P_m is the perimeter of the surface over which the fluid is flowing. For the pre-fuel, the cross-sectional area is a circle, so there is no change between the diameter and the hydraulic diameter. For the air and the reacting fuel, the cross-sectional area is an annular space. In these instances, the formula for the hydraulic diameter simplifies to

$$d_h = 2(r_{outer} - r_{inner}) \tag{3.40}$$

where r represents the radius of the outer and inner circles describing the annular space.

The thermal conductivity and viscosity determinations for the gas mixtures can be considered together in equations 3.41-3.42 since their formulation is nearly identical. The approach used in this study is taken from the collaborative work of Poling et al.'s "Properties of Gases and Liquids" [93]. The selected approach requires the use of the thermal conductivity and viscosity of the species considered in the gas mixtures. For these values, data is gathered from the Aspen-HYSYS database to determine a relationship of these values with temperature. The thermal conductivity is calculated by:

$$\lambda_{mix} = \sum_{i=1}^{n} \frac{y_i \lambda_i}{\sum_{j=1}^{n} (y_j \phi_{ij})} \tag{3.41}$$

Where γ_i and γ_j represent the molar concentration of species i and j, λ is the thermal conductivity, n is the number of varying species in the fluid flow and

$$\phi_{ij} = \frac{\epsilon \left[1 + \left(\frac{\lambda_i}{\lambda_j} \right)^{\frac{1}{2}} \left(\frac{M_j}{M_i} \right)^{\frac{1}{4}} \right]^2}{\left[8 \left(1 + \frac{M_i}{M_j} \right) \right]^{\frac{1}{2}}} \tag{3.42}$$

where ϵ is a constant at or near unity, and M is the molar mass of a particular species in the gas mixture. For viscosity, the formula setup is identical, but the thermal conductivity γ values are swapped out with viscosity μ values, and ϵ *must* equal one, rather than sometimes only being *close* to one.

The convective heat transfer coefficients are calculated from the remaining fluid parameters, starting with the following:

$$h = \frac{Nu*\lambda}{d_h} \tag{3.43}$$

λ and d_h are known, and the Graetz-Lèvêque correlation is assumed here to estimate Nu:

$$Nu = 1.86\left(Re * Pr * \frac{d_h}{L}\right)^{\frac{1}{3}} \tag{3.44}$$

where L is the length of the considered flowing section. This correlation assumes laminar flow with a $Re < 2100$ [94]. The Reynolds number and Prandtl number used in the calculation of Nu are calculated by the general equations

$$Re = \frac{\rho \vec{V} d_h}{\mu} \tag{3.45}$$

$$Pr = \frac{\mu c_p}{\lambda} \tag{3.46}$$

where ρ is the density of the gas mixture calculated by the ideal gas law, and $\vec{V}$ is the velocity of the flow. The c_p is calculated by

$$c_p = \sum_{i=1}^{n} \gamma_i c_{p,i} \tag{3.47}$$

where n represents the number of species in the gas mixture.

All the above constants are calculated at each discretized point along the cell, since all of them are dependent on temperature and the changing molar concentrations.

3.5.2 Energy Balance in Gas Flows

The energy balance in the pre-fuel, reacting fuel, and air flow streams is considered here. For the pre-fuel, the coefficient for convection experiences a negligible change through the cell since the composition never changes inside the FDT. Therefore, the coefficient for convection for the pre-fuel is assumed to be equal to the coefficient for the reacting fuel inlet ($h_{F,0}$) to ease the computation demands. For the fuel inside the delivery tube, the energy balance considers the convective heat transfer coming in from the FDT, and the heat transfer between each of the discretized units of pre-fuel in the cell. This is represented as the following:

$$0 = \left[h_{PF} * 2\pi r_1 \Delta z * \left(T_{FDT,i} - T_{PF,i}\right)\right]_{conv\ in} + \left[N_{PF,i-1}\Delta h_{PF,i-1}(T_{PF}) - \mathrm{N_{PF,i}}\Delta h_{PF,i}(T_{PF})\right]_{Energy\ In - Energ\quad Out} \tag{3.48}$$

where r_1 represents the radius of the first layer as depicted in Figure 3.10, h_{PF} represents the coefficient of convective heat transfer for the pre-fuel, Δz represents the length of a discretized unit of the cell length, and $\Delta h_{PF,i}(T_{PF})$ represents the enthalpy Δh of the pre-fuel stream at the determined temperature T at each discretized point i.

The reacting fuel considers the convective heat transfer from the PEN structure, interconnects and the FDT, the change in enthalpy due to the reactions, and the heat transfer between the discretized units. The approach for the reactions is taken from the models created by Kazempoor [77], [78], [85] and Xi [76]. Additionally, the radiation heat from the interconnects and PEN assembly is assumed to be absorbed by the FDT, and therefore does not have a noticeable effect on the temperature of the fuel, which relationship has also been assumed in previous SOFC models [76].

The energy balance for the fuel is represented by the equation:

$$0 = \left[h_{F,i}\frac{3}{4}(2\pi r_3 \Delta z)\left(T_{PEN,i} - T_{F,i}\right) + h_{F,i}\,\frac{1}{4}2\pi r_3 \Delta z\left(T_{ICF,i} - T_{F,i}\right) + h_{F,i}(2\pi r_2 \Delta z)\left(T_{FDT,i} - T_{F,i}\right)\right]_{conv} + \left[r_{me}\left(\Delta h_{C_2H_2}\left(T_{PEN,i}\right) + \Delta h_{H_2}\left(T_{PEN,i}\right) - \Delta h_{CH_4}\left(T_{F,i}\right)\right) + r_{eb}\left(\Delta h_{C_6H_6}\left(T_{PEN,i}\right) + 3\Delta h_{H_2}\left(T_{PEN,i}\right) - 3\Delta h_{C_2H_4}\left(T_{F,i}\right)\right) + r_{bt}\left(\Delta h_{C_7H_8}\left(T_{PEN,i}\right) + \Delta h_{H_2}\left(T_{PEN,i}\right) - \Delta h_{CH_4}\left(T_{F,i}\right) - \Delta h_{C_6H_6}\left(T_{F,i}\right)\right) + r_{po}\left(\Delta h_{CO}\left(T_{PEN,i}\right) + 2\Delta h_{H_2}\left(T_{PEN,i}\right) - \Delta h_{CH_4}\left(T_{F,i}\right)\right) + r_{sr}\left(\Delta h_{CO}\left(T_{PEN,i}\right) + 3\Delta h_{H_2}\left(T_{PEN,i}\right) - \Delta h_{CH_4}\left(T_{F,i}\right) - \Delta h_{H_2O}\left(T_{F,i}\right)\right) + r_{wgs}\left(\Delta h_{CO_2}\left(T_{PEN,i}\right) + \Delta h_{H_2}\left(T_{PEN,i}\right) - \Delta h_{H_2O}\left(T_{F,i}\right) - \Delta h_{CO}\left(T_{F,i}\right)\right) - r_{orr}\Delta h_{H_2}\left(T_F\right)\Big]_{rxn\ enthalpy} + \left[N_{F,i-1}\Delta h_{F,i-1}\left(T_F\right) - \mathrm{N_{F,i}}\Delta h_{F,i}\left(T_F\right)\right]_{Energy\ In - Energ\quad Out} \tag{3.49}$$

where h_F is the convective heat transfer coefficient for the reacting fuel at discretized point i, r_2 and r_3 are the radii of layers 2 and 3 from Figure 3.10, respectively, $\Delta h_s(T)$ is the enthalpy of species s at the corresponding temperature T, and N_i is the number of moles at the discretized point i.

The air side is similar to the fuel side, albeit with fewer reactions taking place. The energy balance used in this study models the convective heat transfer from the PEN structure and the interconnect, the reaction enthalpies, and the heat in/out along the discretized units:

$$0 = \left[h_{A,i} * \frac{3A}{4} * \left(T_{PEN,i} - T_{A,i}\right) + h_{A,i} * \frac{A}{4} * \left(T_{IC,i} - T_{A,i}\right)\right]_{conv} +$$

$$\left[r_{orr}\left(h_{H_2O}(T_{PEN,i}) - 0.5\Delta h_{O_2}(T_{A,i})\right) - 0.5 * r_{po}\Delta h_{O_2}(T_{A,i})\right]_{rxn\ enthalpy} +$$

$$\left[N_{A,i-1}\Delta h_{A,i-1}(T_A) - \mathrm{N_{A,i}}\Delta h_{A,i}(T_A)\right]_{Energy\ In-Energ\quad Out} \tag{3.50}$$

3.5.3 Constants for Solid Layers

The solid layers are relatively straightforward by comparison. The only input variables needed for these layers are the emissivity and thermal conductivity of the materials. Values for these terms are taken from the previous modelling work of Kazempoor [78], [85] and the online Engineering Toolbox as shown in Table 3.4:

Table 3.4: Thermal Conductivities of Solid Layers

Term	Units	Value	Reference
k_{PEN}	$\frac{W}{m*K}$	2.16	[77], [78], [85]
k_{IC}	$\frac{W}{m*K}$	27	[77], [78], [85]
k_{FDT}	$\frac{W}{m*K}$	355	Engineering Toolbox – Copper [95]
ϵ_{PEN}	-	0.8	[77]
ϵ_{FDT}	-	0.1	[77]

Convection and conduction are generally included in most fuel cell models, but radiation has been both considered and ignored in various modelling studies through the years [75]. Radiant heat transfer is governed by the area of the radiating surface, emissivity of the interacting surfaces, and the view factor between the radiating and absorbing surfaces, which quantifies the direct line-of-sight interaction necessary for radiative energy exchange. In planar SOFC models, Stiller et al. [96] and Recknagle [97] ignored radiant heat along channels due to a high length to width ratio in the cell minimizing its effect. High length

to width ratios have been proven to largely mitigate radiative heat in cell channels [98]. Other planar SOFC studies like Yakabe [98] and Xi [76] included heat radiation and their models returned a lower temperature variation through the cell as a result [75]. In all planar studies where radiant heat is considered, it always defined the relationship between the interconnect and the PEN assembly. This changes in tubular models, since the interconnect is often in direct contact with the PEN structure itself [84]. Ota et al. [99] provided a good example for radiant heat in tubular models, where the inner feed tube experienced radiant heat from the cathode in his model. A similar approach has been taken in this model, where the FDT and PEN assembly experiences radiation between each other.

3.5.4 Energy Balance in Solid Structures

The FDT, PEN assembly, and the interconnect are the three solid structures considered in this model. The FDT energy balance considers the convective heat transfer with respect to the pre-fuel and the reacting fuel, as well as the conductive heat transfer along its discretized units and radiation form the PEN assembly. The energy balance for the FDT is given by:

$$0 = \left[h_{F,i} * (2\pi r_2 \Delta z)\left(T_{F,i} - T_{FDT,i}\right) + h_{PF} * (2\pi r_1 \Delta z)\left(T_{PF,i} - T_{FDT}\right)\right]_{conv} +$$

$$\left[k_{FDT}\pi(r_2^2 - r_1^2) * \frac{\left(T_{FDT,i-1} - 2T_{FDT,i} + T_{FDTi+1}\right)}{\Delta z}\right]_{cond} + \left[\frac{2\pi r_3 \Delta z \sigma\left(T_{PEN,i}^4 - T_{FDT,i}^4\right)}{1/\epsilon_I + 1/\epsilon_{PEN} - 1}\right]_{rad} \quad (3.50)$$

For the PEN assembly, the cathode, anode, and electrolyte are considered together as one unit rather than 3 separate blocks. Most of the material properties for the PEN assembly can come from the anode, as the anode makes up the vast majority of the total block. The energy balance for the PEN considered the convective heat transfer to the air and

fuel bulk flows, the conductive heat transfer in and out of its discretized units, the reaction enthalpies, the electrical work required to generate power, the radiation from the FDT, and the conduction from the interconnects. The equation for energy and heat balance is shown below:

$$0 = \left[\frac{3}{4}\left(h_{F,i}2\pi r_3\Delta z\left(T_{F,i} - T_{PEN,i}\right) + h_{A,i}2\pi r_6\Delta z\left(T_{A,i} - T_{PEN,i}\right)\right)\right]_{fuel\backslash air\ conv.} +$$

$$\left[k_{PEN} * \pi(r_6^2 - r_3^2) * \frac{T_{PEN,i-1} - 2T_{PEN,i} + T_{PEN,i+1}}{\Delta z}\right] + \left[r_{me}\left(\Delta h_{CH_4}\left(T_{F,i}\right) - \Delta h_{C_2H_2}\left(T_{PEN,i}\right) -\right.\right.$$

$$\left.\left.\Delta h_{H_2}\left(T_{PEN,i}\right)\right) + r_{eb}\left(3\Delta h_{C_2H_4}\left(T_{F,i}\right) - \Delta h_{C_6H_6}\left(T_{PEN,i}\right) - 3\Delta h_{H_2}\left(T_{PEN,i}\right)\right) + r_{bt}\left(\Delta h_{CH_4}\left(T_{F,i}\right) +\right.$$

$$\left.\Delta h_{C_6H_6}\left(T_{F,i}\right) - \Delta h_{C_7H_8}\left(T_{PEN,i}\right) - \Delta h_{H_2}\left(T_{PEN,i}\right)\right) + r_{co}\left(\Delta h_{CH_4}\left(T_{F,i}\right) + 0.5\Delta h_{O_2}\left(T_{A,i}\right) -\right.$$

$$\left.\Delta h_{CO}\left(T_{PEN,i}\right) - 2\Delta h_{H_2}\left(T_{PEN,i}\right)\right) + r_{sr}\left(\Delta h_{CH_4}\left(T_{F,i}\right) + \Delta h_{H_2O}\left(T_{F,i}\right) - \Delta h_{CO}\left(T_{PEN,i}\right) -\right.$$

$$\left.3\Delta h_{H_2}\left(T_{PEN,i}\right)\right) + r_{wgs}\left(\Delta h_{H_2O}\left(T_{F,i}\right) + \Delta h_{CO}\left(T_{F,i}\right) - \Delta h_{CO_2}\left(T_{PEN,i}\right) - \Delta h_{H_2}\left(T_{PEN,i}\right)\right) +$$

$$r_{orr}\left(\Delta h_{H_2}\left(T_F\right) + 0.5\Delta h_{O_2}\left(T_{A,i}\right) - h_{H_2O}\left(T_{PEN,i}\right)\right)\Big]_{rxn\ enthalpy} + \left[-i_{cell,i}V_{cell}\right]_{elec.\ work} +$$

$$\left[\frac{2\pi r_3\Delta z\sigma\left(T_{FDT,i}^4 - T_{PEN,i}^4\right)}{1/\epsilon_{FDT} + 1/\epsilon_{PEN} - 1}\right]_{FDT\ rad.} + \left[k_{PEN}\frac{2\pi r_3\Delta z}{4}\frac{\left(T_{ICF,i} - T_{PEN,i}\right)}{r_6 - r_3}\right]_{ICF\ cond} +$$

$$\left[k_{PEN}\frac{2\pi r_6\Delta z}{4}\frac{\left(T_{ICA,i} - T_{PEN,i}\right)}{r_6 - r_3}\right]_{ICA\ cond} \tag{3.51}$$

The interconnectors do not have a location in the discretized model, but they are still modeled and included in this analysis. The interconnect temperature may vary differently than the PEN assembly, particularly due to the effect of Joule heating, which is a form of heat generation due to the ohmic resistance in an electrical circuit. As such, the energy released by this conduction is split between the air and fuel side interconnects and added to the traditional terms of conductive and convective heat transfer. Additionally, the interconnects

are assumed to cover approximately one fourth of the total surface of the electrodes. For the purposes of convection, the surface area available for heat transfer is estimated to be equal with what is available for conduction from the PEN assembly. The fuel-side interconnector energy balance is therefore represented by:

$$0 = \left[\frac{k_{IC}A_{IC}}{\Delta z}\left(T_{ICF,i-1} - 2T_{ICF,i} + T_{ICF,i+1}\right)\right]_{QinQout} + \left[k_{PEN}\left(\frac{2\pi r_3 \Delta z}{4}\right)\left(T_{PEN,i} - T_{ICF,i}\right)\right]_{cond} + \left[h_{F,i}\left(\frac{2\pi r_3 \Delta z}{4}\right)\left(T_{F,i} - T_{ICF,i}\right)\right]_{conv} + \left[\frac{i_{cell}^2 R_{ohm,IC}}{2\Delta z}\right]_{Joule\ heating} \quad (3.52)$$

Where $R_{ohm,IC}$ is the ohmic resistance due to the interconnect. Similarly, the air-side interconnect is represented by:

$$0 = \left[\frac{k_{IC}A_{IC}}{\Delta z}\left(T_{ICA,i-1} - 2T_{ICA,i} + T_{ICA,i+1}\right)\right]_{QinQout} + \left[k_{IC}\left(\frac{2\pi r_6 \Delta z}{4}\right)\left(T_{PEN,i} - T_{ICA,i}\right)\right]_{cond} + \left[h_{A,i}\left(\frac{2\pi r_6 \Delta z}{4}\right)\left(T_{A,i} - T_{ICA,i}\right)\right]_{conv} + \left[\frac{i_{cell}^2 R_{ohm,IC}}{2\Delta z}\right]_{Joule\ heating} \quad (3.53)$$

Chapter 4: Model Validation and Results

4.1 Model Validation

The proposed system in this study is a novel system with innovative characteristics. However, the novelty of the system and its intended purpose means that there are no direct experiments with which to validate the results discussed later in this chapter. Instead, hydrogen-fueled PCFC studies, known properties of fuel cells, mass balance, and experimental reaction data from a fixed bed reactor are combined to prove the validity of the model's results.

4.1.1 Mass Balance Validation

The principle of the mass balance in this model at a system level is that all mass input must equal the mass output. This condition must be verified for all the discretized units as plug flow assumption is considered for the PCFC model. Each discretized unit for the mass balance considered a full cross section of the cell to account for the generation and consumption of hydrogen as it travels from the fuel to air sides. Verifying at each discretized point is essential to ensure that the reaction conversions are properly integrated in the model. This study takes a simplified approach and only considers nitrogen, carbon, hydrogen, and oxygen in the flow streams. Other components and impurities that are common in natural gas like sulfur are omitted for simplicity here, leaving the door open for

their inclusion in future modeling studies. However, it should be noted that certain components should generally be used to reduce sulfur contents of the inlet gas as it can impact the catalyst's durability. The adherence to the mass balance principle is verified by the following equation for each considered element – oxygen, hydrogen and carbon:

$$\sum_1^n \nu_\varphi N_{s,i-1} = \epsilon_\varphi + \sum_1^n \nu_\varphi N_{s,i}\,,\ \varphi \in \{C, H, O\}$$

$$s \in \{CH_4, H_2, C_2H_4, C_6H_6, C_7H_8, H_2O, O_2, N_2\} \tag{4.1}$$

where n is the number of species in the system bearing carbon, hydrogen, or oxygen; the subscript φ signifies carbon, hydrogen or oxygen; s identifies the species; ν denotes the stoichiometric coefficient reflecting the number of carbon, hydrogen, or oxygen atoms in each species; and ϵ is a discrepancy term that always equals zero when the mass balance is accurately maintained in each discretized unit i.

In the iterative solutions provided by EES, the discrepancy term typically equaled something on the order of 10^{-25}. Since the lowest number of moles of any species in the system is closer to 10^{-10}, the mass balance is effectively confirmed across the length of the cell.

4.1.2 Reaction Kinetics Validation

As has been discussed in sections 2.2 and 3.2, the kinetic model utilized by Jeong [64] has been adopted and modified here. However, the catalyst considered for the application at flaring sites, as suggested in Chapter 1, is adapted from the work of Zhu et al.[65]. To get an accurate idea of the reaction rates for the PCFC, a fixed bed reactor (FBR) model is used. This FBR model has the same geometry as Zhu et al. [65], which is a 7mm

inner diameter and a length of 450 mm. For the reactions, the FBR model has an identical formulation to the PCFC model, but the electrochemical sub-model is removed to eliminate the removal of hydrogen that necessarily takes place in the PCFC. This allowed the kinetics from Jeong's [64] work, which is also an FBR with similar geometry, to be adjusted until the outputs matched the work of Zhu et al. [65].

Zhu's study used a novel heterogeneous trimetallic synergistic catalyst for MDA that incorporates the same foundational Mo/ZSM-5 catalyst of Jeong's work, while adding platinum and bismuth for enhanced kinetics [65]. Due to the similarities of the catalysts in Jeong's and Zhu et al.'s studies, the activation energies are kept identical to Jeong's work and only the rate constants are adjusted so the outputs from the FBR model matched the experimental work of Zhu et al. [65]. After testing a variety of different catalyst compositions, the final version of the catalyst consistently achieved 16-20% methane conversion, and around 70% selectivity for benzene, with the remaining 30% being split among coke, C_2, and C_7 byproducts [65]. Therefore, these are set as the target values for the FBR model. It is assumed that the majority of the C_2 products are ethylene, so that is the only C_2 product considered, as shown in Figure 4.12.

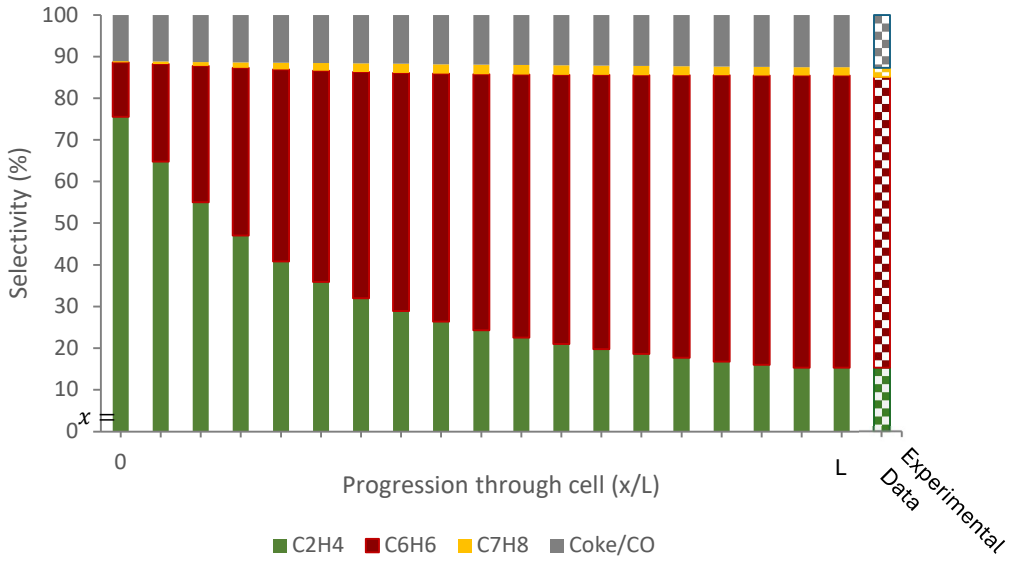

Figure 4.12: FBR model comparison to experimental data from [65]

Figure 4.12 shows the results of the model as the process flows through the reactor from the inlet ($x = 0$) to the outlet ($x = L$), compared to the experimental data which is dotted and shown on the right. These results are gathered running at the same operating temperature of 710 °C and space velocity of $1.272\ L \cdot {g_{cat}}^{-1} \cdot h^{-1}$ from Ding's experimental work. While there is no visible difference in the outputs on the graph, the error in the points is approximately ~0.2% for the selectivity of benzene, toluene and coke, and ~.2% for ethylene, which are respectively considered negligible. The total methane conversion at the outlet is 18%, which is a reasonable estimate from Ding's work for a steady state model. These results confirm the validity of the kinetics implemented in the FBR model.

4.1.3 Electrochemical Validation

The approaches and constants used for the electrochemical sub-model are initially gathered from other validated fuel cell modeling studies, with PCFC studies used for constant data wherever possible [33], [77], [88], [89], [90], [91]. However, many of these

estimates from other works required adjustments for this model to align with validation data due to advancements in PCFC fabrication and operational variances. For example, other studies can be compared to the data generated in this model, but discrepancies can be expected primarily due to the high concentration of methane/natural gas that is anticipated for this model. When methane or natural gas is used as the fuel for the cell, it has historically been mixed with additional hydrogen or water at a ratio of 60-70 vol% water at the inlet [12]. This practice is not adopted here since such compositions are not expected from flare gas streams, and such high levels of additional hydrogen would likely limit the conversion into aromatics [73]. Additionally, this assumption prioritizes the steam reforming and water gas shift reactions for the internal generation of hydrogen, which is a popular tactic for methane-fueled PCFCs, but also increases CO and CO_2 emissions. Because these reactions are mitigated in favor of the MDA reactions in this model for hydrogen generation, the electrochemical results for the model cannot be validated using experimental data from studies using methane as the fuel.

Instead, the electrochemical sub-model is validated using experimental hydrogen-fueled PCFC data from [33]. In this study, isothermal circular large button cells are used with a surface area of 0.5 cm^2 and a flow rate of 80 mL/min for the hydrogen cells [33]. Therefore, an isothermal model with the same geometric surface area, flowrates, and electrolyte and electrode thicknesses is created to validate the electrochemical sub-model. The values for resistance are taken from Duan's work, while activation and concentration losses are taken from an assortment of other works outlined in chapter 3 [88], [89], [90], [91]. An additional loss of .055 V from the total Nernst potential is necessary to add to the model to gain the fit

seen in Figure 4.13. This significant addition is attributed to leakage, variances in electrolyte thickness, and localized concentration losses not accounted for the in concentration overpotential since it is adapted from an older SOFC model.

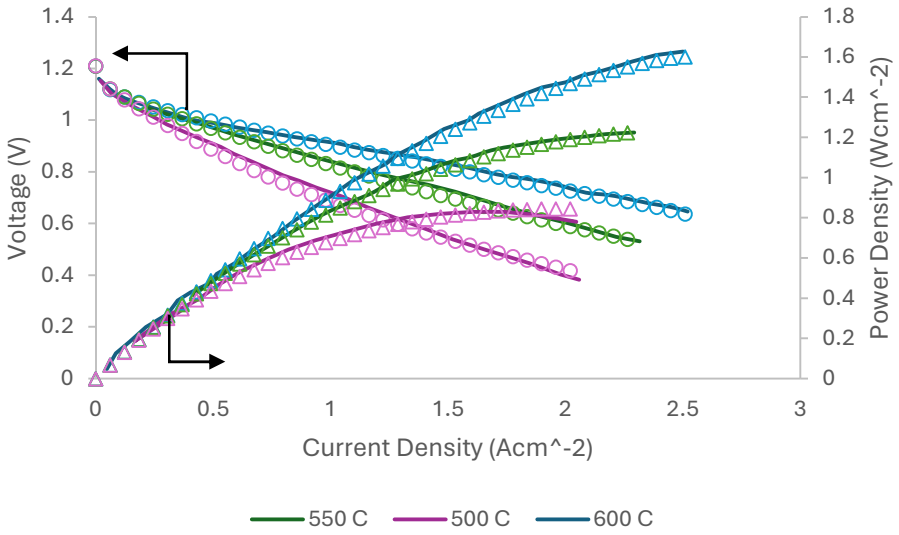

Figure 4.13: Electrochemical validation data using hydrogen

The experimental data spans from 275 °C through 600 °C. The anticipated operation is closer to 700 °C, thus the three highest temperatures of 500 °C, 550 °C, and 600 °C are used for the validation. Figure 4.13 shows that the model very accurately predicts the experimental outputs of voltage and power density with current density. The model accurately accounts for the variation with temperature from 500-600 °C. This implies that data taken at 700 °C should be an accurate representation of these materials at elevated temperatures. The same electrochemical sub-model from this validation model is used in the MDA model where methane/natural gas is used as the fuel. This should establish a quality estimate of the system's electrochemical capabilities until experiments can be carried out for further validation.

4.2 Model Results

The results from the model are approached with the intent to meet the states goals of 90% emissions reduction, 50% aromatic selectivity, and 30% fuel conversion. Achieving all 3 of these goals is challenging and may possibly be outside the limit of theoretical possibilities with this catalyst. This section presents a parametric analysis of the model to optimize the outputs from the flare gas system.

4.2.1 Model Parameters

The model is controlled by the following adjustable parameters:

Table 4.5: Model adjustable input parameters

	Parameter	Symbol	Units
Primary	Inlet Temperature	$T_{fuel\ in}$	$°C$
	Inlet Pressure	P_{in}	bar
	Flow rate	$\dot{V}$	$\frac{L}{g_{cat}h}$
		$\dot{m}$	$\frac{kg}{s}$
	Current density	j_{cell}	$\frac{A}{cm^2}$
	Inlet Composition	x_s , $s \in \{CH_4, H_2, H_2O, C_2H_4\}$	%
	Fuel Conversion	F_U	%
	Emissions	ε	%
Secondary	Anode Thickness	τ_{an}	mm
	Channel Height, fuel	$h_{ch,f}$	mm
	Steam Reforming Coefficient	α_{sr}	-

WGS Coefficient	α_{wgs}	-

In Table 4.5, there are seven primary and four secondary parameters. Of these, the model requires four of the primary parameters and all the secondary parameters to be defined in order to converge a solution. This leaves three primary parameters for the software to solve using the formulation discussed in Chapter 3. In subsequent sections, the relationship between the primary parameters is analyzed, as well as the effect of changing the secondary parameters on the outputs of the system.

The standard inlet temperature and pressure of the model is 710°C and 1.005 bar, respectively. The flow rate is often adjusted to achieve a specified fuel conversion ratio, but the baseline value used in this model is 1 $Lg_{cat}^{-1}h^{-1}$. The current density is varied and depends on the inlet composition. The inlet composition in this model consists of highly idealized natural gas (95% methane, 5% water), additional water, and optional recycling streams of hydrogen and ethylene. Since any recycled stream is a product of the natural gas, and additional water outside the 5% considered for the natural gas is considered an additive, the fuel utilization is based only on the consumption of the natural gas, i.e. the 95% methane and 5% water feed. This is the term that aligns with the research goal of >30% natural gas conversion. Lastly, the emissions term is the sum of the selectivity of the methane conversion to CO and CO_2, which proceed to the flare after the PCFC system. This term is ideally <10% to achieve a 90% reduction in emissions. The secondary parameters, along with other important model inputs are shown below in Table 4.6 unless otherwise indicated.

Table 4.6: Input parameters

Input	Value	Units
Faraday's constant	96485.4	$C\ mol^{-1}$
Universal Gas constant	8.314	$J\ mol^{-1}\ K^{-1}$
Stefan-Boltzmann constant	$5.67 \cdot 10^{-8}$	$W\ m^{-2}\ K^{-4}$
Cell length	0.125	m
Anode thickness	500	μm
Cathode thickness	20	μm
Electrolyte thickness	3.6	μm
FDT thickness	1	mm
FDT inner radius	1.5	mm
Channel height, fuel	1	mm
Channel height, air	1	mm
Steam reforming coefficient	0.3	-
WGS coefficient	0.4	-
PEN density	500	$kg\ m^{-3}$
PEN thermal conductivity	2.16	$W\ m^{-1}\ K^{-1}$
Interconnect thermal cond.	27	$W\ m^{-1}\ K^{-1}$
FDT thermal conductivity	355	$W\ m^{-1}\ K^{-1}$
FDT emissivity	0.1	-
PEN emissivity	0.3	-

In total, there are over 5400 individual equations calculated by the model as it solves 21 discretized units along the cell. Due to the complex reaction system in the model and the model's reliance on updating guess values and boundary conditions for these equations, this setup can be relatively constraining. For example, the model does not converge when the current density gets too close to zero or so high that all the hydrogen is depleted. This is due to the reaction system calling for changes to the adjustable primary parameters that exceed tolerance values at extreme current densities. However, this does not invalidate the

model's ability to accurately reflect outcomes for the vast majority of usable current densities.

4.2.2 Combining MDA and PCFCs

The great benefit that PCFCs can provide to MDA is the hydrogen removal. However, the hindrance for PCFCs is that MDA reactions cannot produce hydrogen as quickly as methane reforming reactions, which are more commonly utilized when methane is the primary feedstock in PCFCs. This is highlighted in the disparity in flowrates used by the validation models. In the reaction kinetics validation model, a space velocity of 1.272 $Lg_{cat}^{-1}h^{-1}$ is used to match the kinetic validation data [65], while 80 ml/min is used in the electrochemical model to match the electrochemical validation data [33]. Assuming an anode thickness of 0.5 mm, combined with the active area of 0.5 cm^2 [33], this results in a space velocity of over 350 $Lg_{cat}^{-1}h^{-1}$. This massive difference highlights the differing needs of MDA and PCFCs on their own. The high space velocity allows higher current densities to be employed, yielding higher peak power densities, while the low space velocity allows the MDA reaction to reach better completion. Therefore, when they are combined, the cell is forced into low flow rates and lower current densities, as shown in Figure 4.14

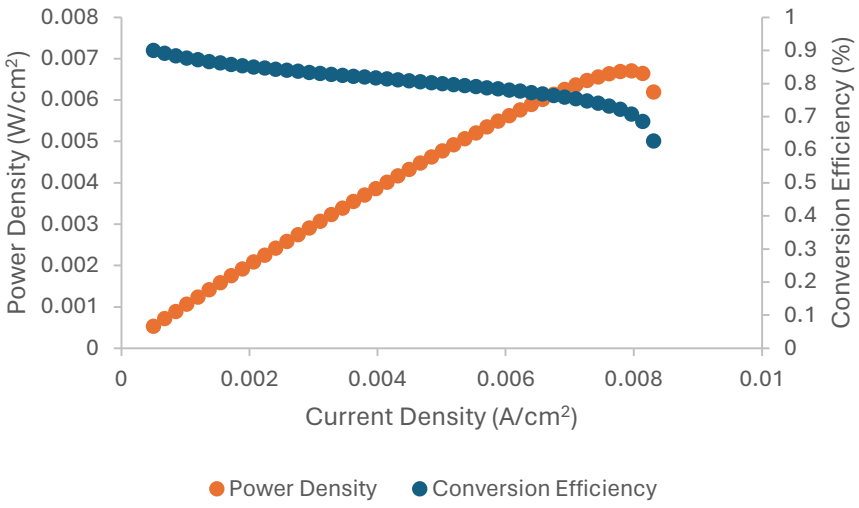

Figure 4.14: Current vs power density and conversion efficiency when operating at 1 $Lg_{cat}^{-1}h^{-1}$

The operational current density (and resulting power density) are significantly lower than the standard for PCFCs operating on methane, which can reach well beyond 1 Acm^{-2} when implemented with high levels of water for reforming [33]. The maximum power produced in the cell at the operating flowrate of 1 $Lg_{cat}^{-1}h^{-1}$ is around 0.2 W since the active area in the tubular cell is around 27.5 cm^2. The conversion efficiency is a measure of how well the cell produces power from the consumed fuel, and is represented by equation 4.2:

$$CE = \frac{I \cdot V}{H_{2\,consumed} \cdot \Delta H_{LHV,H_2}} \tag{4.2}$$

where CE is the conversion efficiency in %, I is the applied current, V is the output voltage, $H_{2\,consumed}$ is the amount of consumed hydrogen in the model, and $\Delta H_{LHV,H_2}$ is the lower heating value of hydrogen. The CE starts at 90% at near zero, hits 75% at .007 Acm^{-2}, and then drops at .0083 Acm^{-2} when the hydrogen availability is depleted.

As a result of Figure 4.14, the following critical points play a large role in the subsequent results of the model:

- MDA reactions produce hydrogen much more slowly than methane reforming reactions
- The 5% water concentration provides a significant amount of the initial hydrogen needed for the PCFC to operate
- Extremely low current densities may be necessary for MDA to proceed within a PCFC
- 0.007 Acm^{-2} provides a safe and effective balance of hydrogen removal and CE

4.2.3 Achieving 30% Fuel Conversion

Per the goals outlined in chapter 1, achieving 30 % fuel conversion is the first goal considered here. Achieving a fuel conversion in excess of 30% is challenging, particularly because without hydrogen removal, conversion levels have been equilibrium limited. Therefore, to achieve 30% conversion, slow flow rates to allow for additional contact time are combined with hydrogen removal. This proves to have a noticeable effect on the selectivity of the aromatic products as shown in Figure 4.15, where the conversion is held constant at 30% across operational current densities:

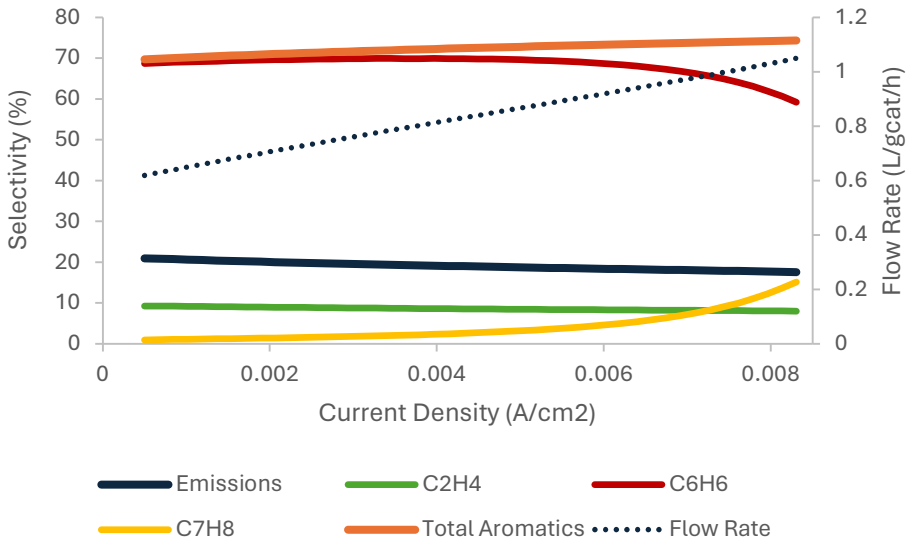

Figure 4.15: 30% natural gas conversion effect on flow rate and selectivity at rising current densities

In Figure 4.15, a strong proportional relationship is shown between the flow rate and the current density when maintaining a 30% conversion. Conversely, there is an inverse relationship of the selectivity of benzene with the current density. This relationship is primarily due to the increase in toluene yield. Toluene is more equilibrium-constrained by hydrogen than its benzene counterpart, leading to its more drastic increase in selectivity at greater levels of hydrogen removal. The total aromatic selectivity steadily increases with current density and achieves 74.4% at the highest current density. However, benzene is a more valuable product than toluene with double the market size, thus the cell should ideally be operated at temperatures where benzene is encouraged over toluene. A current density of 0.007 Acm^{-2} once again serves as a balance point as the benzene is still over 66% and the toluene selectivity is only at 7% compared to the maximum current density where it is over 15%.

A decline in emissions from 21% down to 17.6% is also seen in Figure 4.15. The emissions selectivity decreases for two reasons: 1) the reliance on hydrogen removal for steam reforming and water gas shift reactions is much less than that of MDA reactions, and 2) despite the α_{sr} and α_{wgs} arbitrarily reducing the effectiveness of their reactions by 70 and 60% respectively, they completely exhaust the water very early on in the cell, as shown in Figure 4.16. This means that as aromatic reactions continue to improve with hydrogen removal, the methane reforming reactions are directly controlled and limited by the amount of water in the feed stream.

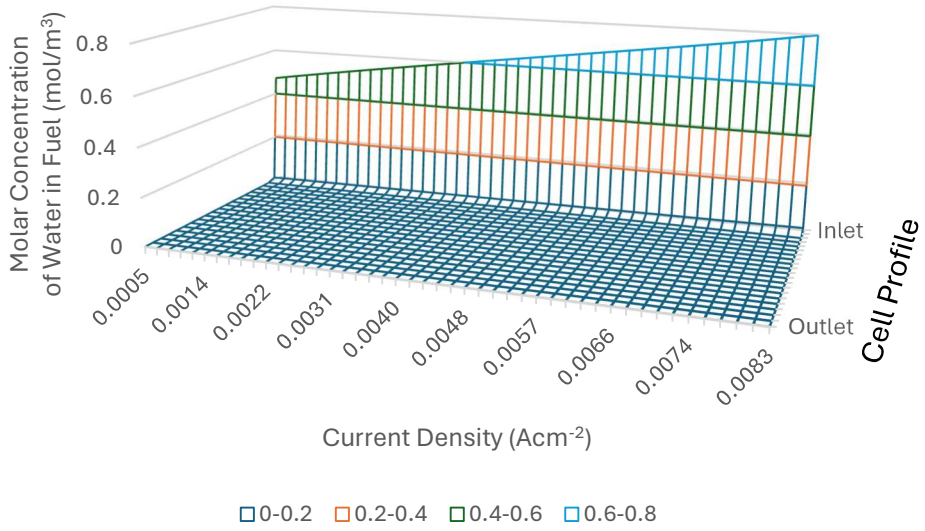

Figure 4.16: Moles of water in the fuel from the inlet to the outlet of the cell at all operational current densities for 30% fuel conversion.

In Figure 4.16, the sharp drop highlights the exponentially faster kinetics of methane reforming and water gas shift over the MDA reactions. The increased inlet concentration at higher current densities is representative of the effect of hydrogen removal giving slight priority to MDA reactions at the inlet. Regardless, the water in the fuel is effectively depleted by the second discretized element of the cell regardless of hydrogen removal.

The temperature is also considered as a prominent variable for achieving 30% conversion. When using the balanced current density of .007 A/cm^{-2}, 30% conversion is achievable at all attempted temperatures between 697 - 800 ℃. Any lower temperature failed to converge as the slow MDA reaction kinetics limit the fuel conversion as they get slower with decreasing temperature, underscoring the importance of achieving 700 ℃ in MDA reactions. However, lower temperatures are desirable for the durability of the cell, thus another attempt is made using 0.004 Acm^{-2} and is shown in Figure 4.17.

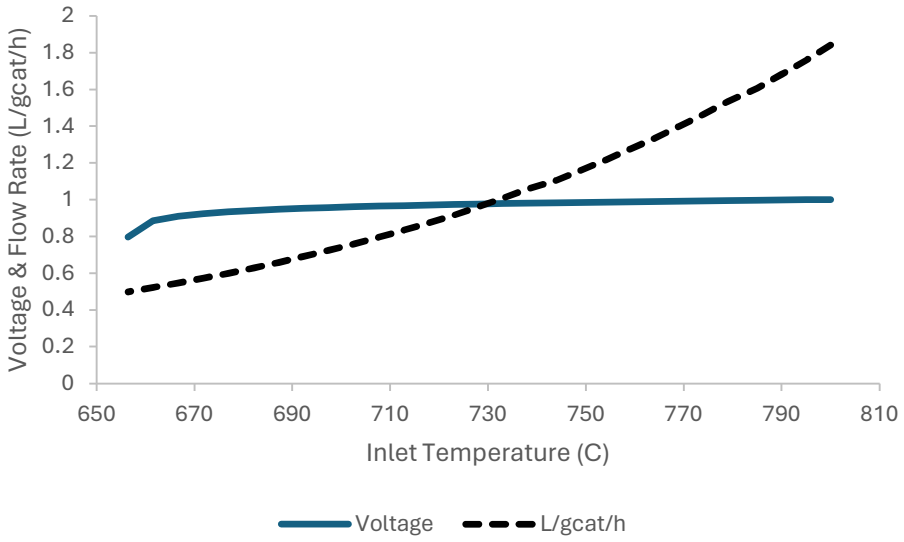

Figure 4.17: Relationship of the inlet temperature and flow rate at 30% conversion using a current density of 0.004 Acm^{-2}

In Figure 4.17, the inlet temperature is gradually dropped from 800 ℃ until it failed to converge due to limited hydrogen availability as the MDA reactions slowed with decreasing temperature. The lowest achievable temperature is 656 ℃, noticeably lower than the lowest temperature using 0.007 Acm^{-2}. Figure 4.17 also indicates that continuing to decrease the flow rate should allow for continued decreasing inlet temperatures for the cell while still achieving 30% fuel conversion. However, the sudden drop in voltage the cell experiences at

the lowest temperature indicates a lack of hydrogen availability. As the temperature continues to drop, the MDA reactions are less favorable, but the methane reforming reactions continue to be strong. So, while continuing to decrease both the flow rate and the current density may enable even lower temperatures for 30% conversion, this trend reaches a hydrogen-availability and kinetic threshold that will render the MDA PCFC ineffective. Therefore, it is estimated that 650 ℃ is the lowest temperature that has the potential to achieve reasonably effective results alongside a 30% fuel conversion, barring further catalyst development.

If the PCFC system is run with the intent to achieve conversion rates other than 30% fuel conversion, it is important to understand the consequences. As such, the maximum and minimum conversions attainable at 0.007 Acm^{-2} are shown in Figure 4.18. Like Figure 4.17, the model is run until a solution could no longer be converged in either direction, reaching limits of 4% fuel utilization and up to 56% fuel utilization at 0.007 Acm^{-2} at an inlet temperature of 710℃.

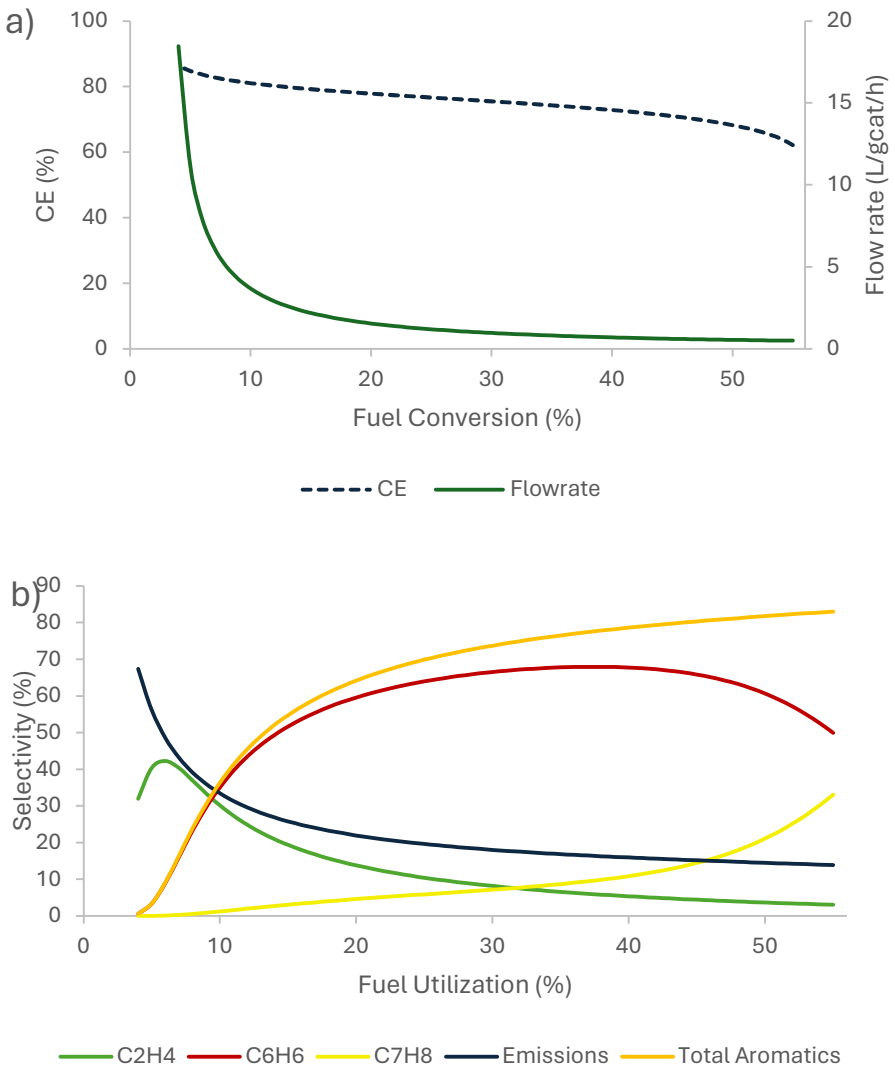

Figure 4.18: Effect and limitations of varying the fuel utilization; a) the inverse relationships of CE and flow rate with fuel conversion; b) fuel conversion's effect on the output selectivity

The first note from Figure 4.18a is that the CE, and therefore the voltage and power density, are only lightly dependent on the fuel utilization, with the CE gradually decreasing from 86-62% with increased fuel utilization. Because the CE varies exactly with the voltage, this implies that the power output from the cell is consistent through minor to moderate fluctuations of the flow rate through it, which could be especially helpful when relying on the power output from the cell at a place like a wellhead flare where the flare gas flowrate has

the potential to experience many fluctuations. Conversely, the flowrate has an exponentially inverse relationship with fuel utilization, reaching as high as 18.4 $L/g_{cat}/h$ at 4% utilization and as low as .50 $L/g_{cat}/h$ at 56% utilization.

In the selectivity graph in Figure 4.18b, dependencies on the fuel utilization are the most pronounced for the benzene and emissions selectivity but are clearly apparent for all products. Benzene is essentially not produced at extremely low fuel utilization, but achieves a maximum of 65%-68% selectivity between 26%-46% fuel utilization before lowering back down to 50% at maximum fuel utilization due to the accelerated production of toluene. The apparent lack of benzene at low fuel utilization is due to the high flow rate preventing opportunities for the newly formed ethylene to interact on the catalyst reaction sites. This is reversed at low flow rates, where ethylene has the maximum opportunity to react. Notably, the benzene selectivity sharply increases to 60% at only 20% fuel utilization and increases only gradually thereafter. Additionally, the total aromatic selectivity achieves the goal of 50% selectivity at only 13% conversion.

Ethylene is the important intermediate product and has an initial spike up to 42.3% selectivity at 6% utilization and then decreases rapidly down to 3.1% at 56% fuel conversion. After the initial spike in selectivity, the decline in ethylene selectivity slows noticeably after 15-25% fuel conversion. Ethylene at the outlet is most certainly a byproduct and is ideally either mitigated or recycled to the inlet, which is discussed later.

The emissions rate is also strongly affected by fuel utilization. The relationship of the emissions is inversed with benzene selectivity, with a high of 67.4% selectivity at 4% fuel

conversion and then decreasing to 20% selectivity at 25% conversion before reaching a low of 13.9% selectivity at maximum fuel utilization, which is only 1.3% above the FBR results.

Lastly, the toluene varies with the utilization but also consistently remains at a very low selectivity until sufficient levels of hydrogen are removed. It achieves a high of 33.1% selectivity at 55% fuel conversion, but only gets above 10% selectivity at 39% fuel conversion (0.725 $Lg_{cat}^{-1}h^{-1}$). This underscores the exponential relationship between toluene production and hydrogen removal. It is likely that, in industrial practices, the very low flow rates required to achieve such high fuel utilizations may prevent toluene from becoming an abundant product from the system. While not as useful as benzene, toluene remains a valuable aromatic byproduct from the PCFC system.

The results from the figures 4.4-4.7 indicate the following important takeaways:

- Achieving the goal of 50% aromatic conversion should not be a significant obstacle
- Achieving 90% emissions reduction at usable current densities relies completely on catalyst development to speed up the MDA reaction mechanism so less water can be used in the natural gas stream. Currently, a small amount of water is required for the hydrogen production necessary to start the electrochemical reactions, which creates a lower threshold of emissions above the 10% DOE goal.
- A current density of 0.007 Acm^{-2} provides an effective balance between power output and product selectivity at 30% conversion, unless temperatures lower than 700 ℃ are required.

- While 30% conversion is most definitely an ideal goal and achieves high selectivity, a lower conversion may still be acceptable if there are too few cells to meet the flow demand. For example, a fuel conversion of 20% yields a 50% flow rate increase at the expense of only a 10% decrease in aromatic selectivity (down to 64%)
- 650℃ is the minimum inlet temperature required to achieve 30% conversion while also producing significant power levels. However, this requires extremely low flow rates.
- Toluene has the potential to spike at flow rates lower than 0.725 $Lg_{cat}^{-1}h^{-1}$.

4.2.3 Parametric Study of Input Parameters

The values in Table 4.6 are representative of ideal future applications and are loosely based on previous PCFC works directly applicable to this study [21], [33]. However, as real experimental data begins to be gathered, it is necessary to investigate several additional parameters more directly applicable to the fabrication and catalyst development. In this section, a flowrate of 1 $Lg_{cat}^{-1}h^{-1}$ is used instead of a demanded 30% conversion.

The first of these is the temperature profile. This has already been discussed some, but only from the perspective of the PEN assembly, which dictates the kinetics of the reactions. However, the PEN experiences heat transfer and is affected by other components as shown in Figure 4.19:

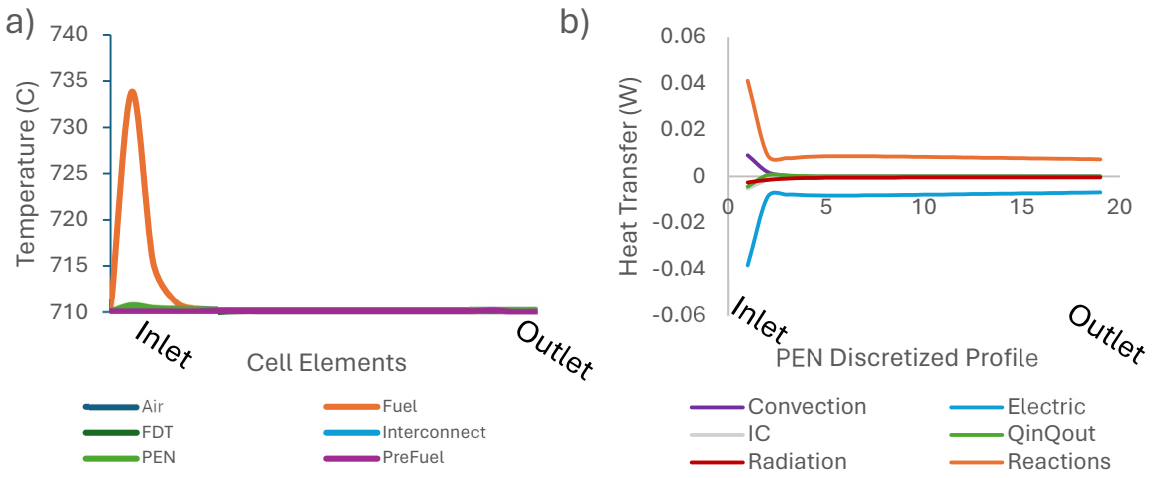

Figure 4.19: Temperature of cell components and heat transfer to the PEN assembly when operating at 710℃, 0.007 Acm^{-2}, and 1 $Lg_{cat}^{-1}h^{-1}$; a) Temperature profile along the z-axis of the various cell components; b) the heat transfer profile along the z-axis of the other components into the PEN assembly

In the model, the interconnect for the air and fuel sides are modeled separately and have their own temperatures, but their results are identical and so only the fuel side is shown in Figure 4.19a. Nearly all of the temperatures of the different components of the cell remain at the inlet temperature during operation, except for the reacting fuel which spikes near the inlet and quickly returns to the inlet temperature. The spike in the reacting fuel temperature can be attributed to the kinetically fast exothermic water gas shift reaction. This is confirmed in Figure 4.19b where the reactions produce a spike of heat at the inlet during the water consumption. Furthermore, only the heat from the reactions and the electrical work have a significant effect on the remarkably consistent temperature of the PEN through the cell. *All* the other heat inputs into the PEN assembly work out to values between ± 0.0005 W after the first two elements, which are considered negligible in comparison to the former. This phenomenon is explained by the flow rates in two ways. First, the slow nature of the MDA reactions limits their ability to provide a large temperature swing. This is also true for

electrochemical reactions. The water formation is very exothermic, but because it only occurs as a function of the current, which is extremely low, the temperature variation is minimal. Second, the low flow rates in the model necessitate even lower velocities. This, in turn, demands lower Reynolds and Nusselt numbers, which yield a low convective heat transfer coefficient as described in equations 3.43-3.46. Therefore, it is expected that when flowrates are increased that these other factors should have greater prominence, as shown in Figure 4.20:

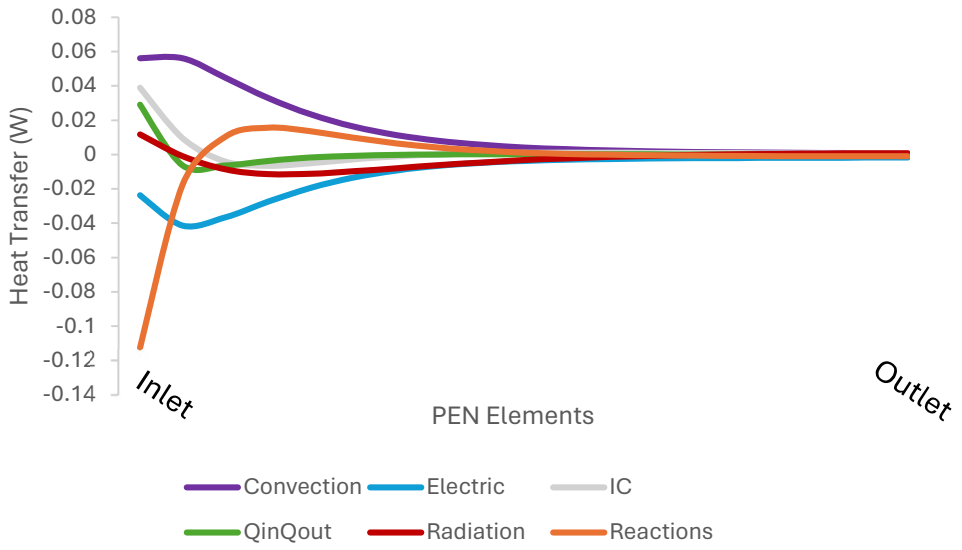

Figure 4.20: Heat transfer profile along z-axis of other components into the PEN at 25 $Lg_{cat}^{-1}h^{-1}$

In Figure 4.20, the initial variations in the temperature across its various components is caused by the reforming reactions. The increased heat transfer due to convection in the cell causes the whole cell to reach a uniform temperature despite the initial variation. The high value for electrical work at the inlet in Figure 4.19 and Figure 4.20 also means there is a higher current there. This higher current is only possible because of the reforming reactions; after these are completed, there is a correlating drop in current represented by the electrical

work in both Figure 4.19 and Figure 4.20. This is also reflected in the concentration overpotential shown below in Figure 4.21:

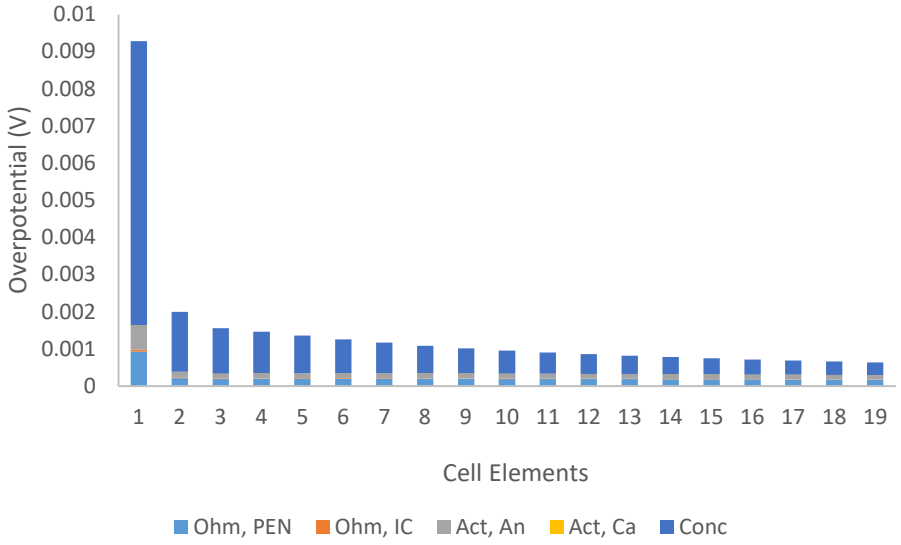

Figure 4.21: Overpotential profile through the cell, neglecting leakage

Figure 4.21 shows the effect of the different calculated overpotentials in the cell, with the concentration overpotential clearly represented as the dominant overpotential. The effect of the concentration overpotential compared to its activation and ohmic counterparts is much, much greater in this model than the validation model since hydrogen is not so readily available in the bulk flow. In other PCFCs where methane reforming reactions are the primary hydrogen source, all the primary reactions generate pure hydrogen with no significant amounts of hydrogen-containing byproducts. In this MDA PCFC model, a large portion of the hydrogen that would have been generated by reforming is instead forming the aromatic products. Therefore, even though the diffusion coefficients are taken from very effective PCFC studies [11], the concentration overpotential is more pronounced here due to hydrogen availability. Continued development of the anode catalyst with a focus on proton

conductivity can benefit the concentration overpotential to help close the gap between the bulk and triple phase boundary concentrations. In addition, while small in comparison to the concentration losses, the activation loss due to the anode far outweighs that of the cathode, further highlighting the benefits of continued anode catalyst development. However, the total voltage losses from the three represented overpotentials in Figure 4.21 are fairly miniscule compared to the voltage, which is close to 1 V. This tiny loss continues the trend seen in experimental studies that show decreased overpotential losses at lower current densities [33].

A variety of geometrical parameters are attempted to investigate their effect, but many of them do not yield significant differences. For example, the cell length could be increased, and it would linearly improve the power output but not the power density or the reaction kinetics. This is because the fuel inputs like fuel utilization and flowrate are directly linked to how much catalyst there is. So, increasing or decreasing the size or amount of catalyst also increases or decreases the flowrate in the model comparably.

However, the anode thickness plays a more significant role as it acts as the structural building block of the cell. Both Liu et al. [33] and Zou et al. [21] have recently used the anode as the structural surface on which printing/spraying techniques are used to apply the electrolyte and cathode layers. At the elevated temperatures that are needed for MDA, it is imperative that the anode be mechanically sound and able to withstand the thermal stresses. As such, it is not uncommon for the anode to vary significantly in thickness depending on the demands of the system. While this variance does not have a significant

effect on the reactions and kinetics, it does have implications for the overpotentials, as shown in Figure 4.22 below:

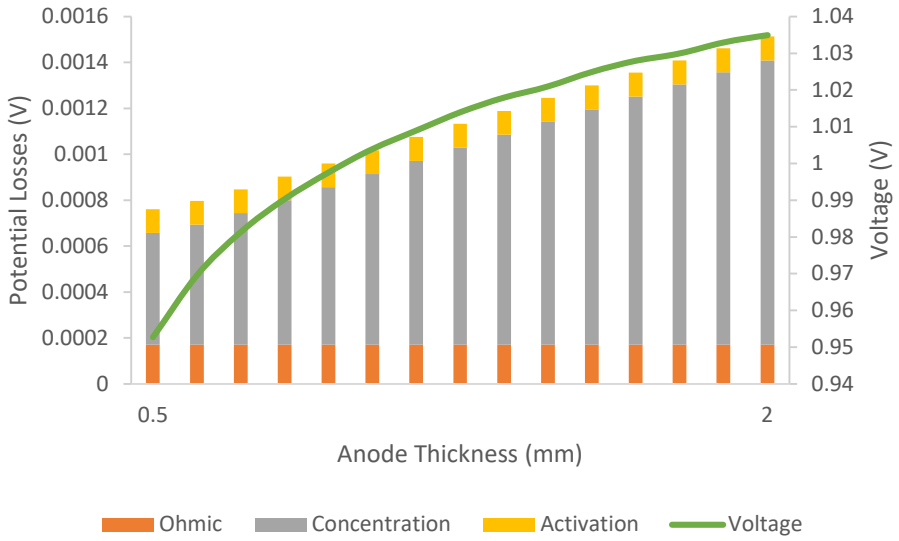

Figure 4.22: Effect of anode thickness on average overpotentials and voltage output of the PCFC

In Figure 4.22, the inlet temperature and flowrate are set to 710°C and 1L/g_{cat}/h, respectively. The left most data represents the voltage losses predicted by the PCFC and validation models and progresses to the right as the anode thickness is increased from 0.5mm up to 2mm. There is no measurable difference in the average ohmic loss since this is experimentally measured with respect to surface area, which did not change with anode thickness, and the activation overpotential is similar. The concentration overpotential is expected to have the largest difference in the model since increased thickness means more distance for the protons to be conducted. This extra distance can cause additional losses as it can be more difficult for the protons to make their way all the way through the PEN assembly. This overpotential is modeled in the calculation of the concentrations at the triple phase boundary in equations 3.34-3.37. The relationship of the losses with thickness is

strictly linear, and results in a concentration loss ~150% higher at a thickness of 2mm compared to 0.5mm.

Curiously, the output voltage *increases* nonlinearly with the anode thickness. Typically, the increased overpotentials would always decrease the voltage in a normal PCFC. In this case, the increased thickness translates into more catalyst, and therefore a higher flowrate when the space velocity is held constant. So, while this does not significantly change the selectivity of the products, it allows greater opportunity for the MDA reactions to occur and produce more water, as well as input more water at the inlet. The result is an increased Nernst potential due to increased hydrogen levels (see equation 3.23) that outweighs the increased overpotentials to yield a greater net voltage output. However, for a complete understanding of the relationship between anode thickness, catalyst effectiveness and voltage, additional modeling parameters like tortuosity and pore radius of the anode are required [88]. These factors help account for the additional length of travel required for diffusing ions through the porous medium and are likely to change the relationship between anode thickness and voltage shown in this model when implemented.

Other secondary parameters from Table 4.5 are varied but had little to no effect on outcomes. A more complex fluid mechanics model could be implemented wherein the fuel bulk flow is not considered a perfect mixture, and this would allow the change in height of the fuel channel to have a more pronounced effect than what this model can simulate. The α_{sr} and α_{wgs} have little effect due to the kinetics already being so much faster than the MDA reactions as has been previously discussed.

To revisit, the important takeaways from Figures 4.8-4.11 consist of the following:

- The electrical work and reaction heat are the largest sources of heat transfer for the PEN assembly at effective flowrates that yield aromatic outputs
- Due to low flowrates and current, the temperature of the cell components largely remains constant throughout the cell.
- The concentration overpotential is the overwhelmingly dominant overpotential in an MDA PCFC, but has little effect due to the low current density (equations 3.34-3.37)
- Anode thickness can be increased to yield greater voltage outputs due to the ability to increase the flowrate when catalyst volume is increased. However, this model lacks the necessary parameters to properly optimize the anode thickness for voltage output, so the maximum thickness used in subsequent sections is 1mm, as this has been used in recent experimental PCFC studies [21].

4.2.4 Recycling and Optimization

The final section in this chapter analyzes the possibility and benefits of recycling streams. Recycling streams allow the system to achieve higher conversions and benefit from the work it has already done. This comes at the expense of increased capital and construction costs but can pay off very well in the right scenario. These extra costs come from additional required elements in the system like separators, pumps, and sometimes amine scrubbing, as well as additional pipelines to reroute the process from a system outlet back to the inlet.

Hydrogen is a valuable byproduct that could increase the power output if put into a recycle stream. Ethylene is also considered. Ideally, the ethylene would all turn into benzene since benzene is more valuable and easily transportable. In a recycling system, this outcome becomes possible where it was not before. Data is gathered with this section with the flowrate held at 1 $Lg_{cat}^{-1}h^{-1}$ similar to previous sections, but the anode thickness is increased to 1mm. As such, higher current densities can be utilized due to the increased hydrogen availability as shown in Figure 4.23.

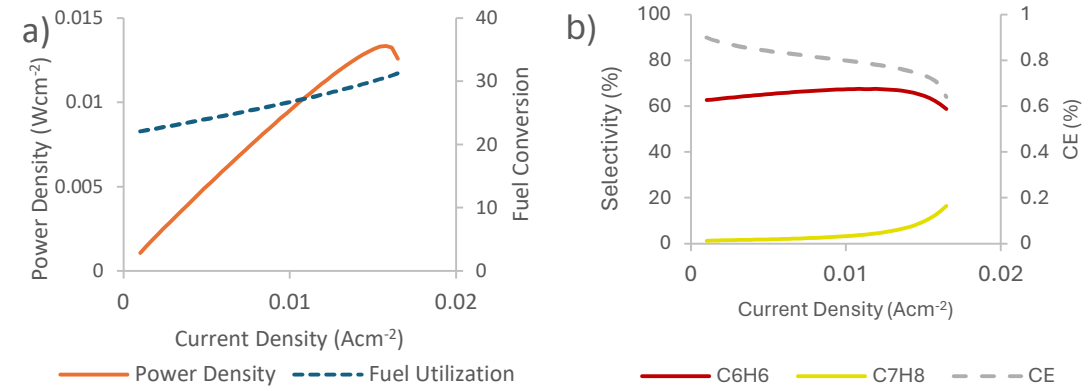

-

Figure 4.23: Updated power density (a) and selectivity (b) curves for an anode thickness of 1mm

A current density of .015 Acm^{-2} is selected as this is the minimum current that achieved 30% fuel conversion in Figure 4.23a. This also comes just before the heavy drop in CE and spike in toluene shown in Figure 4.23b. Without recycling or further optimization, the setup of 1 $Lg_{cat}^{-1}h^{-1}$ utilizing a current density of 0.015 Acm^{-2} at 710℃ achieves 0.0132 Wcm^{-2}, 74% CE, 30% fuel conversion, and 74% aromatic selectivity.

Before discussing recycling streams, the basic model is compared to the FBR model discussed in the validation study using Ding's experimental data [65]. The overall aromatic selectivity for the FBR is estimated around ~72%, with a coking/emissions selectivity of

12.6% at 1.272 $Lg_{cat}^{-1}h^{-1}$. For a fair comparison, the PCFC flowrate is temporarily increased to 1.272 $Lg_{cat}^{-1}h^{-1}$ and the main results are shown in Figure 4.24

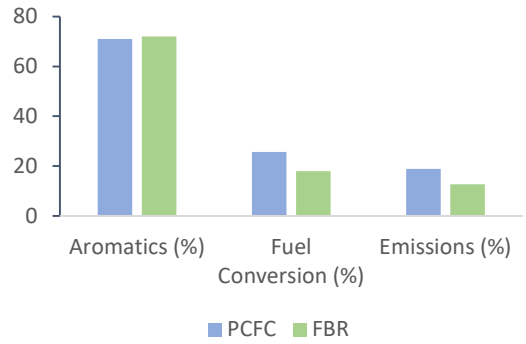

Figure 4.24: Basic PCFC model compared with FBR model used for validation

The FBR exhibits superior emissions results due to the lack of water but suffers from the need to regenerate the catalyst much more often than the PCFC model, which benefits from the oxygen ions conducting from the air side to remove the coke (see Figure 2.5 and Equation 3.9). Additionally, the PCFC model is achieving a higher fuel conversion of ~26% compared to the FBR's 18% at the same flowrate.

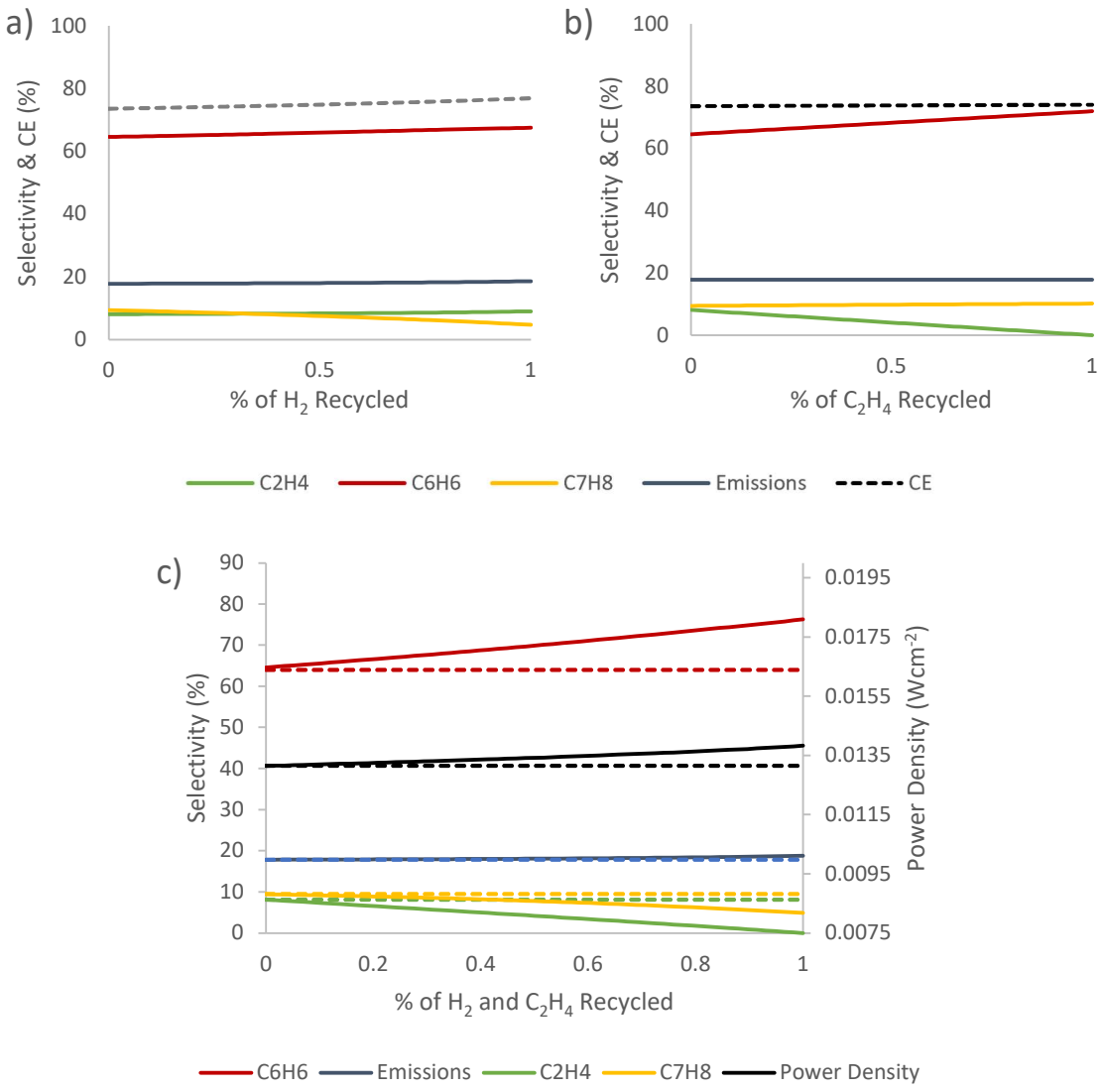

Figure 4.25: Effects of recycling only hydrogen (a) or ethylene (b) in the PCFC system on the carbon selectivity of the products leaving the system and the CE; (c) effect of fully recycling hydrogen and ethylene together with respect to zero recycling

In the individual recycling scenarios depicted in Figure 4.25a and 4.13b, the primary benefit of hydrogen recycling is an improved power production, while the ethylene recycling provides better MDA improvements. There are slight improvements in the CE of the cell in both scenarios, with the H2 recycle stream improving by 3.37% and the C2H4 recycle stream gaining just 0.47%. Both also saw improvements in the benzene selectivity, with the ethylene

recycling resulting in a 7.4% improvement while hydrogen recycling yielded just 2.9% improvement. Continuing toluene's relationship with hydrogen, recycling H2 proved to decrease the toluene output.

The best case scenario in both individual recycling scenarios in Figure 4.25a/b occur at a full recycling load and imply that hydrogen and ethylene recycling can be combined to synergize the results, as shown in Figure 4.25c. The fully recycled scenario effectively combines the electrochemical benefits of Figure 4.25a with the MDA benefits of Figure 4.25b, yielding an 11.7% increase in benzene yield with a 3.8% CE increase to achieve a power density of 0.0138 Wcm^{-2}. The significant increase in benzene is due to the complete removal of ethylene as a product and the reduction of toluene production from 9.4% to 4.8%. These trends are reiterated for a clearer comparison in Figure 4.26:

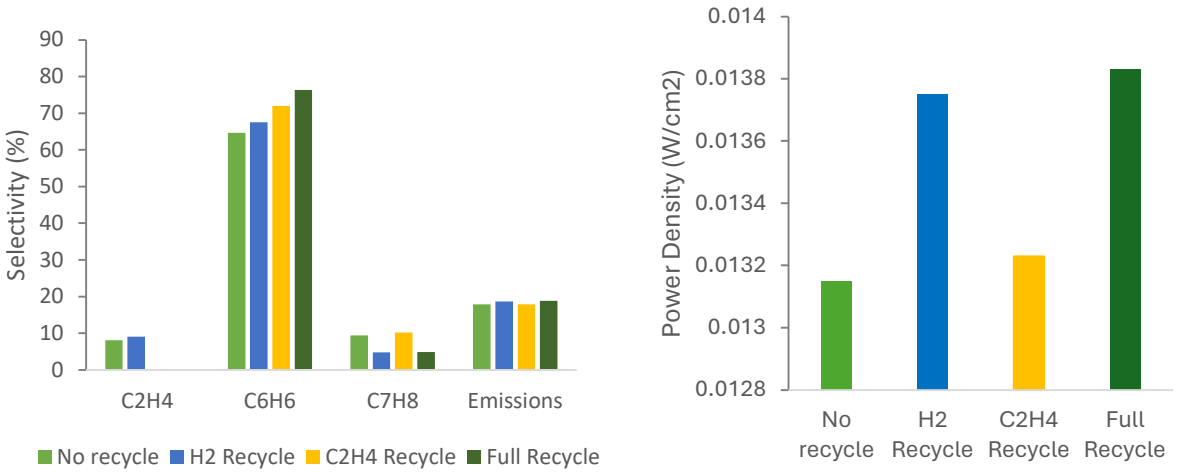

Figure 4.26: Comparison of the ideal recycling scenario with individual recycling and pre-recycle results

The synergized results of recycling both hydrogen and ethylene show notable improvements over the other recycling and the pre-recycling scenarios in all categories

except toluene output. However, the improvements in the benzene outweigh the toluene losses. Most notably, the improvements in selectivity and power are made with no significant change in emissions.

Final takeaways from the recycling models are as follows:

- If only hydrogen or ethylene could be recycled, ethylene takes priority since the aromatics improvement is more valuable than the power improvement
- The ideal recycling scenario with maximum benzene selectively and the ideal balance of improved power density and mitigation of emissions occurs when both ethylene and hydrogen can be fully recycled into the stream
    - Benzene selectivity increases by nearly 12% in ideal recycling conditions.
- Recycling streams cannot improve the emissions, since these are mostly determined by the water output
- The final results of the basic, non-recycling PCFC exhibit marked improvements in the fuel conversion over the FBR model. It is also anticipated that catalyst regeneration will be largely mitigated in the PCFC, which is significant as the FBR required regeneration every six hours [65], but this comes at the cost of increased emissions in the PCFC

Chapter 5: Evaluation and Comparison

The aim of this chapter is to ascertain the viability of implementing a cogenerating protonic ceramic modular reactor to utilize currently stranded/flared natural gas as shown in Figure 1.2, as well as compare it to existing technologies. This is accomplished by a comparison of the results from Chapter 4 with competing technologies like traditional power plants, gas to liquids (GTL) plants and Fischer-Tropsch Synthesis (FTS) facilities.

5.1 Methods

5.1.1 Evaluation Overview

Three pillars of analysis for industrial applications are thermodynamic (i.e. efficiencies), environmental, and economical [100]. As such, the suggested technology and its expected capabilities are compared with competing technologies with regard to these three foundational backgrounds, with a heavy emphasis on economic viability.

To ascertain whether the PCFC technology is competitive, the modeled status of the PCFC is compared to several commonly practiced techniques. These consist of GTL technology, FTS facilities, BTX plants, and power production technologies like natural gas power plants and alternative energy production methods. GTL is used as a case study and comparison throughout this document since the primary purpose of GTL processes is to

produce useful fuels, hydrocarbons, and chemicals from natural gas and related feedstocks. One of the most common and mature GTL technologies for methane conversion is FTS. FTS plants take a hydrogen and carbon monoxide mixture, referred to as syngas, and convert it into hydrocarbon products like naphtha, light gases, gasoline, diesel, and heavy waxes [100]. Because the specific desired product for the PCER system is aromatics, BTX plants serve as useful benchmarks for conversion and chemical production rates and are also used in the comparison study.

As this is the first attempt at a system-level integration cost analysis of a PCFC utilizing MDA, a model is constructed in Aspen-HYSYS to analyze the balance of plant costs and expectations of integrating a PCFC at a flaring site. Aspen-HYSYS is an incredibly useful process engineering software capable of easily modeling industrial applications, as well as presenting capital and operational cost estimations with its in-house economic analyzer tool. The economic analyzer within Aspen-HYSYS considers many factors including direct field costs, and both direct and indirect non-field costs. Direct field costs include factors such as equipment, piping, civil, instrumentation/controls, electrical equipment, insulation, and paint. Indirect field costs consider engineering, start-up, and construction expenses like scaffolding, rentals, and insurance. Indirect non-field costs include freight, contingencies, permits, taxes, and other project costs [101]. Overall, Aspen-HYSYS has the capability to provide a very effective benchmark prediction for new industrial system costs.

This Aspen-HYSYS model is used in tandem with the EES model to predict the impact of the PCFC system on the flare site. The data and background for the model is generated via a case study wherein the PCFC system is hypothetically implemented at a remote flaring site

in North Dakota's Bakken basin. The economic assessment performed here is relatively high-level, as a more detailed breakdown was not necessary to reach early conclusions about the necessary improvements.

5.1.2 Aspen-HYSYS Modeled Use Case

Data for the use case is gathered from public wellhead data and previous use case studies that have used a similar location as an example. In this study, the selected site flares an average of 209,000 scf/d of natural gas [102]. Initial gas conditions are taken from arbitrary values that meet the equipment conditions outlined in ISO 10423:2003, also titled API 6A: Specification for Wellhead and Christmas Tree Equipment [103]. In addition, the composition of the gas is selected from arbitrary values provided by the standard ranges given in Siazik and Malcho's work [104] and values provided in other natural gas processing models [105], [106]. The exact composition from the beginning to the end of the model is provided in Table 5.7. The result from this composition and average flare rate yields a mass flow rate of 177 kg/h through the EES and Aspen-HYSYS models.

Table 5.7: Inlet molar concentration for Aspen-HYSYS model

	Common values (mol %)	**Aspen-HYSYS Model (mol %)**
Methane	70-90	0.7926
Ethane	0-20	0.0411
Propane	0-20	0.003
CO2	0-8	0.0151
n-Butane	0-5	0.0203
Nitrogen	0-5	0.0099
i-Butane	0-5	0.0203

n-Pentane	0-5	0.0099
n-Hexane	0-5	0.0061
i-Pentane	0-5	0.0127
H2S	0-5	0.0000
Benzene	0	0.0000
Water	0-5	0.0419

The gas is assumed to be sweet, as reported wellhead data indicates that there are a number of wellheads that produce sweet gas naturally [107], or have the capability to process raw natural gas onsite [108]. If the wellhead produces sour gas, then the assumption is made that the gas will have already gone through a sweetening process prior to entering the modeled Aspen-HYSYS system shown in Figure 5.27.

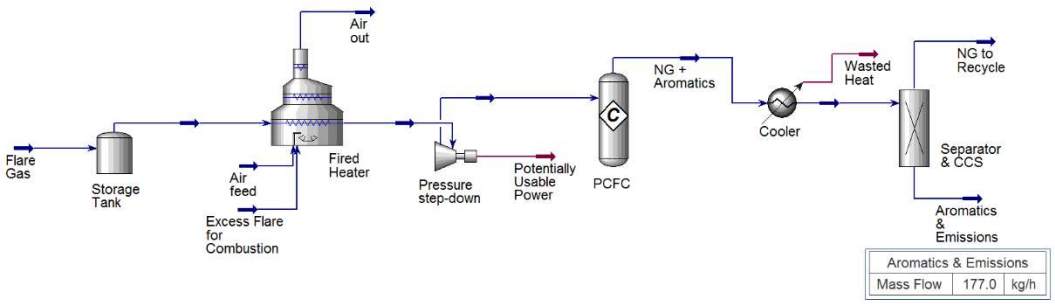

Figure 5.27: Aspen-HYSYS system integration model of protonic ceramic modular reactor

In Figure 5.27, the flare gas is first routed to a storage vessel, so the operation of the PCFC does not fluctuate with the same irregularity of a flare. Some flares are only operated for four hours per day [102], which would force extremely high flow rates through the PCFC and render it ineffective for aromatics production. This can be mitigated by the use of a storage vessel to extend the same flow of gas over a 24-hour period to ease the flowrate through the PCFC system. A small portion of the flare gas is then used in a fired heater to heat the gas to the PCFC inlet temperature. PCFCs cannot be accurately modeled with the

basic setup of Aspen-HYSYS. Instead, the relevant outcomes from chapter 4 can be modeled within the Aspen-HYSYS program by a conversion reactor with set conversion % rates. The product is then cooled for aromatics extraction and sent to a carbon capture system (CCS) and recycling flow. CCS's can be incredibly complex systems to model, so the simplified component splitter tool is used instead of building out a CCS sub-model. A component splitter in Aspen-HYSYS is a tool used to model the outcomes of an outside system, in this case the CCS and aromatics separation unit. The resulting mass flow of the aromatics and carbon species should match the average mass flow of gas that would have gone through the flare. Non-converted gas is recycled back to the inlet via the component splitter.

The end product coming out of the cooler is unconverted gas and aromatics, alongside nonaromatic MDA byproducts consisting mostly of carbon oxide emissions, ethane and ethylene [109]. The aromatics are easily filtered out in the cooling process as they achieve liquid conditions beginning at ~80℃ at atmospheric pressure, over 100°C higher than methane and other byproducts. Ethane and ethylene can continue to be reformed in the PCFC to generate aromatics and therefore should not be separated from the main gas feed stream [15], [110]. At this point in, the stream labeled "NG to recycle" would return to the "Raw NG" stream to repeat the cycle.

5.1.3 Costing Approach

To evaluate the profits of the system, an estimate for the price of the two primary products of the system is considered, namely, the price of electricity for the plant, and the sale price of aromatic chemicals. The average ultimate price for electricity in the U.S. is

around 12 cents per kWh [111], and this number is used here even though it is substantially higher than the industrial average due to the elevated cost of electricity in remote locations such as are considered in this use case. The price for benzene and aromatics has more fluctuation, as seen in Figure 5.28.

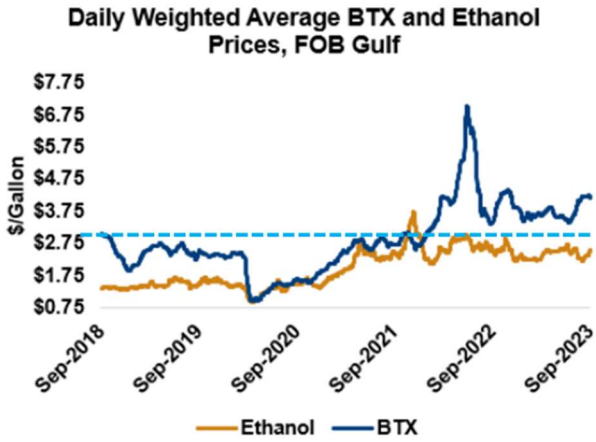

Figure 5.28: Average market price for aromatic chemicals from 2018-2023. The dashed blue line represents the approximate average for the price of BTX materials, around $3/gallon since 2018. Figure reproduced with permission from reference [112]

These two products can be combined to determine a gross profit value for the system. The aromatics product is assumed to be transported to a BTX facility or other customer, while the generated power is likely to be used onsite. Combining these profits is done using the following formula:

$$Gross\ Profits = E_{PCFC} * \frac{\$}{kWh} + BTX_{PCFC} * \frac{\$3}{gallon} \quad (5.1)$$

Where E_{PCER} is the electricity generated by the modular reactor, and BTX_{PCER} is the amount of BTX/aromatic product generated by the PCFC in gallons. The capital cost of the system is determined by combining the capital cost estimated by the Aspen-HYSYS software with an estimate of the PCFC manufacturing and installation costs. Notably, Aspen-HYSYS cost estimations largely ignore processes modeled by component splitters. As such, the

aromatics separator is considered to take the place of the PCFC with regard to the Aspen-HYSYS cost estimations; and the CCS is factored in afterwards as a lump sum and is assumed to be either a small-scale modular adsorption CCS or a modular CCS sold by Carbon Clean [113]. Modular CCSs have gradually become a more popular industry, with Carbon Clean offering an affordable 10 tCO_2/d CCS [113], [114].

PCFC installation costs are relatively complex, and a trusted approach for estimating this important factor was not available at the time of this writing. Instead, the average ratio between the equipment and installation costs of the balance of plant components in the Aspen-HYSYS economic analyzer tool is applied to the PCFC equipment cost to provide an estimate for the PCFC installation. This factor likely has the largest potential margin of error of the factors considered in the cost analysis. Once the gross profits are calculated, the total spending per year can be subtracted to find the net revenue per year of the system's operation.

$$Net\ Revenue = Gross\ Profits - \left(O\&M + C_{Transport} + Cap\right) \tag{5.2}$$

Where $O\&M$ represents the annual operations and maintenance cost as directly calculated by Aspen-HYSYS, plus an additional \$70/kW for the PCFC, $C_{Transport}$ represents the cost of transporting the aromatic chemicals from the wellhead to a customer or BTX facility, and Cap represents a yearly payback of 10% of the system capital costs for a total payback period of 10 years, after which time this factor can be removed for additional profit.

The transportation costs can be significant when there is no piping infrastructure, as considered here in the use case. For this cost, a variety of factors are considered, including the hourly rate for a truck driver, cost of two 60,000 lb trailers, one truck, vehicle

maintenance, and a 500-mile round trip distance. Two trailers are needed so that aromatics can continue to be stored during transportation. The values considered and references from which they are taken are shown in Table 5.8.

Table 5.8: Transportation Cost Factors

Factor	Cost	Reference
mean annual driver cost per the Bureau of Labor Statistics	$53,090.00	[115]
assumed trip distance (miles)	500	Use Case
assumed mpg	7	Use Case
estimated diesel price per gallon	$4.50	Use Case
cost of 60klb capacity tractor/trailer	$250,000.00	[116]
cost of spare trailer	$100,000.00	[116]
annual maintenance/contingency for tractor/trailer	$70,000.00	[116]
Upfront cost payback period	5 years	Use Case

5.2 Competing Technologies

To establish grounds for whether the suggested technology is economically viable, some target ranges can be determined based on the competing technologies. Considering the dual purpose of the modular PCFC system, targets are first established based on existing GTL facilities, and additional targets are set based on power production technologies.

5.2.1 Existing chemical production costs

Ramberg, et al.[117] performed an impressive study on the economic viability of GTL processes. They estimated that standard, industrial GTL plants have a capital cost of $68k per b/d capacity. This estimation is determined by examining the capital, operations and maintenance, labor, and natural gas input costs associated with plants on a scale of

~120,000 b/d of output, implying approximately $8.16 billion in initial capital costs. The operations and maintenance costs are further estimated as 4% of the capital cost, with an expected lifetime of ~25 years[117]. For FTS specifically, Albrecht and Nguyen[118] performed a techno-economic analysis that estimated 64.744 GWh per year is used to produce 116.257 metric kilotons of products. Assuming a crude oil ratio of 7.33 barrels per ton, this equates to ~76 kWh per barrel of product, which highlights the energy-intensive nature of FTS technology, and GTL in general. Considering this, and a price of $0.07/kWh, which is the approximate industrial average since 2010 [119], a GTL/FTS facility would spend an additional $6.6 billion over the 25 year lifetime of operation in energy input costs. To generate a target value for capital costs for the PCFC system, this energy input cost can be added to the capital cost since the PCFC would ideally generate enough power to provide a surplus of energy after fueling all the balance of plant components. In summary, an overall target capital cost value of around ~$120k per b/d capacity would suggest that the modular reactor system is competitive with existing GTL technologies.

However, the cost is not the only consideration when comparing GTL and the PCEC function of the PCER technology. There are a variety of factors that play significant roles in the economic viability of GTL processes, mainly the distance to the consumer and the trends of the oil and gas market. GTL processing is a clear second choice after power production and other uses and is only mainly implemented when the oil and gas market is right and the distance from the wellhead to the consumer is moderate to large, as depicted in Figure 5.29.

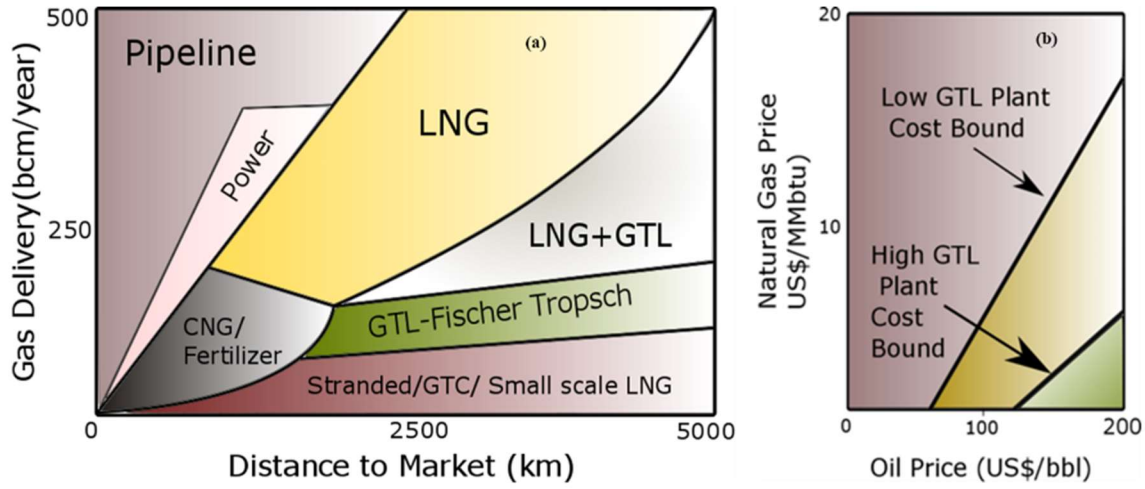

Figure 5.29: Techno-economic analysis of potential stranded gas monetization technologies; Possible options available for different sources (left); the impact of oil and gas prices on the feasibility of GTL technologies (right)

While the distance to market plays a role (as seen by the fading color at greater distances in Figure 5.29, GTL technology is mainly limited by the prices of oil and gas. It is only economical when gas prices are low and oil prices are moderate to high. This is because GTL products are often used in conjunction with oil and therefore the marketability of GTL products is largely dependent on oil prices.

These factors combine to severely limit the potential environmental benefits of FTS and GTL technology making use of stranded gas. In short, FTS and GTL processes are a massive investment in a process that is only economically viable under certain oil to natural gas price ratios as noted in Figure 5.29.

The viability under only certain price ratios will remain a limitation of industrial GTL technology. However, the MDA PCFC technology, while still a GTL process, does not necessarily follow these same guidelines. The modular PCFC is employed to harness stranded/flared natural gas, meaning the intended fuel is likely to simply be too expensive to economically transport to a GTL or other processing facility. Therefore, the cogenerating

modular reactor is able to harness a wholly new area of the gas market that has been largely wasted to this point. Figure 5.30 shows the target area for oil to gas price ratios. This new target area should provide an excellent economic advantage in the implementation of the PCFC system. Flared natural gas is normally wasted at a loss, and therefore the feedstock for the proposed reactor is considered free.

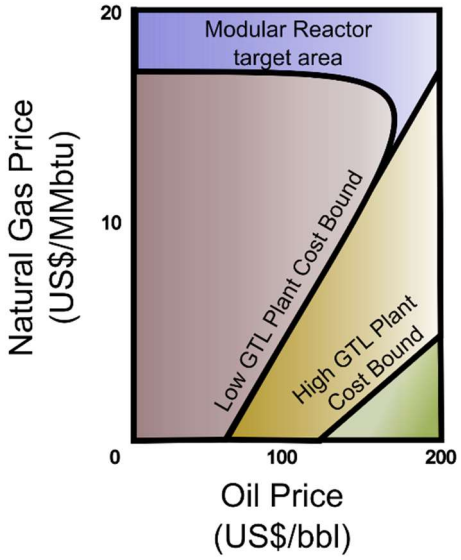

Figure 5.30: Intended oil-to-gas price ratios, adjusted for the suggested technology

Existing power production costs

5.2.2 Existing power production costs

Natural gas power plants are one of the most mature and well-researched power production technologies available in the modern era. Natural gas power plants generate 40% of the power in the U.S., significantly more than any other singular technology [120]. As such, they represent the standard for cost comparisons of power production at an industrial scale in the U.S. Every year, reports are generated that highlight the price and capacity of newly constructed and existing power plants. On average in 2020, a natural gas power plant had a

total construction cost of $1,116 per kW of power capacity [121]. New natural gas power plants are being constructed with an average capacity of 235.6 MW [121].

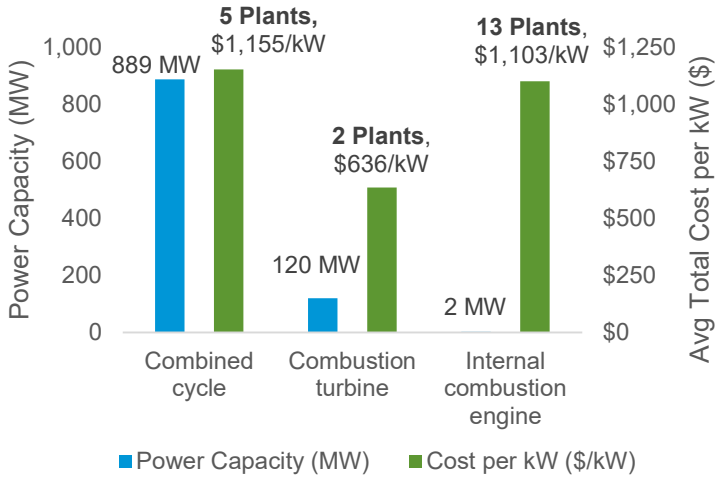

Figure 5.31: Construction Cost Data for Natural Gas Power Generators in 2020. [121]

As seen in Figure 5.31, the vast majority of investments in power production fall into the category of combined cycle natural gas power plants. The total investment in this technology alone was more than $5 billion in 2020 [121].

It is important to also recognize that the environment also pays a price for these power production technologies. Oil, gas, and coal all produce emissions when used for power production. However, natural gas power plants generally have fewer emissions when compared to coal and oil being used to produce the same amount of energy [122]. Despite this, natural gas power plants still account for around 34% of the total U.S. energy-related emissions [122].

An ambitious target value might then be set around $1,155/kW for a PCER system in order to compete with the most popular power production technology, but this may prove

difficult given the immaturity of fuel cells as a technology. Another important figure is the feedstock to power ratio. As reported by the U.S. Energy Information Administration, the standard natural gas consumed per kWh is 7.36 scf/kWh [123]. Achieving a value close to this ratio or its approximate equivalent of 0.15 kg_{CH4}/kWh would also help prove the effectiveness of the system, since it is a direct indicator of how well natural gas is turned into usable energy.

Despite the maturity of natural gas power plants, many investors and government-funded programs are looking into alternative energy production routes due to the environmental issues already mentioned. Figure 5.32 shows the costs associated with the most popular energy routes currently being investigated at a significant level as of 2020 [121].

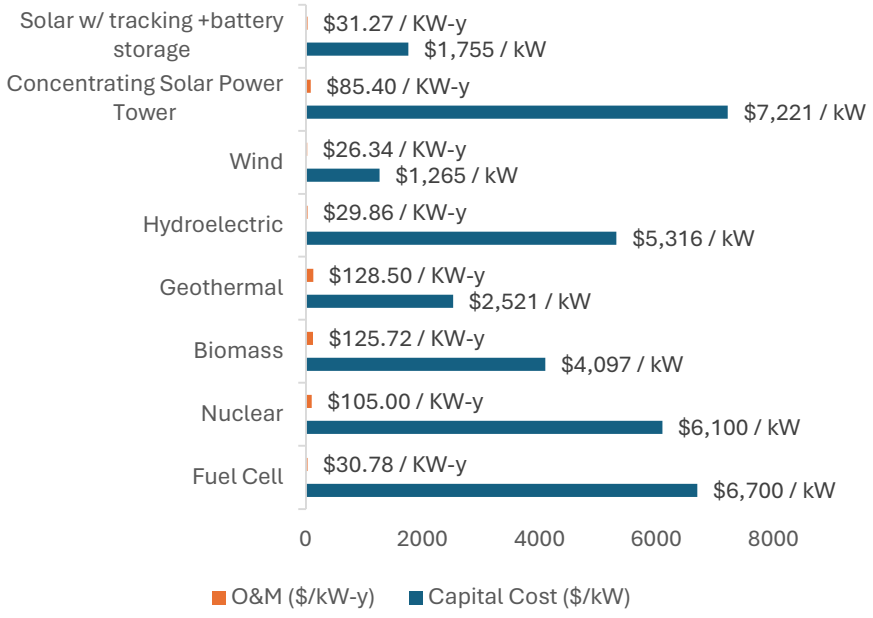

Figure 5.32: Alternative energy production routes featuring yearly O&M costs (on top) and system-level capital costs (on bottom)

The fuel cell category located at the bottom of Figure 5.32 displays numbers collected from Bloom Energy's SOFC systems, not PCFCs. So, while they represent a rough baseline, it is largely expected that PCFCs have the potential to be cheaper [124], but no previous system level cost analysis for PCFCs has been performed to verify that assumption. Of the reported alternative energy production systems, the average value for system capital costs is ~$4,370, while the average O&M costs are ~$70/kW-y. These values represent better target ranges for the readiness of the suggested technology. When combined with the earlier analysis of natural gas power systems, a final system capital cost between $1,155-$4,370 per kW would be an ideal outcome to ensure its competitiveness with existing technology.

5.2.3 Efficiency Analysis of PCERs vs Competing Technology

Ideally, the efficiency of the new technology will either meet or exceed that of existing practices. This section compares the modeled PCFC with industry standards in areas like conversion efficiency for chemical production, faradaic efficiency, and thermal efficiency. The numbers used for industry standards come from reported government data and chemical processing studies for FTS and other value-added chemical production processes for chemicals like benzene, and naphtha.

Conversion efficiency

FTS plants commonly convert in excess of 90% of the provided methane into syngas. However, the FTS process usually only converts about 60% of the syngas into the desired product in a single pass, resulting in a total conversion rate of ~54% [117], [125]. For BTX plants and aromatic production, there are several techniques that are commonly used

ranging from 13-46.6% conversion per-pass depending on the chosen method [46] as seen in Figure 5.33.

Unfortunately, conversion efficiency is one of the limiting factors of the effectiveness of the MDA PCFC and other similar membrane reactors for value-added chemicals. Table 5.9 shows several experiments involving aromatic chemical production from PCECs and PCERs, with the current standard limited to ~12%. The high in Table 5.9 is 18%, but this value is only achieved at an operating temperature that is far too high to be economically viable at the industrial level for PCERs.

Table 5.9: Recent protonic ceramic electrochemical studies for methane to aromatic chemical conversion [13]

Application	Configuration	Temp (C)	Reactant Composition	Conv. %	Selectivity %	Stability	Ref
PCEC for methane upgrading	Cu-Mo/H-MCM-22(Methane electrode) | $BaZr_{0.7}Ce_{0.2}Y_{0.1}O_{3-\delta}$(Electrolyte) |Ni-$Ba_{0.7}Zr_{0.7}Ce_{0.2}Y_{0.1}O_{3-\delta}$ (Hydrogen evolution reaction electrode)	710	10%CH_4/H_2	11.6	86.2 Aromatics	40h at 40 mA/cm^2	[73]
Proton membrane reactor for methane upgrading	Fe-$SiO_2SrCe_{0.8}Zr_{0.2}O_{3-\delta}$ (Methane side) | $SrCe_{0.7}Zr_{0.2}Eu_{0.1}O_{3-\delta}$ (Membrane)	980	90% CH_4/Ar	5.9	42.9 Aromatics	50h	[109]
		1000		10.1	46.4		
		1030		18.2	47.4		
Hydrogen-permeable membrane reactor for MDA	$La_{5.5}W_{0.6}Mo_{0.4}O_{11.25-\delta}$ (membrane) Mo/ HZSM-5 (catalyst)	700	CH_4	12	~75 Aromatics	10h	[126]

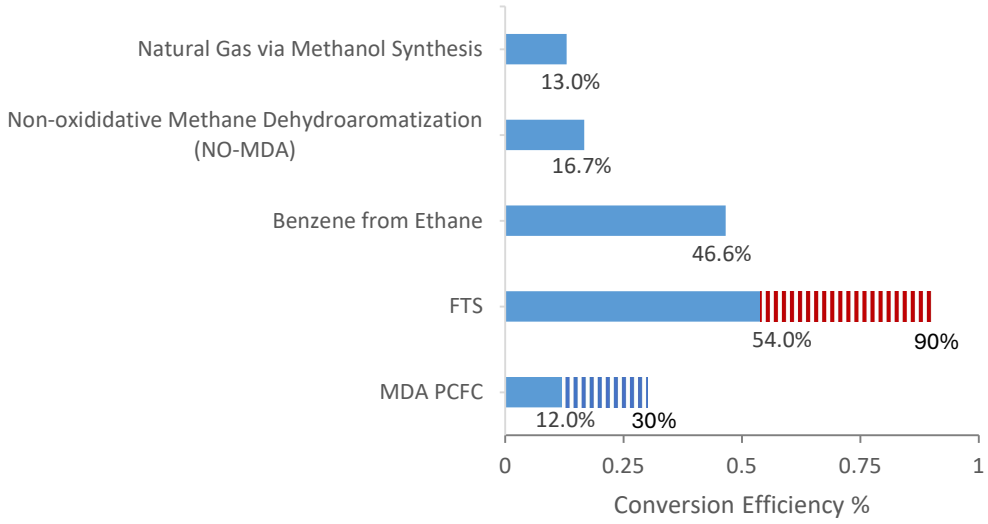

Figure 5.33: Comparison of conversion rates across the GTL industry. The slashed red area represents the net conversion rate for FTS after the initial 90% conversion is processed again to a final product. The slashed blue area represents the improvements shown by the model developed in this study compared to the industry standard.

Figure 5.33 provides an industry-wide comparison of conversion rates of various natural gas or methane to valuable products. The top 3 processes represent 3 of the most mature benzene production methods practiced at BTX facilities [46]. In the review work performed by Nithyanandam et al. [46], it was determined that NO-MDA is the most sustainable option for methane use with the current technologies available. The PCER, FTS, and BTX processes' conversion rates can be significantly enhanced by recycling, but the PCER and BTX have a lot more to gain by developing better catalysts to reduce recycling needs and increase output capacity. Additionally, increasing the conversion rate to the stated goal of 30% as shown in chapter 4 makes the PCER technology surpass current BTX facilities, and provides the PCER with a significant advantage over the "most-sustainable practice"[46] of NO-MDA.

Energy efficiencies

Traditional power plants are extremely mature technologies, but they are limited by the Carnot cycle and have therefore achieved a general overall efficiency of 60% [127]. A recent study by Otomo et al. [128] achieved a system-level efficiency as high as 74% with methane as fuel. This indicates that PCFCs have the potential to not only compete with, but *exceed* the efficiencies of competing technologies at the industrial scale. For the PCFC in this study, the system-level efficiency is calculated as

$$\epsilon_{sys} = \frac{LHV_{C_6H_6} \cdot \dot{m}_{C_6H_6} + LHV_{C_7H_8} \cdot \dot{m}_{C_7H_8} + P_{out}}{LHV_{CH_4} \cdot \dot{m}_{CH_4,converted} + LHV_{H_2} \cdot \dot{m}_{H_2,gen}}$$

where LHV_s and $\dot{m}_s$ represent the lower heating value and the mass flow rate of species *s*, respectively; P_{out} is the produced power, and subscripts $_{CH_4,converted}$ and $_{H_2,gen}$ represent the converted methane and generated hydrogen, respectively. At its peak form at 1 $Lg_{cat}^{-1}h^{-1}$, the system has an efficiency of 58.97%, on par with mature power generation technologies.

Another significant factor to consider is the input energy efficiency. A common way this is measured in electrochemical cells is through Faradaic efficiency, which measures how much of an electrical input is used directly to form the intended product. In other words, it is a ratio of the measured vs the theoretical maximum output selectivity in an electrochemical process. Duan, et al. has reported faradaic efficiencies around 90-98%, with a >97% overall electric-to-hydrogen energy conversion efficiency [72]. This is especially impressive since their work involved reversible PCFCs, which can switch from power generation to chemical (in this case, hydrogen) production, while maintaining high faradaic efficiencies in PCEC mode. In the model, the faradaic efficiency is most affected by the

overpotential losses. This would mean a faradaic efficiency near 100% for this system due to the low current density if not for the volt leakage modeled to meet the validation requirements. Because of the Volt leakage being set to 0.055 V, and the open circuit voltage coming out to around 1.003 volts, the faradaic efficiency rounds to 95% at all tested conditions.

Despite these great achievements, PCERs still have their limitations. Thermal efficiency is one of the weakest points of PCERs. The constant heat levels necessary for the ceramics to function as electrolytes usually results in a low thermal efficiency with an expected range of 15-29% [129], [130]. This is actually fairly competitive with solid oxide fuel cells, which operate around 18-35% thermal efficiency [129], [130]. Depending on the application of the PCER, the low thermal efficiency could provide an opportunity to recover heat for other energy-intensive processes, a tactic which is utilized in the cost analysis herein.

In contrast, a standard FTS plant boasts chemical and energy efficiencies of ~76% and 92%, respectively [118]. PCER technology is not likely to ever reach 92% thermal efficiency by itself, which is why system-level integration analyses are critical for PCERs to compete with FTS technology on this front.

5.3 Cost analysis of the protonic ceramic modular reactor technology

5.3.1 Estimating the MDA PCFC manufacturing cost

In contrast with FTS and natural gas power plants, PCFCs are a much less proven technology, with a significantly wider margin of error regarding cost analysis. PCECs

designed for chemical production outside of hydrogen have not received significant attention regarding techno-economic analyses. However, PCFCs have had several attempts for various applications, and they are commonly measured in price per kW similar to other power systems. The most versatile, and widely accepted techno-economic analysis to date was performed by Dubois et al. in 2017. The cell used for analysis had the characteristics shown in Table 5.10 [20]:

Table 5.10: Sample cell for Dubois cost analysis

Cell Composition	Anode: Ni(60%)/$BaZr_{0.8}Y_{0.2}O_{3-d}$(40%), Electrolyte: $BaZr_{0.8}Y_{0.2}O_{3-d}$, Cathode: $BaCo_{0.4}Fe_{0.4}Zr_{0.1}Y_{0.1}O_{3-d}$
Layer thickness	A: 500 μm, E: 20 μm, C: 40 μm
Power Density	.156 W/cm^2
Power Output	5kW
Active Area	~3.2 m^2

Almost every cell configuration is unique amongst PCFC studies, but this serves as an adequate baseline from which further assessment can be made. The result of Dubois' analysis regarding the PCFC unit is organized in Table 5.11.

Table 5.11: Specific PCFC manufacturing costs in $/kW assuming a power density of .156 W/cm^2[20]

Item(s)	**$/kW**
Raw PEN materials	19
Cell PEN manufacturing cost	52
Ball milling cost	17

Assembly and housing	38
Interconnects	63
Seals	118
Current collectors	58

It should first be acknowledged that Dubois et al. [20] noted that the seals, interconnects, and assembly carry the largest amount of uncertainty. Additionally, tubular cells require substantially less sealing compared to planar cells due to having a closed end. Therefore, this is an overly conservative estimate for the purpose of establishing a starting point for the cogenerating reactor.

Arguably the most important part of the PCFC, the membrane electrode assembly, only accounts for 24% of the total manufacturing cost of the PCFC. The other aspects can vary widely depending on whether tubular or planar dimensions are chosen, or if the model is based on additive or subtractive manufacturing [21], or other chosen manufacturing processes. Regardless, the total for cell is $365/kW [20]. At this rate, a 5kW cell stack with no balance of plant components would cost $1,825.

For comparison, Bloom Energy, a modern fuel cell manufacturer, currently has prices of ~$7-8,000/kW for SOFC [131]. This price can be broken down into ~$4,000/kW for the fuel cell system, and ~$2500/kW for installation, with a few other fees [129], [131], [132]. The greater specifics of how Bloom breaks down their prices is not publicly available.

Since the economic analysis by Dubois et al. [20] was in 2017 and utilized a planar geometry instead of a tubular, some updates for this application are reasonable. As shown in Figure 4.12a, the power density of the MDA PCFC system is significantly lower than what

was considered in the study by Dubois [20]. Therefore, instead of measuring the cost by kW as has been done historically, a price per square meter of active area is used instead. This results in a starting value of \$570.31/m^2. Considering the factors from Table 5.11, the anode thickness in the PCFC model is double that of the value used in [20], so the raw material cost is doubled. Due to advancements in cell manufacturing that include 3D printing processes for maximum raw material use [21], the manufacturing cost is considered to be reduced 40%. Ball milling remains the same as an important part of applying well-coated PEN layers [33]. The assembly and housing, interconnects, and current collector costs are reduced by 10% to account for advancements in manufacturing processes [130]. Lastly, the costs of seals are reduced by 80% due to the tubular configuration. This combination yields a price of \$252.9/kW, or ~\$395.2/m^2, which is not unreasonable considering further advancements since a 2021 cost estimation attempt that returned a value of \$260/kW for low-intermediate temperature PCFCs [132].

5.3.2 Cost analysis results

Using the values described above in the calculations and assumptions outlined for the model, the raw data from the projected economic results of implementing the PCER system are shown in Table 5.12. There are several companies that offer modular CCSs that would work for this application, but none of them have any posted prices, and those who have responded to inquiries have claimed their prices are under a non-disclosure agreement. So instead, it is assumed they can be purchased for \$1 million, which is lumped into the capital costs. In addition, CCS's require a lot of energy, of which 100kWh is being taken from the energy produced by the PCFC for a constant source, and the remaining

needed energy will ideally come in the form of heat from the PCFC outlet, which must be cooled and can provide 500-1150 kWh of heat energy depending on the chosen scenario. To determine trends and best future applications, four scenarios are considered, wherein the 177 kg/h average flow through the system represented 1, 1.5, 2, and 3 $Lg_{cat}^{-1}h^{-1}$. Each scenario is adjusted to operate at its peak power density, which are approximately 0.016, 0.018, 0.02 and 0.023 A/cm^2, respectively. Naturally, small amounts of water may need to be added to maintain the 5% water in the inlet stream, which is important to ensure appropriate hydrogen levels throughout the cell for the current to draw on. This is represented by the utilities cost gradually increasing with the space velocity in Table 5.12.

Table 5.12:Summary of capital cost breakdown

	1 $Lg_{cat}^{-1}h^{-1}$	**1.5 $Lg_{cat}^{-1}h^{-1}$**	**2 $Lg_{cat}^{-1}h^{-1}$**	**3 $Lg_{cat}^{-1}h^{-1}$**
Total Capital Cost [$]	$ 8,419,463	$ 7,995,299	$ 7,629,575	$ 6,671,092
Total Operating Cost [$/Year]	$ 962,227	$ 966,536	$ 970,400	$ 977,603
Utilities Cost [$/Year]	$ 46,346	$ 50,286	$ 53,716	$ 60,282
Aromatics Transportation ($/year)	$ 148,661	$ 147,901	$ 147,311	$ 146,304
Total BTX Product Sales [$/Year]	$ 880,215	$ 802,974	$ 742,975	$ 640,641
Total Electric Benefit [$/Year]	$ 790,748	$ 837,952	$ 858,680	$ 924,670
Desired Rate of Return [%/Year]	10%	10%	10%	10%
Equipment Cost [$]	$ 3,476,264	$ 3,065,915	$ 3,195,165	$ 3,043,403
Total Installed Cost [$]	$ 4,679,556	$ 3,810,239	$ 4,170,766	$ 3,364,045

Interestingly, Aspen-HYSYS did not significantly adjust its estimations for balance of plant equipment and operations costs when recycling is increased. This may be for a similar

reason that the aromatic transportation changed minimally. With increasing space velocities, emissions are slightly increased in the PCFC, leading to fewer aromatic delivery trips. However, the difference made by paying the driver, getting gas, etc. is relatively insignificant compared to the initial startup cost of purchasing the trailers. Additionally, after 5 years, the aromatic transportation costs go down by approximately $70,000 per year until a new truck needs to be purchased due to a five year payback period on the transportation costs.

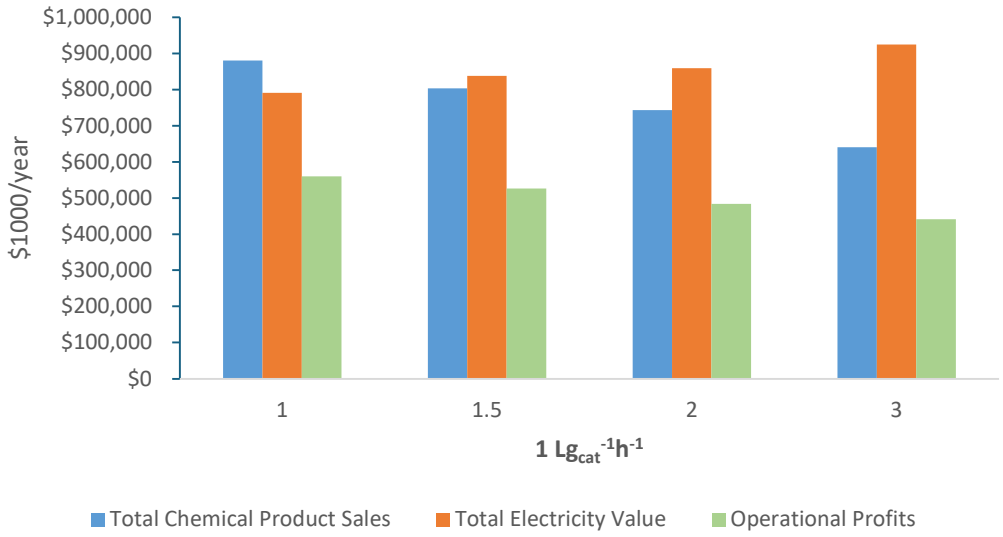

Figure 5.34: Space velocity effect on operational profit margins

For net profits, clear trends are seen in Figure 5.34 as the gap between profits from electrical and chemical products widens with increasing space velocity. Focusing on electrical power appears to have a slight but noticeably negative effect on the overall operational profits of the system. The operational profits are defined as the gross income minus the operational costs, ignoring debts for capital startup costs. When capital costs are

included year over year, Figure 5.35 shows an approximate 13 year payback period, followed by a linear increase in total profits from the system.

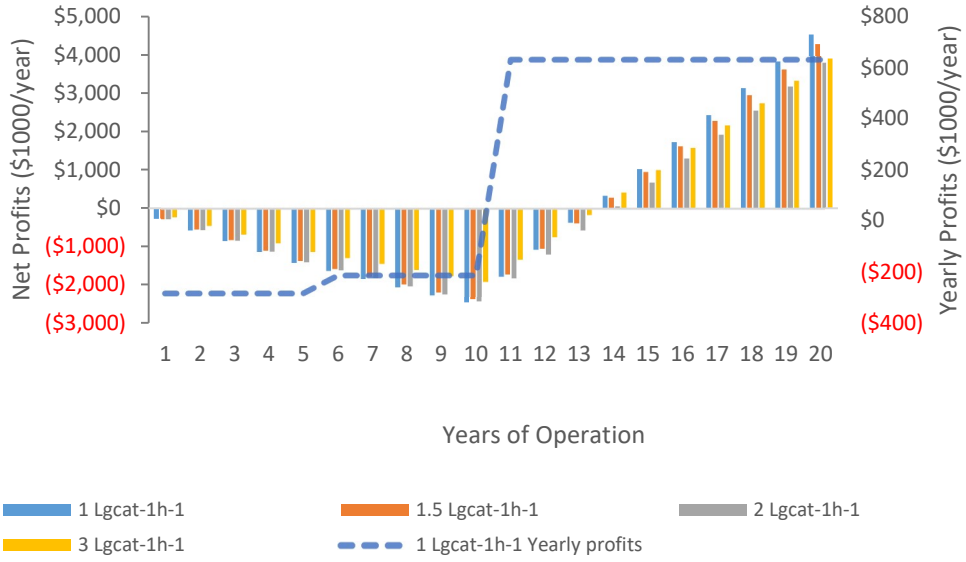

Figure 5.35: Cumulative net profits by years of operation

In Figure 5.35, all scenarios clearly lose increasing amounts of money for the first 10 years of operation. After 5 years, the transportation gets cheaper, but the effect is almost negligible. Scenarios 1, 2, and 4 break even by year 14, while scenario 3 follows suit by year 15, at which point scenario 1 with 1 $Lg_{cat}^{-1}h^{-1}$ will generate the most net profits going forward due to its higher operational profits and prioritization of chemical production compared to the other scenarios. A 13 year payback period is significantly behind the industry standard, which would ideally place the payback period $\leq$ 10 years for capital projects [133].

Table 5.13: Comparing results with competitive target values

Space Velocity	**kg/kwh**	**Cap $/kW**	**Cap per Output [$/bbl/d]**
1 $Lg_{cat}^{-1}h^{-1}$	0.2	$8756	$387,392
1.5 $Lg_{cat}^{-1}h^{-1}$	0.19	$7840	$400,379
2 $Lg_{cat}^{-1}h^{-1}$	0.19	$7269	$410,089
3 $Lg_{cat}^{-1}h^{-1}$	0.18	$5817	$406,836
Target	0.15	$1155 – $4370	$120,000

The values in

Table 5.13 are representative of the PCFC's performance compared to the target values outlined by discussing competing technologies. The results of this table indicate that the current implementation of the PCER system is generally behind that of its GTL and power production competitors. However, its competitors generally do not perform both chemical and power production simultaneously. The closest target is the efficiency of converting methane/natural gas into power. All of the scenarios operate with a CE between 73-77% for hydrogen, and as a significant amount of energy is also spent producing aromatics, the system is much more efficient than the individual numbers might portray.

For the modeled system, excluding the CCS, the PCFC makes up an average of a massive 85% of the total equipment cost across the four scenarios. This is in large part due to the significant active area required to keep pace with the necessary flowrate. The price associated with manufacturing the cell could be decreased as improvements in the kinetics or manufacturing methods are made. However, while improvements in the catalyst or locating additives to speed up the kinetics of the MDA reactions would take a significant cut out of these expenses, it is unlikely that the improvements necessary can be made quickly given the history of conversion limitations for MDA (see Table 5.9). Further advancements in PCFC manufacturing are much more likely with a current trajectory of significant improvement. The effect of improving the manufacturing cost is shown in Figure 5.36:

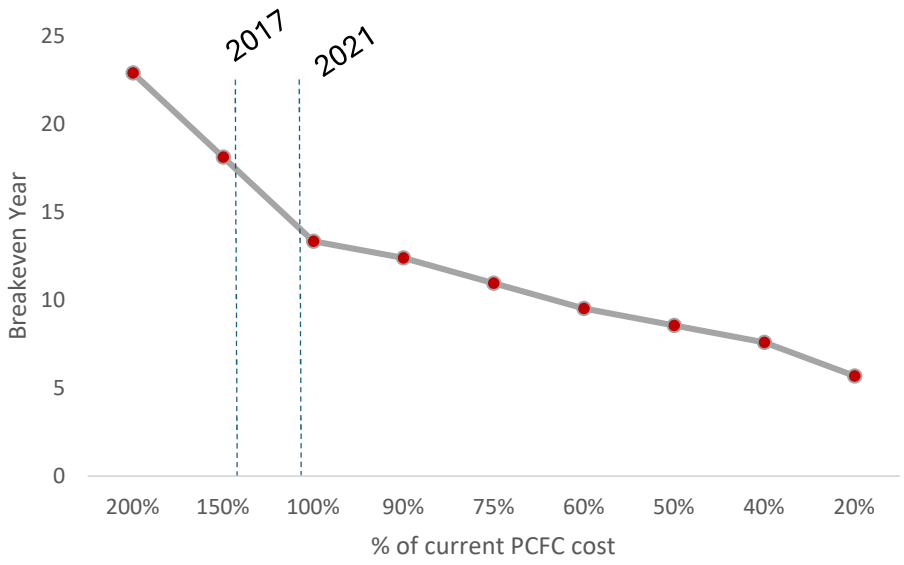

Figure 5.36: Impact of manufacturing cost on the breakeven year of the PCFC system. The dashed lines reference the manufacturing cost estimations from Dubois et al. [20] and O'Hayre et al. [132] for 2017 and 2021, respectively

Figure 5.36 shows that the manufacturing cost alone has the power to make the system economically feasible. Had there been no progress since 2017, the breakeven point would have been approximately 17.6 years. As further improvements are made, the breakeven point for the system can reach 10 years if PCFCs can be manufactured for 65% of the current estimations in this study. This would correspond to a price of approximately $165/kW for a pure hydrogen-fed cell, as was considered in the estimated manufacturing costs from 2021 [132].

A final important note is the effect that the distance to market has on the system. Figure 5.37 shows the relationship between the annual transportation costs and the distance to market assuming that all trips throughout the year are to the same distance or customer. It is highly likely that the distance will never have a need to exceed ~2000 km, especially considering the use case example of North Dakota, which is centrally located in

the U.S. The transportation costs shown in the tables and figures above assume a distance of 800 km. The value shown at ~2000 km in Figure 5.37 is only ~$25,000 more than the ~160 km value. This is a very affordable adjustment and proves that the distance to market should not play a significant role in hindering the profitability of the MDA PCFC system.

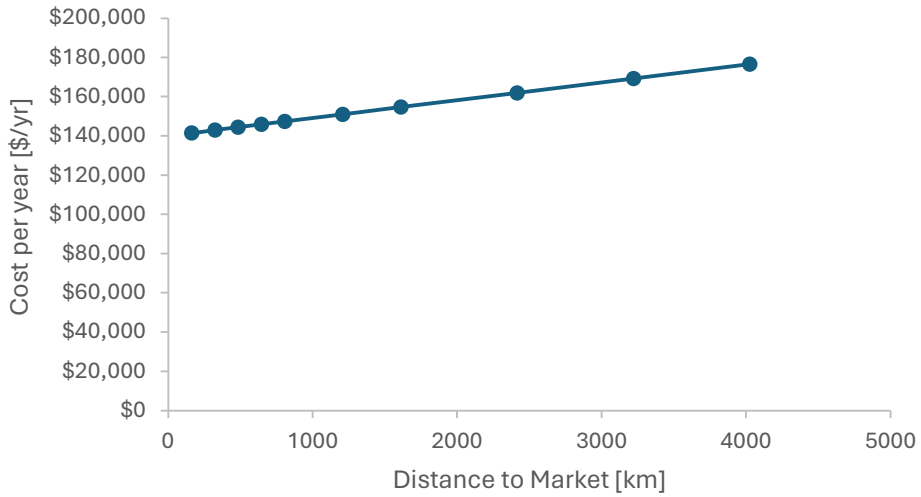

Figure 5.37: Effect of distance to market on transportation costs

Overall, the MDA PCFC falls a little short of the economic expectations needed for deployment. However, it also appears to be very close to achieving economic viability. With an effective CE of ~75%, and a fuel conversion rate of up to 30%, a lot of progress has already been made to make this a viable flaring solution. The largest obstacle is the manufacturing of the cell, which dwarfs the other components needed to make it successful.

It should also be noted that this analysis is performed without the assumption of any grants or tax credits. There are several significant tax credits and grants that exist to help with fuel cell applications. For example, the U.S. currently has a tax credit for 30% of the total fuel cell cost up to $100,000 [134], [135]. These can be taken into consideration to make the technology more profitable in the short term.

5.3.4 Environmental Considerations

Emissions rate is the primary environmental concern for most industrial processes, especially for power generation. The average CO2 emissions from converting natural gas to energy in the U.S. is 971.36 lbs/MWh produced [136]. Implementing technologies that can lower this average is critical for decreasing the country's emissions as a whole.

GTL technology is one of the leading practices with a lot of potential to harness leftover gas to reduce emissions. Ideally, all stranded, flared, or vented gas would be routed through GTL facilities to mitigate environmental impacts. However, even these GTL processes produce significant GHG emissions due to the high energy inputs required for reforming.

Without the balance of plant, the PCFC model by itself (and some water) is predicting an emission between 17-19 mol% emissions. The Aspen-HYSYS model adds 5.5% to that number due to the fired heater directly combusting a small portion of the feed to heat the PCFC inlet stream. However, it is possible that the CCS may be able to mitigate these emissions. Additionally, while not factored into this evaluation, Carbon Clean advertises that their modular system should make it easy to prepare the captured carbon for sequestration or other environmentally friendly means of disposal [113]. This is an avenue worth further exploration as it could potentially reduce direct emissions to net zero.

5.3.3 Safety and risk assessment

As with any plant process, there are inherent risks and safety measures to be followed in the management of processing equipment. The two largest safety concerns in the PCER

considered here are the high-temperature environment and the sulfur content in natural gas. Both of these factors have proven to significantly increase the rate of degradation of solid oxide fuel cells [137]. PCERs operate at lower temperatures compared to SOFCs, but >500 °C can still have a harmful effect on many materials. The durability of the materials in high-temperature environments is often one of the first topics of study when new catalysts and electrodes are implemented.

Sulfur content is highly moderated in natural gas pipelines due to its corrosive effects and is currently limited to 17 ppm in U.S. pipelines [12]. Duan, et al. tested PCFC's durability in sulfuric environments and found that 19 ppm did not noticeably degrade fuel cell performance even after 1000 hours [12]. This discovery greatly enhances the prospect of PCFC use at oil production sites. Raw natural gas is likely to still need to be processed prior to exposure to the modular reactor, but Duan's work still represents a substantial improvement over other fuel cell types, which have been known to be limited to <1 ppm sulfur content [129]. Proper safety precautions are always necessary in the presence of sulfur, but there is no indication that the PCFC technology introduces any increased risk for sulfur exposure due to degradation, leaks, or other causes over existing practices.

5.3.4 Evaluation Conclusion

This cost analysis is meant to provide an estimate for the readiness of a theoretical MDA PCFC for deployment within the parameters of the use case scenario. While boasting excellent conversion efficiencies, massively improved conversion, and net positive operational profits, there is still work to be done before this becomes a viable solution. The following summarize key points from this chapter:

- The choice of what space velocity to use may be decided less on emissions and money and more about the relatively unknown heat requirements of the CCS. For example, if the CCS requires more heat, then a higher space velocity may be useful to supply that heat through the recycling streams or in place of a cooler.
- Slower flow rates (i.e. 1 $Lg_{cat}^{-1}h^{-1}$) yield the best combination of power and chemical profits, providing bigger post payback period payouts.
- The technology "as is" requires a 13 year payback period, with most of the capital cost coming from the manufacturing and installation of the PCFC
    - Decreasing the price per square meter is more important than decreasing the price per square kW, as has been the focus of other studies. This is due to the low power densities of the MDA PCFC making the area larger and therefore a bigger focus of future development needs.
    - A target of $165/kW manufacturing price for a hydrogen-fed cell would provide the system with a breakeven year competitive with the industry.
- The MDA PCFC is not yet capable of competing directly with mature GTL and power technologies individually. However, the potential to exceed them is very real if manufacturing costs can continue the current trend of innovation and improvement.

    - While it cannot compete with the cost of other power generation technologies, the system level efficiency of 57.2% is on par with most mature power production system efficiencies
- The distance to market for the aromatic products is not a significant factor in the economic viability of the PCFC system.
- The catalyst is very effective in comparison to other GTL technologies when hydrogen is actively removed. As such, further catalyst development is less important than cheaper manufacturing techniques.

Chapter 6: Conclusion

6.1 Conclusions

In this thesis, a model is created for a PCFC intended to operate using MDA reactions at a remote flare site, and a performance and economic evaluation of that system is conducted. The primary takeaways from the work are summarized as follows:

- The developed PCFC model uses proven validation data, energy and mass balances, tested electrochemical formulations, and effective kinetic data to represent an accurate prediction of how the system would perform using existing catalysts and PCFC manufacturing methods.
- Utilizing current technology, a PCFC designed for MDA at a flare site is not competitively profitable. With a breakeven point between 13 and 14 years for the system, this would not meet most petrochemical companies goals of a 10 year maximum payback period [133].
- Further developments in PCFC manufacturing are likely to be the biggest hinge point in proving the economic viability of the PCFC system. A target value of $165/kW is identified in order to achieve acceptable profitability levels. This value relates to hydrogen-fed PCFCs.

- Regarding DOE goals of 30% fuel conversion, 50% aromatic selectivity, and 90% emissions reduction, the conversion and selectivity goals are proven to be achievable. However, due to water being needed to help jumpstart the electrochemical reactions, the 90% emissions reduction remains out of reach for this technology, especially when considering balance of plant components. Emissions for the system are consistently between 17-23% depending on flowrates and water levels in the fuel.
- The kinetics of MDA are extremely slow, particularly in comparison to methane reforming reactions. Water in the system needs to be limited to maintain a decrease in emissions, but also needed to help start the reactions.
    - Slower flowrates help prioritize the MDA reactions. Of the tested space velocities, 1 $Lg_{cat}^{-1}h^{-1}$, is the best flowrate and also the only one able to achieve the 30% fuel conversion target.
- While the exact MDA reaction mechanism may not be known, the reaction can be effectively predicted using ethylene as the intermediate product.

6.2 Future Work

This study proves the potential of PCFC and MDA integration is promising, but a variety of further work is required to both validate the results shown here, and continue the development of a growing fuel cell research field:

- The most important factor in making PCFCs with MDA economically viable is the manufacturing cost. This cost *must* go down for this system to be deployed. As such, further developments in cost analysis to identify the largest contributors to this cost would be most crucial. Additionally, most cost estimations to this point have utilized planar cells, so no effective comparison exists for choosing a tubular over a planar configuration. Future especially considering recent 3D printing solutions that have made the tubular configuration much easier to manufacture [21]
- There is a significant gap in research regarding the study of MDA in PCFCs or other similar membrane reactor setups, especially regarding economics. This study had to make use of the research knowledge of these processes independently to merge them effectively. A full-scale techno-economic analysis including experimental data would be extremely valuable to the future research work in this field.
- MDA is a much more complex process than FTS and GTL processes, and even more so when combined with electrochemistry. The reaction mechanism of MDA alone is still relatively unknown. More studies have attempted to decipher these processes, but some new theories have only increased the complexity of MDA, such as hydrocarbon pooling. This reaction needs to be better understood before the kinetics can be significantly improved. As it stands, the mystery behind the MDA process is

likely one of the biggest contributors to the consistently limited speed of MDA reactions.

- Finally, the balance of plant is not yet fully defined for the system in literature. This makes the balance of plant used in this study relatively questionable. For example, heat exchangers could have been used to improve the system efficiency, but none are utilized here for simplicity. A standard setup of balance of plant components would help clarify site needs and possibly open the door to new markets.

References

[1] Royal Society, "Climate Change: Evidence and Causes 2020." Accessed: Oct. 15, 2023. [Online]. Available: https://royalsociety.org/-/media/Royal_Society_Content/policy/projects/climate-evidence-causes/climate-change-evidence-causes.pdf

[2] "CO_2 and Greenhouse Gas Emissions Data Explorer," Our World in Data. Accessed: Aug. 09, 2023. [Online]. Available: https://ourworldindata.org/explorers/co2

[3] H. Ritchie, P. Rosado, and M. Roser, "Greenhouse gas emissions," *Our World Data*, Sep. 2023, Accessed: Oct. 16, 2023. [Online]. Available: https://ourworldindata.org/greenhouse-gas-emissions

[4] "Methane and climate change – Methane Tracker 2021 – Analysis," IEA. Accessed: Oct. 16, 2023. [Online]. Available: https://www.iea.org/reports/methane-tracker-2021/methane-and-climate-change

[5] E. Geary, "Natural gas venting and flaring in North Dakota and Texas increased in 2019," U.S. Energy Information Administration. Accessed: Jul. 19, 2023. [Online]. Available: https://www.eia.gov/todayinenergy/detail.php?id=46176

[6] P. Springer, "North Dakota's gas flaring intensity is highest (by far) in nation," Twin Cities. Accessed: Jul. 19, 2023. [Online]. Available: https://www.twincities.com/2022/12/05/north-dakotas-gas-flaring-intensity-is-highest-by-far-in-nation/

[7] "Natural Gas Vented and Flared." Accessed: Sep. 07, 2023. [Online]. Available: https://www.eia.gov/dnav/ng/ng_prod_sum_a_EPG0_VGV_mmcf_a.htm

[8] D. R. Lyon *et al.*, "Concurrent variation in oil and gas methane emissions and oil price during the COVID-19 pandemic," *Atmospheric Chem. Phys.*, vol. 21, no. 9, pp. 6605–6626, May 2021, doi: 10.5194/acp-21-6605-2021.

[9] "Gas Flaring - Energy System," IEA. Accessed: Oct. 16, 2023. [Online]. Available: https://www.iea.org/energy-system/fossil-fuels/gas-flaring

[10] "DOE Announces $30 Million for Technologies that Create Valuable Products from Otherwise Wasted Natural Gas While Reducing Methane Emissions from Flaring," Energy.gov. Accessed: Sep. 06, 2023. [Online]. Available: https://www.energy.gov/fecm/articles/doe-announces-30-million-technologies-create-valuable-products-otherwise-wasted

[11] C. Duan, J. Huang, N. Sullivan, and R. O'Hayre, "Proton-conducting oxides for energy conversion and storage," *Appl. Phys. Rev.*, vol. 7, no. 1, p. 011314, Mar. 2020.

[12] C. Duan *et al.*, "Highly durable, coking and sulfur tolerant, fuel-flexible protonic ceramic fuel cells," *Nature*, vol. 557, no. 7704, Art. no. 7704, May 2018, doi: 10.1038/s41586-018-0082-6.

[13] F. Liu, D. Ding, and C. Duan, “Protonic Ceramic Electrochemical Cells for Synthesizing Sustainable Chemicals and Fuels,” *Adv. Sci.*, vol. 10, no. 8, p. 2206478, 2023, doi: 10.1002/advs.202206478.
[14] Z. Li *et al.*, “Protonic ceramic fuel cells for power-ethylene cogeneration: A modelling study on structural parameters,” *Energy*, vol. 264, p. 126193, Feb. 2023, doi: 10.1016/j.energy.2022.126193.
[15] Z. Li *et al.*, “Ethylene and power cogeneration from proton ceramic fuel cells (PCFC): A thermo-electrochemical modelling study,” *J. Power Sources*, vol. 536, p. 231503, Jul. 2022, doi: 10.1016/j.jpowsour.2022.231503.
[16] F. Liu, H. Deng, H. Ding, P. Kazempoor, B. Liu, and C. Duan, “Process-intensified protonic ceramic fuel cells for power generation, chemical production, and greenhouse gas mitigation,” *Joule*, vol. 7, no. 6, pp. 1308–1332, Jun. 2023, doi: 10.1016/j.joule.2023.05.009.
[17] K. Hong, J. Min, G. Min, Y. Bae, and J. Hong, “Carbon-neutral conversion of methane supported by Ni-(Rh, Co) bimetallic catalysts for low-temperature proton-conducting ceramic fuel cells,” *Chem. Eng. J.*, vol. 462, p. 142334, Apr. 2023, doi: 10.1016/j.cej.2023.142334.
[18] “Project Landing Page,” netl.doe.gov. Accessed: Jul. 19, 2023. [Online]. Available: https://netl.doe.gov/project-information
[19] A. V. Kasyanova, I. A. Zvonareva, N. A. Tarasova, L. Bi, D. A. Medvedev, and Z. Shao, “Electrolyte materials for protonic ceramic electrochemical cells: Main limitations and potential solutions,” *Mater. Rep. Energy*, vol. 2, no. 4, p. 100158, Nov. 2022, doi: 10.1016/j.matre.2022.100158.
[20] A. Dubois, S. Ricote, and R. J. Braun, “Benchmarking the expected stack manufacturing cost of next generation, intermediate-temperature protonic ceramic fuel cells with solid oxide fuel cell technology,” *J. Power Sources*, vol. 369, pp. 65–77, Nov. 2017, doi: 10.1016/j.jpowsour.2017.09.024.
[21] M. Zou *et al.*, “3D Printing Enabled Highly Scalable Tubular Protonic Ceramic Fuel Cells,” *ACS Energy Lett.*, vol. 8, no. 8, pp. 3545–3551, Aug. 2023, doi: 10.1021/acsenergylett.3c01345.
[22] F. Liu, L. Fang, D. Diercks, P. Kazempoor, and C. Duan, “Rationally designed negative electrode for selective CO2-to-CO conversion in protonic ceramic electrochemical cells,” *Nano Energy*, vol. 102, p. 107722, Nov. 2022, doi: 10.1016/j.nanoen.2022.107722.
[23] H. An *et al.*, “A 5 × 5 cm2 protonic ceramic fuel cell with a power density of 1.3 W cm–2 at 600 °C,” *Nat. Energy*, vol. 3, no. 10, Art. no. 10, Oct. 2018, doi: 10.1038/s41560-018-0230-0.
[24] X. Xu *et al.*, “Tailoring electronic structure of perovskite cathode for proton-conducting solid oxide fuel cells with high performance,” *J. Power Sources*, vol. 489, p. 229486, Mar. 2021, doi: 10.1016/j.jpowsour.2021.229486.
[25] M. Liang *et al.*, “Nickel-doped BaCo0.4Fe0.4Zr0.1Y0.1O3-δ as a new high-performance cathode for both oxygen-ion and proton conducting fuel cells,” *Chem. Eng. J.*, vol. 420, p. 127717, Sep. 2021, doi: 10.1016/j.cej.2020.127717.

[26] H. Shimada, Y. Yamaguchi, H. Sumi, and Y. Mizutani, “Enhanced La0.6Sr0.4Co0.2Fe0.8O3–δ-based cathode performance by modification of BaZr0.1Ce0.7Y0.1Yb0.1O3–δ electrolyte surface in protonic ceramic fuel cells,” *Ceram. Int.*, vol. 47, no. 11, pp. 16358–16362, Jun. 2021, doi: 10.1016/j.ceramint.2021.02.123.

[27] D. Cao, M. Zhou, X. Yan, Z. Liu, and J. Liu, “High performance low-temperature tubular protonic ceramic fuel cells based on barium cerate-zirconate electrolyte - ScienceDirect,” *Electrochem. Commun.*, vol. 125, p. 106986, Apr. 2021.

[28] M. Hou, Y. Pan, and Y. Chen, “Enhanced electrochemical activity and durability of a direct ammonia protonic ceramic fuel cell enabled by an internal catalyst layer,” *Sep. Purif. Technol.*, vol. 297, p. 121483, Sep. 2022, doi: 10.1016/j.seppur.2022.121483.

[29] M. Fu, K. Li, Y. Yang, Q. Zeng, L. Zeng, and Z. Tao, “Fabrication and study of LaNi0.6Fe0.4O3-δ and Sm0.5Sr0.5CoO3-δ composite cathode for proton-conducting solid oxide fuel cells,” *Sep. Purif. Technol.*, vol. 287, p. 120581, Apr. 2022, doi: 10.1016/j.seppur.2022.120581.

[30] R. Guo and T. He, “High-Entropy Perovskite Electrolyte for Protonic Ceramic Fuel Cells Operating below 600 °C,” *ACS Mater. Lett.*, vol. 4, no. 9, pp. 1646–1652, Sep. 2022, doi: 10.1021/acsmaterialslett.2c00542.

[31] J. Jing *et al.*, “Boosting Performance of a Protonic Ceramic Fuel Cell by the Incorporation of Active Nano-Structured Layers,” *ACS Sustain. Chem. Eng.*, vol. 11, no. 28, pp. 10303–10310, Jul. 2023, doi: 10.1021/acssuschemeng.3c00706.

[32] Q. Huang *et al.*, “Highly active and durable triple conducting composite air electrode for low-temperature protonic ceramic fuel cells,” *Nano Res.*, Feb. 2023, doi: 10.1007/s12274-023-5531-3.

[33] F. Liu *et al.*, “Lowering the operating temperature of protonic ceramic electrochemical cells to <450 °C,” *Nat. Energy*, vol. 8, no. 10, Art. no. 10, Oct. 2023, doi: 10.1038/s41560-023-01350-4.

[34] “CDC | Facts About Benzene.” Accessed: Dec. 09, 2023. [Online]. Available: https://emergency.cdc.gov/agent/benzene/basics/facts.asp

[35] “Benzene | Public Health Statement | ATSDR.” Accessed: Dec. 08, 2023. [Online]. Available: https://wwwn.cdc.gov/TSP/PHS/PHS.aspx?phsid=37&toxid=14

[36] A. M. Niziolek, O. Onel, and C. A. Floudas, “Production of benzene, toluene, and xylenes from natural gas via methanol: Process synthesis and global optimization,” *AIChE J.*, vol. 62, no. 5, pp. 1531–1556, 2016, doi: 10.1002/aic.15144.

[37] P. Duchêne, L. Mencarelli, and A. Pagot, “Optimization approaches to the integrated system of catalytic reforming and isomerization processes in petroleum refinery,” *Comput. Chem. Eng.*, vol. 141, p. 107009, Oct. 2020, doi: 10.1016/j.compchemeng.2020.107009.

[38] S. Ma, X. Guo, L. Zhao, S. Scott, and X. Bao*, “Recent progress in methane dehydroaromatization: From laboratory curiosities to promising technology,” *J. Energy Chem.*, vol. 22, no. 1, p. 1, Jan. 2013.

[39] K. Nam, H. W. Ryu, M. Y. Gim, and D. H. Kim, “Enhanced reactivity and stability in methane dehydro-aromatization over Mo/HZSM-5 physically mixed with NiO,” *Appl. Catal. B Environ.*, vol. 296, p. 120377, Nov. 2021, doi: 10.1016/j.apcatb.2021.120377.

[40] “Global Benzene Market Expected to See Strong Growth Fueled by Automotive, Construction, and Pharmaceutical Industries,” Yahoo Finance. Accessed: Dec. 09, 2023. [Online]. Available: https://finance.yahoo.com/news/global-benzene-market-expected-see-123300321.html
[41] K. Gao, “Methane Dehydro Aromatization: Thermodynamics, Catalysts, Kinetics, and Potential of Membrane Reactors,” Otto von Guericke University, Liaoning, China, 2015. Accessed: Dec. 11, 2023. [Online]. Available: https://d-nb.info/1078066469/34
[42] S. Han, D. J. Martenak, R. E. Palermo, J. A. Pearson, and D. E. Walsh, “The direct partial oxidation of methane to liquid hydrocarbons over HZSM-5 zeolite catalyst,” *J. Catal.*, vol. 136, no. 2, pp. 578–583, Aug. 1992, doi: 10.1016/0021-9517(92)90087-X.
[43] L. Wang, L. Tao, M. Xie, G. Xu, J. Huang, and Y. Xu, “Dehydrogenation and aromatization of methane under non-oxidizing conditions,” *Catal. Lett.*, vol. 21, no. 1, pp. 35–41, Mar. 1993, doi: 10.1007/BF00767368.
[44] N. Kosinov and E. J. M. Hensen, “Reactivity, Selectivity, and Stability of Zeolite-Based Catalysts for Methane Dehydroaromatization,” *Adv. Mater.*, vol. 32, no. 44, p. 2002565, 2020, doi: 10.1002/adma.202002565.
[45] V. Fila, M. Bernauer, B. Bernauer, and Z. Sobalik, “Effect of addition of a second metal in Mo/ZSM-5 catalyst for methane aromatization reaction under elevated pressures,” *Catal. Today*, vol. 256, pp. 269–275, Nov. 2015, doi: 10.1016/j.cattod.2015.02.035.
[46] R. Nithyanandam, Y. K. Mun, T. S. Fong, T. C. Siew, O. S. Yee, and N. Ismail, “Review on Production of Benzene from Petroleum Associated Gas by Dehydroaromatization, Partial Oxidation on Methane and Methanol-to-Aromatics Processes,” 2019. Accessed: Oct. 18, 2023. [Online]. Available: https://www.semanticscholar.org/paper/REVIEW-ON-PRODUCTION-OF-BENZENE-FROM-PETROLEUM-GAS-Nithyanandam-Mun/4fd0aff1b350c48b541f0c50b507f6c4965c278c
[47] J. Guo, H. Lou, and X. Zheng, “Energy-Efficient coaromatization of methane and propane,” *J. Nat. Gas Chem.*, vol. 18, no. 3, pp. 260–272, Sep. 2009, doi: 10.1016/S1003-9953(08)60127-9.
[48] X. Guo *et al.*, “Direct, Nonoxidative Conversion of Methane to Ethylene, Aromatics, and Hydrogen,” *Science*, vol. 344, no. 6184, pp. 616–619, May 2014, doi: 10.1126/science.1253150.
[49] H. Song, J. Jarvis, S. Meng, H. Xu, Z. Li, and W. Li, “Direct Systems: Methane Dehydroaromatization (MDA) and the Oxidative Coupling of Methane (OCM),” in *Methane Activation and Utilization in the Petrochemical and Biofuel Industries*, H. Song, J. Jarvis, S. Meng, H. Xu, Z. Li, and W. Li, Eds., Cham: Springer International Publishing, 2022, pp. 43–69. doi: 10.1007/978-3-030-88424-6_3.
[50] Y. Liu *et al.*, “Understanding the Preparation and Reactivity of Mo/ZSM-5 Methane Dehydroaromatization Catalysts,” *Chem. – Eur. J.*, vol. 28, no. 5, p. e202103894, 2022, doi: 10.1002/chem.202103894.
[51] N. K. Razdan, A. Kumar, B. L. Foley, and A. Bhan, “Influence of ethylene and acetylene on the rate and reversibility of methane dehydroaromatization on Mo/H-ZSM-5 catalysts,” *J. Catal.*, vol. 381, pp. 261–270, Jan. 2020, doi: 10.1016/j.jcat.2019.11.004.
[52] N. Kosinov, E. A. Uslamin, F. J. A. G. Coumans, A. S. G. Wijpkema, R. Y. Rohling, and E. J. M. Hensen, “Structure and Evolution of Confined Carbon Species during Methane

Dehydroaromatization over Mo/ZSM-5," *ACS Catal.*, vol. 8, no. 9, pp. 8459–8467, Sep. 2018, doi: 10.1021/acscatal.8b02491.
[53] N. Kosinov *et al.*, "Confined Carbon Mediating Dehydroaromatization of Methane over Mo/ZSM-5," *Angew. Chem. Int. Ed.*, vol. 57, no. 4, pp. 1016–1020, 2018, doi: 10.1002/anie.201711098.
[54] K. Skutil and M. Taniewski, "Some technological aspects of methane aromatization (direct and via oxidative coupling)," *Fuel Process. Technol.*, vol. 87, no. 6, pp. 511–521, Jun. 2006, doi: 10.1016/j.fuproc.2005.12.001.
[55] N. Kosinov and E. J. M. Hensen, "Reactivity, Selectivity, and Stability of Zeolite-Based Catalysts for Methane Dehydroaromatization," *Adv. Mater.*, vol. 32, no. 44, p. 2002565, 2020, doi: 10.1002/adma.202002565.
[56] L. Y. Chen, L. W. Lin, Z. S. Xu, X. S. Li, and T. Zhang, "Dehydro-oligomerization of Methane to Ethylene and Aromatics over Molybdenum/HZSM-5 Catalyst," *J. Catal.*, vol. 157, no. 1, pp. 190–200, Nov. 1995, doi: 10.1006/jcat.1995.1279.
[57] E. C. Corredor, P. Chitta, and M. D. Deo, "Techno-economic evaluation of a process for direct conversion of methane to aromatics," *Fuel Process. Technol.*, vol. 183, pp. 55–61, Jan. 2019, doi: 10.1016/j.fuproc.2018.05.038.
[58] E. C. Corredor, P. Chitta, and M. Deo, "Membrane reactor system model for gas conversion to benzene," *Fuel*, vol. 179, pp. 202–209, Sep. 2016, doi: 10.1016/j.fuel.2016.03.073.
[59] L. Li, R. W. Borry, and E. Iglesia, "Reaction-transport simulations of non-oxidative methane conversion with continuous hydrogen removal — homogeneous–heterogeneous reaction pathways," *Chem. Eng. Sci.*, vol. 56, no. 5, pp. 1869–1881, Mar. 2001, doi: 10.1016/S0009-2509(00)00465-6.
[60] I. Vollmer, E. Abou-Hamad, J. Gascon, and F. Kapteijn, "Aromatization of Ethylene – Main Intermediate for MDA?," *ChemCatChem*, vol. 12, no. 2, pp. 544–549, 2020, doi: 10.1002/cctc.201901655.
[61] Y. Zhu, N. Al-ebbinni, R. Henney, C. Yi, and R. Barat, "Extension to multiple temperatures of a three-reaction global kinetic model for methane dehydroaromatization," *Chem. Eng. Sci.*, vol. 177, pp. 132–138, Feb. 2018, doi: 10.1016/j.ces.2017.11.001.
[62] K. S. Wong, J. W. Thybaut, E. Tangstad, M. W. Stöcker, and G. B. Marin, "Methane aromatisation based upon elementary steps: Kinetic and catalyst descriptors," *Microporous Mesoporous Mater.*, vol. 164, pp. 302–312, Dec. 2012, doi: 10.1016/j.micromeso.2012.07.002.
[63] Z. Li, C. Kjølseth, S. H. Morejudo, and R. Haugsrud, "Numerical Simulations of Methane Aromatization with and without a Ceramic Hydrogen Separation Membrane," presented at the 2012 COMSOL Conference in Milan, Oslo, Norway: COMSOL, 2012. Accessed: Dec. 11, 2023. [Online]. Available: https://www.comsol.com/paper/numerical-simulations-of-methane-aromatization-with-and-without-a-ceramic-hydrog-13307
[64] J. Jeong, A. Hwang, Y. T. Kim, D.-Y. Hong, and M.-J. Park, "Kinetic modeling of methane dehydroaromatization over a Mo2C/H-ZSM5 catalyst: Different deactivation behaviors of the Mo2C and H-ZSM5 sites," *Catal. Today*, vol. 352, pp. 140–147, Aug. 2020, doi: 10.1016/j.cattod.2019.09.002.

[65] P. Zhu *et al.*, “Direct conversion of methane to aromatics and hydrogen via a heterogeneous trimetallic synergistic catalyst,” *Nat. Commun.*, vol. Accepted, 2024.
[66] Z.-G. Zhang, “Process, reactor and catalyst design: Towards application of direct conversion of methane to aromatics under nonoxidative conditions,” *Carbon Resour. Convers.*, vol. 2, no. 3, pp. 157–174, Dec. 2019, doi: 10.1016/j.crcon.2019.07.001.
[67] Z. Zhang, Y. Xu, Y. Song, H. Ma, and Y. Yamamoto, “NGU: Development of a two-bed circulating fluidized bed reactor system for nonoxidative aromatization of methane over Mo/HZSM-5 catalyst,” *Environ. Prog. Sustain. Energy*, vol. 35, no. 2, pp. 325–333, 2016, doi: 10.1002/ep.12287.
[68] A. Galadima and O. Muraza, “Advances in Catalyst Design for the Conversion of Methane to Aromatics: A Critical Review,” *Catal. Surv. Asia*, vol. 23, no. 3, pp. 149–170, Sep. 2019, doi: 10.1007/s10563-018-9262-5.
[69] Y. Xu, J. Lu, Y. Suzuki, Z.-G. Zhang, H. Ma, and Y. Yamamoto, “Performance of a binder-free, spherical-shaped Mo/HZSM-5 catalyst in the non-oxidative CH4 dehydroaromatization in fixed- and fluidized-bed reactors under periodic CH4–H2 switch operation,” *Chem. Eng. Process. Process Intensif.*, vol. 72, pp. 90–102, Oct. 2013, doi: 10.1016/j.cep.2013.05.016.
[70] P. L. Spath and D. C. Dayton, “Technical and Economic Assessment of Synthesis Gas to Fuels and Chemicals with Emphasis on the Potential for Biomass-Derived Syngas,” National Renewable Energy Laboratory, Golden, Colorado, Technical Report NREL/TP-510-34929, Dec. 2003. [Online]. Available: https://www.nrel.gov/docs/fy04osti/34929.pdf
[71] F. Almarri, B. Carv, T. Stevenson, A. A. Musabeh, and M. Alyousif, “Fischer-Tropsch Synthesis: Natural Gas to Diesel Fuel,” University of Wyoming, Oct. 13, 2014. doi: 10.15786/13702882.v3.
[72] C. Duan *et al.*, “Highly efficient reversible protonic ceramic electrochemical cells for power generation and fuel production,” *Nat. Energy*, vol. 4, no. 3, Art. no. 3, Mar. 2019, doi: 10.1038/s41560-019-0333-2.
[73] S. H. Morejudo *et al.*, “Direct conversion of methane to aromatics in a catalytic co-ionic membrane reactor,” *Science*, vol. 353, no. 6299, Aug. 2016, doi: 10.1126/science.aag0274.
[74] G. C. Mather, D. Muñoz-Gil, J. Zamudio-García, J. M. Porras-Vázquez, D. Marrero-López, and D. Pérez-Coll, “Perspectives on Cathodes for Protonic Ceramic Fuel Cells,” *Appl. Sci.*, vol. 11, no. 12, Art. no. 12, Jan. 2021, doi: 10.3390/app11125363.
[75] C. Stiller, “Design, Operation and Control Modelling of SOFC/GT Hybrid Systems,” Norwegian University of Science and Technology, Trondheim, Norway, 2006. [Online]. Available: https://ntnuopen.ntnu.no/ntnu-xmlui/bitstream/handle/11250/231300/125922_FULLTEXT01.pdf?sequence=1
[76] H. Xi, “Dynamic Modeling and Control of Planar SOFC Power Systems,” University of Michigan, Ann Arbor, MI, 2007.
[77] P. Kazempoor, V. Dorer, and O. Fathollah, “Modelling and Performance Evaluation of Solid Oxide Fuel Cell for Building Integrated Co- and Polygeneration,” *Fuel Cells*, vol. 10, no. 6, pp. 1074–1094, 2010, doi: 10.1002/fuce.200900082.

[78] P. Kazempoor and R. J. Braun, “Model validation and performance analysis of regenerative solid oxide cells for energy storage applications: Reversible operation,” *Int. J. Hydrog. Energy*, vol. 39, no. 11, pp. 5955–5971, Apr. 2014, doi: 10.1016/j.ijhydene.2014.01.186.

[79] H. Timmermann, W. Sawady, R. Reimert, and E. Ivers-Tiffée, “Kinetics of (reversible) internal reforming of methane in solid oxide fuel cells under stationary and APU conditions,” *J. Power Sources*, vol. 195, no. 1, pp. 214–222, Jan. 2010, doi: 10.1016/j.jpowsour.2009.07.019.

[80] W. Lehnert, J. Meusinger, and F. Thom, “Modelling of gas transport phenomena in SOFC anodes,” *J. Power Sources*, vol. 87, no. 1, pp. 57–63, Apr. 2000, doi: 10.1016/S0378-7753(99)00356-0.

[81] E. P. J. Mallens, J. H. B. J. Hoebink, and G. B. Marin, “The Reaction Mechanism of the Partial Oxidation of Methane to Synthesis Gas: A Transient Kinetic Study over Rhodium and a Comparison with Platinum,” *J. Catal.*, vol. 167, no. 1, pp. 43–56, Apr. 1997, doi: 10.1006/jcat.1997.1533.

[82] A. Bharadwaj, D. H. Archer, and E. S. Rubin, “Modeling the Performance of a Tubular Solid Oxide Fuel Cell,” *J. Fuel Cell Sci. Technol.*, vol. 2, no. 1, pp. 38–44, Aug. 2004, doi: 10.1115/1.1842781.

[83] K. Taghikhani, A. Dubois, J. R. Berger, S. Ricote, H. Zhu, and R. J. Kee, “Modeling Electro-Chemo-Mechanical Behaviors within the Dense BaZr0.8Y0.2O3−δ Protonic-Ceramic Membrane in a Long Tubular Electrochemical Cell,” *Membranes*, vol. 11, no. 6, Art. no. 6, Jun. 2021, doi: 10.3390/membranes11060378.

[84] R. J. Kee, S. Ricote, H. Zhu, R. J. Braun, G. Carins, and J. E. Persky, “Perspectives on Technical Challenges and Scaling Considerations for Tubular Protonic-Ceramic Electrolysis Cells and Stacks,” *J. Electrochem. Soc.*, vol. 169, no. 5, p. 054525, May 2022, doi: 10.1149/1945-7111/ac6c4e.

[85] P. Kazempoor and R. J. Braun, “Model validation and performance analysis of regenerative solid oxide cells: Electrolytic operation,” *Int. J. Hydrog. Energy*, vol. 39, no. 6, pp. 2669–2684, Feb. 2014, doi: 10.1016/j.ijhydene.2013.12.010.

[86] S. Campanari and P. Iora, “Comparison of Finite Volume SOFC Models for the Simulation of a Planar Cell Geometry,” *Fuel Cells*, vol. 5, no. 1, pp. 34–51, 2005, doi: 10.1002/fuce.200400057.

[87] S. H. Chan, K. A. Khor, and Z. T. Xia, “A complete polarization model of a solid oxide fuel cell and its sensitivity to the change of cell component thickness,” *J. Power Sources*, vol. 93, no. 1, pp. 130–140, Feb. 2001, doi: 10.1016/S0378-7753(00)00556-5.

[88] H. Zhu, S. Ricote, and R. J. Kee, “Thermodynamics, transport, and electrochemistry in protonic ceramic electrolysis cells,” in *High-Temperature Electrolysis: From fundamentals to applications*, IOP Publishing, 2023. doi: 10.1088/978-0-7503-3951-3ch12.

[89] J.-H. Zhang, L.-B. Lei, D. Liu, F.-Y. Zhao, M. Ni, and F. Chen, “Mathematical modeling of a proton-conducting solid oxide fuel cell with current leakage,” *J. Power Sources*, vol. 400, pp. 333–340, Oct. 2018, doi: 10.1016/j.jpowsour.2018.08.038.

[90] Y. Sahli, “Thermodynamic Modeling and Analysis of Proton Ceramic Fuel Cells: Power Optimization,” *Arab. J. Sci. Eng.*, vol. 47, no. 5, pp. 6355–6363, May 2022, doi: 10.1007/s13369-021-06262-7.

[91] P. Aguiar, C. S. Adjiman, and N. P. Brandon, “Anode-supported intermediate temperature direct internal reforming solid oxide fuel cell. I: model-based steady-state performance,” *J. Power Sources*, vol. 138, no. 1, pp. 120–136, Nov. 2004, doi: 10.1016/j.jpowsour.2004.06.040.

[92] K. Li, H. Shimada, Y. Mizutani, Y. Okuyama, and T. Araki, “Ultra-elevated power density and high energy efficiency of protonic ceramic fuel cells: Numerical and experimental results,” *Energy Convers. Manag.*, vol. 296, p. 117678, Nov. 2023, doi: 10.1016/j.enconman.2023.117678.

[93] B. Poling, J. Prausnitz, and J. O’Connell, *The Properties of Gases and Liquids*, 5th Edition. McGraw-Hill, 2000.

[94] S. Srisurichan, R. Jiraratananon, and A. G. Fane, “Mass transfer mechanisms and transport resistances in direct contact membrane distillation process,” *J. Membr. Sci.*, vol. 277, no. 1, pp. 186–194, Jun. 2006, doi: 10.1016/j.memsci.2005.10.028.

[95] “Copper - Density, Specific Heat and Thermal Conductivity vs. Temperature.” Accessed: Mar. 29, 2024. [Online]. Available: https://www.engineeringtoolbox.com/copper-density-specific-heat-thermal-conductivity-vs-temperature-d_2223.html

[96] C. Stiller, B. Thorud, S. Seljebø, Ø. Mathisen, H. Karoliussen, and O. Bolland, “Finite-volume modeling and hybrid-cycle performance of planar and tubular solid oxide fuel cells,” *J. Power Sources*, vol. 141, no. 2, pp. 227–240, Mar. 2005, doi: 10.1016/j.jpowsour.2004.09.019.

[97] K. P. Recknagle, R. E. Williford, L. A. Chick, D. R. Rector, and M. A. Khaleel, “Three-dimensional thermo-fluid electrochemical modeling of planar SOFC stacks,” *J. Power Sources*, vol. 113, no. 1, pp. 109–114, Jan. 2003, doi: 10.1016/S0378-7753(02)00487-1.

[98] H. Yakabe, T. Ogiwara, M. Hishinuma, and I. Yasuda, “3-D model calculation for planar SOFC,” *J. Power Sources*, vol. 102, no. 1, pp. 144–154, Dec. 2001, doi: 10.1016/S0378-7753(01)00792-3.

[99] T. Ota, M. Koyama, C. Wen, K. Yamada, and H. Takahashi, “Object-based modeling of SOFC system: dynamic behavior of micro-tube SOFC,” *J. Power Sources*, vol. 118, no. 1, pp. 430–439, May 2003, doi: 10.1016/S0378-7753(03)00109-5.

[100] S. Sharifi, A. R. Razmi, M. H. Nabat, J. J. Liu, A. Arabkoohsar, and M. Shahbakhti, “Power-to-X,” in *Future Grid-Scale Energy Storage Solutions*, Elsevier, 2023, pp. 621–646. doi: 10.1016/B978-0-323-90786-6.00003-0.

[101] S. Hajipour, “Economic Evaluation using Aspen HYSYS,” Process Ecology. Accessed: Apr. 21, 2024. [Online]. Available: https://processecology.com/articles/economic-evaluation-using-aspen-hysys

[102] J. Goyne, V. Holten, and R. Wang, “On-Site Flare Gas Utilization: Generating Electricity and Flue Gas for EOR.” Duke University, 2018. [Online]. Available: https://sites.duke.edu/adhoc_energy__environment_/files/2018/08/Flare-Gas_Flue-Gas-Poster.pdf

[103] American Petroleum Institute, *API 6A: Specification for Wellhead and Christmas Tree Equipment*, Nineteenth Edition. [Online]. Available: https://law.resource.org/pub/us/cfr/ibr/002/api.6a.2004.pdf
[104] J. Siažik and M. Malcho, "Accumulation of Primary Energy Into Natural Gas Hydrates," *Procedia Eng.*, vol. 192, pp. 782–787, Jan. 2017, doi: 10.1016/j.proeng.2017.06.135.
[105] *Natural Gas Sweetening Process with DEA || Aspen HYSYS*, (Nov. 18, 2021). Accessed: Oct. 18, 2023. [Online Video]. Available: https://www.youtube.com/watch?v=gXU2d0f4IeA
[106] *Amine Sweetening Unit with MDEA || Aspen HYSYS*, (Aug. 31, 2020). Accessed: Oct. 18, 2023. [Online Video]. Available: https://www.youtube.com/watch?v=G9kyi9OKVKg
[107] Railroad Commission of Texas, "Hydrogen Sulfide H2S Fields & Concentration Listings," Hydrogen Sulfide (H2S) Fields & Concentration Listings. Accessed: Oct. 09, 2023. [Online]. Available: https://www.rrc.texas.gov/oil-and-gas/research-and-statistics/field-data/hydrogen-sulfide-h2s/
[108] S. Joshi, H. Hussain, P. Tiwari, D. Rahman, and T. Aldajani, "IMPROVE GAS TURBINE/ENGINE PERFORMANCE AND REDUCE MAINTENANCE USING MEMBRANES FOR FUEL GAS CONDITIONING." MTR Inc, 2015. [Online]. Available: https://www.mtrinc.com/wp-content/uploads/2018/09/NG08-MTR-Power-Gen-NG-2015.pdf
[109] M. Sakbodin *et al.*, "Direct Nonoxidative Methane Conversion in an Autothermal Hydrogen-Permeable Membrane Reactor," *Adv. Energy Mater.*, vol. 11, no. 46, p. 2102782, 2021, doi: 10.1002/aenm.202102782.
[110] Y. Fan *et al.*, "Barium-doped Sr2Fe1.5Mo0.5O6-δ perovskite anode materials for protonic ceramic fuel cells for ethane conversion," *J. Am. Ceram. Soc.*, vol. 105, no. 5, pp. 3613–3624, 2022, doi: 10.1111/jace.18329.
[111] "Electric Power Monthly - U.S. Energy Information Administration (EIA)." Accessed: Sep. 20, 2023. [Online]. Available: https://www.eia.gov/electricity/monthly/index.php
[112] World Perspectives, Inc. and U.S. Grains Council, "Ethanol Market and Pricing Data Report: September 20, 2023." Accessed: Sep. 20, 2023. [Online]. Available: https://grains.org/ethanol_report/ethanol-market-and-pricing-data-september-20-2023/
[113] "Modular carbon capture systems for industry | Carbon Clean." Accessed: Apr. 22, 2024. [Online]. Available: https://www.carbonclean.com/modular-carbon-capture-systems
[114] "Carbon Clean launches modular CO_2 capture system," Chemical & Engineering News. Accessed: Apr. 22, 2024. [Online]. Available: https://cen.acs.org/environment/climate-change/Carbon-Clean-launches-modular-CO2/99/web/2021/11
[115] "Heavy and Tractor-Trailer Truck Drivers." Accessed: Oct. 06, 2023. [Online]. Available: https://www.bls.gov/oes/current/oes533032.htm
[116] ICF International, "Breakeven Analysis for Four Flare Gas Capture Options," Apr. 2016. [Online]. Available: https://www.edf.org/sites/default/files/content/blm_breakeven_analysis_memo_final_4_22_2016.reviewed.pdf

[117] D. J. Ramberg, Y. H. Henry Chen, S. Paltsev, and J. E. Parsons, “The economic viability of gas-to-liquids technology and the crude oil–natural gas price relationship,” *Energy Econ.*, vol. 63, pp. 13–21, Mar. 2017, doi: 10.1016/j.eneco.2017.01.017.
[118] F. G. Albrecht and T.-V. Nguyen, “Prospects of electrofuels to defossilize transportation in Denmark – A techno-economic and ecological analysis,” *Energy*, vol. 192, p. 116511, Feb. 2020, doi: 10.1016/j.energy.2019.116511.
[119] “U.S. industrial retail electricity price 2023,” Statista. Accessed: Apr. 22, 2024. [Online]. Available: https://www.statista.com/statistics/190680/us-industrial-consumer-price-estimates-for-retail-electricity-since-1970/
[120] “Electricity in the U.S. - U.S. Energy Information Administration (EIA).” Accessed: Apr. 22, 2024. [Online]. Available: https://www.eia.gov/energyexplained/electricity/electricity-in-the-us.php
[121] EIA, “Construction cost data for electric generators installed in 2020.” Aug. 23, 2022. Accessed: Sep. 16, 2023. [Excel]. Available: https://www.eia.gov/electricity/generatorcosts/index.php
[122] U.S. Energy Information Administration, “Natural gas and the environment.” Accessed: Oct. 18, 2023. [Online]. Available: https://www.eia.gov/energyexplained/natural-gas/natural-gas-and-the-environment.php
[123] “Frequently Asked Questions (FAQs) - U.S. Energy Information Administration (EIA).” Accessed: Aug. 16, 2023. [Online]. Available: https://www.eia.gov/tools/faqs/faq.php
[124] Colorado School of Mines, “Development of Intermediate-Temperature Fuel-Flexible Protonic-Ceramic Fuel Cells,” DEVELOPMENT OF INTERMEDIATE-TEMPERATURE FUEL-FLEXIBLE PROTONIC-CERAMIC FUEL CELLS. Accessed: Oct. 09, 2023. [Online]. Available: https://aes.mines.edu/development-of-intermediate-temperature-fuel-flexible-protonic-ceramic-fuel-cells/
[125] F. T. Alsudani *et al.*, “Fisher–Tropsch Synthesis for Conversion of Methane into Liquid Hydrocarbons through Gas-to-Liquids (GTL) Process: A Review,” *Methane*, vol. 2, no. 1, Art. no. 1, Mar. 2023, doi: 10.3390/methane2010002.
[126] J. Xue, Y. Chen, Y. Wei, A. Feldhoff, H. Wang, and J. Caro, “Gas to Liquids: Natural Gas Conversion to Aromatic Fuels and Chemicals in a Hydrogen-Permeable Ceramic Hollow Fiber Membrane Reactor,” *ACS Catal.*, vol. 6, no. 4, pp. 2448–2451, Apr. 2016, doi: 10.1021/acscatal.6b00004.
[127] “Combined-cycle gas turbines (2022),” Ipieca. Accessed: Oct. 09, 2023. [Online]. Available: https://www.ipieca.org/resources/energy-efficiency-solutions/combined-cycle-gas-turbines-2022
[128] J. Otomo, S. Yamate, and J. A. Ortiz-Corrales, “Bilayer Cell Model and System Design of Highly Efficient Protonic Ceramic Fuel Cells,” *ECS Trans.*, vol. 111, no. 6, p. 1075, May 2023, doi: 10.1149/11106.1075ecst.
[129] R. O’Hayre, “ARPA-E Project | Fuel-Flexible Protonic Ceramic Fuel Cell Stack,” arpa-e.energy.gov. Accessed: Sep. 13, 2023. [Online]. Available: http://arpa-e.energy.gov/technologies/projects/fuel-flexible-protonic-ceramic-fuel-cell-stack

[130] K. Ferguson, A. Dubois, K. Albrecht, and R. J. Braun, “High performance protonic ceramic fuel cell systems for distributed power generation,” *Energy Convers. Manag.*, vol. 248, p. 114763, Nov. 2021, doi: 10.1016/j.enconman.2021.114763.

[131] J. Jenkins, “Doing The Math On Bloom Energy,” Forbes. Accessed: Sep. 14, 2023. [Online]. Available: https://www.forbes.com/2010/02/25/fuel-cell-costs-technology-ecotech-bloom-energy.html

[132] R. O’Hayre *et al.*, “Low-Cost Intermediate-Temperature Fuel-Flexible Protonic-Ceramic Fuel Cell and Stack,” Colorado School of Mines, Golden, CO (United States), Final Report: DOE-CSM-0493-1, Sep. 2021. doi: 10.2172/1861417.

[133] “ExxonMobil Corporate Plan,” ExxonMobil. Accessed: Apr. 22, 2024. [Online]. Available: https://corporate.exxonmobil.com/news/news-releases/2023/1206_exxonmobil-corporate-plan

[134] “Financial Incentives for Hydrogen and Fuel Cell Projects,” Energy.gov. Accessed: Oct. 06, 2023. [Online]. Available: https://www.energy.gov/eere/fuelcells/financial-incentives-hydrogen-and-fuel-cell-projects

[135] “Sources: Bloom Box Costs $12.50 Per Watt.” Accessed: Oct. 06, 2023. [Online]. Available: https://www.greentechmedia.com/articles/read/bloom-update

[136] O. US EPA, “Data Explorer.” Accessed: Jul. 19, 2023. [Online]. Available: https://www.epa.gov/egrid/data-explorer

[137] M. Ziomek-Moroz and J. A. Hawk, “DEGRADATION OF SOLID OXIDE FUEL CELL METALLIC INTERCONNECTS IN FUELS CONTAINING SULFUR”.